MSc. Thesis

Reservoir Considerations for Carbon-Dioxide Plume Geothermal in Depleted Gas Reservoirs

C.P.B. de Beus

TU Delft

Reservoir Considerations for Carbon-Dioxide Plume Geothermal in Depleted Gas Reservoirs

THESIS

submitted in partial fulfillment of the
requirements for the degree of

MASTER OF SCIENCE

in

PETROLEUM ENGINEERING & GEOSCIENCES

by

Charles Pieter Baltus de Beus
born in Rotterdam, the Netherlands

Thesis Committee:

Chair	Dr. D. Voskov	TU Delft
Committee Member	Dr. H. Hajibeygi	TU Delft
Committee Member	Prof. Dr. M.O. Saar	ETH Zurich
Committee Member	Dr. P.J. Vardon	TU Delft
Committee Member	PhD. Candidatte X. Lyu	TU Delft

TU Delft

Reservoir Engineering Section
Department of Geoscience & Engineering
Faculty CEG, Delft University of Technology
Delft, the Netherlands
`www.tudelft.nl/en/ceg/`

© 2021 Charles Pieter Baltus de Beus.

Reservoir Considerations for Carbon-Dioxide Plume Geothermal in Depleted Gas Reservoirs

Author: Charles Pieter Baltus de Beus
Student id: 4359046

Abstract

Carbon dioxide (CO_2) capture and sequestration (CCS) can play a significant role in reducing anthropogenic CO_2 emissions while allowing society to slowly phase out traditional energy sources. One of the main challenge in CCS is the current absence of a clear revenue model. One idea is to use the sequestered supercritical CO_2 as a working fluid for geothermal energy extraction from sedimentary reservoirs (Carbon-dioxide Plume Geothermal or CPG). Due to the large variability in density and mobility of CO_2 under different temperatures, reservoir heterogeneities can give a rise to a combination of convective and conductive heat transfer. In this work, qualitative and quantitative descriptions of the effect of reservoir properties on the performance of CPG in depleted gas fields are provided using an example realistic depleted gas field. The primary focus is on the behaviour of the CO_2 plume with regards to different reservoir properties such as porosity, permeability and thermal properties. The effect of large-scale reservoir structure, such as a presence of an aquifer, net-to-gross ratio and layering is also studied. In order to accurately model these effects, a thermal multi-component multiphase model based on a fugacity-activity Equation of State is built and validated for for pressures from 50-400 bar and temperatures from 35°C to 130°C. The developed thermodynamic model is implemented into the Delft Advanced Research Terra Simulator. Numerous studies of 2D and 3D ensembles and sensitivity studies are carried out to examine the effects of isolated parameters on CPG performance. Results reveal that increased net-to-gross (N/G) ratio is associated with increased recovery factor. In addition, layering architecture becomes an important factor for the importance of conductive flux only at low N/G. Variations in the required pressure to sustain a production rate is associated with fluctuations in production temperature and density due to expansive cooling. Varying reservoir properties and state also have a significant effect on brine upconing, which is detrimental to CPG performance. It appears that an increase in injection rate have a positive effect on the performance of CPG, but this should be studied in conjunction with a coupled wellbore and power plant model. Heterogeneous porosity-permeability realizations show a strong decrease in reservoir lifetime compared to their upscaled homogeneous counterparts, which is caused by a combination of preferential flow, reduced conductive flux and lower production BHP associated with the upscaled realizations. It was also found that reducing production rate delays the time of thermal breakthrough due to the combined effect of these factors.

Preface

This thesis marks the end of seven years of study in Delft. I feel incredibly fortunate to have been able to combine passion in Earth Science with a technological education at such a great university. The graduation process has been quite a journey, being made substantially more challenging by having to do my research during a series of lockdowns with little human contact. Nevertheless, being able to work on a topic as interesting as the one I have chosen was very inspiring. I hope that, in whatever small way, my thesis might contribute to the development of the new and innovative subsurface technologies required not only for the transition of our societal energy system, but also the craft of Petroleum Engineering itself. I am excited for what the future holds!

First and foremost I'd like to thank my main supervisor Dr. Denis Voskov, with whom I could always discuss problems and challenges, even at the most unorthodox of times. I was incredibly impressed by your knowledge of reservoir simulation, as well as the commitment you put into giving me guidance on any problems I encountered. I could not have wished for a more involved supervisor.

I would also like to thank Xiaocong Lyu, who helped me innumerable times with challenges surrounding every facet of my thesis from programming to writing, and was always available for a quick chat if the need arose.

I would also like to express my gratitude to Dr. Hadi Hajibeygi and Dr. Martin Saar for being the co-supervisors on my thesis. Ever since I met Hadi three years ago, I've known him as an inspiring educator who provoked you to think deeper, and ask better questions. Your weekly input was very valuable and much appreciated. Martins research on CPG was the very reason I chose to pursue the topic of this research over other options. It was a great honour to be able to get feedback and input from one of the first people to describe the concept, and you were able to steer me towards better results.

Furthermore, I would like to thank all my friends who presented me with ideas and advice at the best of times. A special thanks to my parents and their unwavering support in the final stages of the project.

-"Água mole em pedra dura tanto bate até que fura"
C.P.B. de Beus
Oostelbeers, August 2021

Contents

Preface **iii**
Preface iii

Contents **v**

List of Figures **viii**

List of Tables **xii**

1 Introduction **1**
1.1 Carbon Capture and Storage 2
1.1.1 Potential for CCS in the Netherlands 3
1.1.2 Challenges for CCS 4
1.2 Carbon Plume Geothermal 4
1.2.1 Differences between Carbon Plume Geothermal and Hydrothermal systems 5
1.2.2 Current Research 6
1.3 Research Objectives 6

2 Literature Study **9**
2.1 Carbon Plume Geothermal 9
2.1.1 Carbon dioxide as a geothermal working fluid 9
2.1.2 The Carbon Plume Geothermal Cycle 11
2.2 Heterogeneity 14
2.2.1 Types of heterogeneity 15
2.2.2 Scales of heterogeneity 15
2.2.3 Quantifying Heterogeneity 18
2.3 Reservoir Model 18
2.3.1 Geological setting 18
2.3.2 Modelling values 20

3 Simulation Model **23**
3.1 Model Description 23
3.1.1 Modelling objectives and assumptions 24
3.2 Governing Equations 25
3.2.1 Mass Balance Equation 25
3.2.2 Energy Conservation Equation 26
3.2.3 Operator Based Linearization 26
3.3 Thermodynamic Model 28

3.3.1 Non-aqueous component phase partitioning 29
3.3.2 Aqueous component phase partitioning 31
3.3.3 Flash 32
3.4 Physical Properties 32
3.4.1 Flow properties 32
3.4.2 Non-aqueous phase properties 33
3.4.3 Aqueous phase properties 36

4 Simulation Strategies 41
4.1 Simulation Strategies for Model 41
4.2 Experiment Setup for Macroscale Heterogeneity 43
4.2.1 Synthetic reservoir ensemble for layering study 44
4.2.2 Experiment analysis 45
4.3 Experimental Setup for Sensitivity Study 46
4.3.1 Synthetic reservoir for 2D sensitivity 46
4.4 Experimental Setup for 3D Simulation 48
4.4.1 3D Box models 49

5 Simulation Results 53
5.1 Results from the Macroscale Experiments 53
5.1.1 Energy extraction 54
5.1.2 Recovery factor 56
5.1.3 Importance of conductive flux 56
5.2 Results of Sensitivity Study 58
5.2.1 Base case 58
5.2.2 Initial state parameters 61
5.2.3 Reservoir parameters 65
5.2.4 Parameters of relative permeability 67
5.2.5 Thermal parameters 70
5.2.6 Control parameter 71
5.3 Results of 3D Simulation Study 73
5.3.1 Results from the 3D-box case 73
5.3.2 Results from the 3D-box model with lower flow rate 74
5.3.3 Results from the increased permeability in 3D-box case 76

6 Conclusions 79
6.1 Discussion 79
6.2 Conclusion 81
6.3 Recommendations 82

Bibliography 85

Acronyms 91

A Supplemental Model information 93
A.1 Supplemental information to the Thermodynamic Model 93
A.2 Supplemental Information to Physical Properties 94

B Model Validation 97
B.1 Validation of component phase partitioning 97
B.2 Validation of the non-aqueous phase properties 98
B.3 Validation of the aqueous phase properties 100

C Supplemental Results 107
C.1 Appendix to 2D Sensitivity Study 107
  C.1.1 Supplemental figures to the Inital State Parameters 107
  C.1.2 Supplemental Reservoir parameter figures 109
  C.1.3 Supplemental Relperm parameter figures 111
  C.1.4 Supplemental Thermal Parameter figures 112
C.2 Supplemental figures to the 3D Study 114

List of Figures

1.1 Figure showing different CCS target geologies, after [51] 2
1.3 The location of the recently approved Porthos CCS project near the Rotterdam Port area [65] 3
1.4 Schematic simplified overview of a CPG system set-up from [33] 4
1.5 Two graphs showing the depth of Dutch gas reservoirs (left) [72] and temperature gradient in the Netherlands (right) [14] 5

2.1 Two graphs showing the phase diagrams for water (left) [49] and carbon dioxide with common states for CO_2 (right) 9
2.2 Three graphs showing density, kinematic viscosity and specific enthalpy for combinations of CO_2 and CH_4, from [24] using NIST reference data [46] 10
2.3 Example of CO_2 based geothermal thermodynamic cycle 11
2.4 Example of CPG being added to the lifecycle of a gas reservoir, modified after [28] 13
2.5 Different types of depositional environments within a sedimentary system [55] . 14
2.6 Image showing the different relevant scales for heterogeneity 15
2.8 Example from the Libyan K-field showing how areal heterogeneity translates to complex reservoir facies distribution [67] 17
2.9 Figures showing geographical location of the PRN in Rotterdam, with neighbouring fields Pernis-West (PRW) and the Rotterdam Field (RTD) (left) and seismic interpretation of PRN (right) 19
2.11 Porosity-permeability graph of PRN storage layers from [16] 21

3.1 Figures showing the phase envelope and critical points for binary CO_2-CH_4 mixtures (left) and a phase diagram for pure CO_2 (right) from [24] 24
3.3 Relative permeability curves using Brooks-Corey for the Pernis field 33

4.1 Model cell thickness growing exponentially in over- and underburden 43
4.3 Schematic example of layering generation framework 45
4.4 N/G distribution of the sampled reservoir realizations 45
4.5 Array of some possible reservoir realizations 46
4.7 Well locations shown together with the different layers (left) and in a pressure profile plot during a run (right) 47
4.10 3D Box model from the Pernis Petrel model [16] 49
4.11 Crosssections of 3D Box realizations centered on the EEM-01 Well. Left to right, top to bottom: Realization 40 x and y direction, Realization 80 x and y direction . 50
4.12 Schematic description of 5-spot pattern, modified after [15] 50

5.1 Array of the temperature distribution at thermal breakthrough for the realizations from Figure 4.5 53

5.2 Histograms of energy produced per volume of net rock 54
5.3 Scatter plots of energy produced per volume of net rock 55
5.4 Histogram of contact surfaces over entire dataset 55
5.5 Base case plots of reservoir thermal properties 55
5.6 Histograms of Recovery Factors 56
5.7 Scatter plots of Recovery Factor 56
5.8 Base case plots of reservoir thermal properties 57
5.9 Base case plots of phase densities and viscosities after 15 years of CPG 58
5.10 Base case thermal profile after 15 and 60 years of CPG 59
5.11 Base case saturation profile after 15 and 60 years of CPG 59
5.12 Base case production data 60
5.13 Base case production data per production well 60
5.14 Comparison between the two reservoir segments, 1 is upper and 2 is lower 61
5.15 Production graphs for reservoir pressure sensitivity test per well 61
5.16 Reservoir pressure sensitivity saturation profile after 60 years of CPG. From left to right: low case, base case, high case 62
5.17 Production graphs for reservoir temperature sensitivity test 62
5.18 Reservoir temperature sensitivity saturation profile after 60 years of CPG. From left to right: low case, base case, high case 63
5.19 Production graphs for reservoir temperature sensitivity test per well 63
5.20 Brine salinity sensitivity saturation profile after 60 years of CPG. From left to right: low case, base case, high case 63
5.21 Production graphs for salinity sensitivity test per well 64
5.22 Bottomhole pressure profile for the Salinity sensitivty test 64
5.23 Separating layer thickness and temperature profile after 60 years of CPG. from left to right: low case, base case and high case 65
5.24 Production graphs for separating layer thickness test 65
5.25 Permeability anisotropy sensitivity saturation profile after 60 years of CPG. From left to right: low case, base case, high case 66
5.26 Production graphs per well for permeability anisotropy sensitivity test 66
5.27 Brooks-Corey gas exponent sensitivity saturation profile after 60 years of CPG. From left to right: low case, base case, high case 67
5.28 Brooks-Corey gas exponent sensitivity pressure profile after 15 years of CPG. From left to right: low case, base case, high case 67
5.29 Production graphs per well for Brooks-Corey gas exponent sensitivity test 68
5.30 Production well BHP profile for Brooks-Corey gas exponent test 68
5.31 Brooks-Corey water exponent sensitivity saturation profile after 60 years of CPG. From left to right: low case, base case, high case 69
5.32 Production graphs per well for Brooks-Corey water exponent sensitivity test . . . 69
5.33 Production graphs per well for Brooks-Corey water exponent sensitivity test . . . 69
5.34 Production graphs for the heat capacity sensitivity test 70
5.35 Thermal conductivity sensitivity temperature profile after 60 years of CPG. From left to right: low case, base case, high case 70
5.36 Production graphs for the thermal conductivity sensitivity test 71
5.37 Pressure distribution after 15 years of CPG for the injection surplus comparative test, as well as the pressure profile in the production wells 72
5.38 Production graphs for the injection surplus comparative test 72
5.39 Production graphs per well for the injection surplus comparative test 72
5.40 Reservoir information for the 3D Box model cases 73
5.41 Graphs showing sideview temperature distribution for the best performing realization (top) and worst performing realization (bottom) after 30 years of CPG . . 73
5.42 Temperature profile for the 3D-box model case 74

5.43 Thermal energy extraction and mass flowrate for the 3D box base case realizations 74
5.44 Scatter plot of cumulative energy extraction for every facies realization with facies mean in grey 75
5.45 Temperature profile for the 3D Box Model Base case 75
5.46 Production temperature for 3D box base case and low production case 76
5.47 Scatter plot of thermal performance for the 3D box base case and low rate case heterogeneous realizations 76
5.48 Temperature profile comparison for the heterogeneous base case and increased permeability realizations 77
5.49 Temperature profile comparison for the heterogeneous and homogeneous increased permeability realizations 77

B.1 Graphs showing the saturation molality of CO_2 in water for a range of different temperatures, pressures and salinities compared to experimental data from [26] 97
B.2 Graphs showing the saturation molality of CO_2 in water and H_2O in the non-aqueous phase from the used model (left) and a comparative graph from [82] using data from [26] 98
B.3 Non-aqueous phase density for a range of pressures and temperatures at 3 compositions is shown, compared to NIST reference data[46] for the pure components 99
B.4 Non-aqueous phase viscosity for a range of pressures and temperatures for pure components is shown, compared to NIST reference data [46] 99
B.5 Pure CO_2 and CH_4 phase relative enthalpies for the non-aqueous phase using [32] and data from [46] 100
B.6 Non-aqueous phase thermal conductivity for a range of pressures and temperatures for pure CO_2 is shown, compared to NIST reference data [46] 101
B.7 Aqueous phase density for a range of pressures and temperatures for pure H_2O is shown, compared to NIST reference data [46] 101
B.8 Aqueous phase density with saturation concentration CO_2 for a range of pressures, temperatures and salinities are shown for pure H_2O is shown with experimental data from [50] 102
B.9 Aqueous phase viscosity for a range of pressures and temperatures for pure H_2O is shown, compared to NIST reference data [46] 102
B.11 Pure water enthalpy using correlations from Keenan et al.[32] 104
B.12 Effect of salinity on AqP enthalpy, with the validating graph from Guo [32] . . . 104
B.13 Graphs comparing the enthalpy of dissolution of CO_2, with the model (left) compared to the validation graph from Guo (right) 104
B.14 Aqueous phase thermal conductivity for a range of pressures and temperatures for pure H_2O is shown, compared to NIST reference data [46] 105

C.1 Production graphs for Reservoir Pressure Sensitivity test 107
C.2 Production well pressure profiles for the Reservoir Pressure Sensitivity test . . . 107
C.3 Production graphs for Reservoir Temperature Sensitivity test per well 108
C.4 Production graphs for the Salinity Sensitivity tests 108
C.5 Production graphs for separating layer thickness test per well 109
C.6 Pressure profile for the separating layer sensitivity test 109
C.7 Production graphs for permeability anisotropy sensitivity test 110
C.8 Production graphs per well for permeability anisotropy sensitivity test 110
C.9 Production graphs per well for the Brooks-Corey gas exponent sensitivity tests . 111
C.10 Production graphs per well for Brooks-Corey water exponent sensitivity test per well 111
C.11 Brooks-Corey water exponent sensitivity pressure profile after 15 years of CPG. From left to right: low case, base case, high case 112

C.12 Production graphs per well for the Heat Capacity sensitivity test 112
C.13 BHP profile for the Heat Capacity sensitivity test 112
C.14 Production graphs per well for the thermal conductivity sensitivity test 113
C.15 BHP profile for the thermal conductivity sensitivity test 113
C.16 Thermal energy extraction and mass flow rate for the 3D box base case realizations 114
C.17 Graphs showing the top down temperature distribution for the best performing realization(left) and worst performing realization(right) after 30 years of CPG . 114

List of Tables

1.2 Dutch CCS potential capacity from [27] 3

2.7 Heterogeneity considerations across different scales 16
2.10 Pernis reservoir lithology according to [16] 19
2.12 Saturation values for the Pernis field from [16] 21

3.2 Correlations used in the model with their validity ranges 32
3.4 Tuned coefficients from [10] used in Equation 3.53 35

4.2 Reservoir specifics for the 2D Macroscale ensemble generation 44
4.6 Lithology to 2D reservoir model conversion 47
4.8 Properties for the base case reservoir model 48
4.9 Overview of different parameters tested in the 2D sensitivity study, * signifies base case variable 49

A.1 Table showing the constants used for determination of k_h used in Equation 3.32 . 93
A.2 Second order interaction coefficients used in Equation 3.33 93
A.3 Third order interaction coefficients used in Equation 3.33 94
A.4 Binary interaction coefficients between H_2O and Gaseous components used in Equation 3.30 94
A.5 Fitting coefficients for CO_2 viscosity computation in Equation 3.47 94
A.6 Fitting coefficients for CH_4 viscosity computation in Equation 3.48 94
A.7 Constants for the determination of ideal gas component enthalpy from [32] and [9] in Equation 3.50 95
A.8 Coefficients for density of brine as function of temperature at 70 MPa for Equation 3.55 95
A.9 Coefficients for different variants of Equation 3.57 and Equation 3.56 95
A.10 coefficients used for the computation of $E_{Cm,i}$ and $F_{C_{m,i}}$ in Equation 3.59 95
A.11 Constants used to compute salt dissolution enthalpy in Equation 3.67 96

B.10 Effect of salinity and dissolved CO_2 on aqueous phase viscosity with experimental data from [50] 103

Chapter 1

Introduction

One of the greatest scientific, technological, economic, and thus ultimately societal challenges of this century is how to provide energy to a growing global population, while mitigating global climate change, caused by elevated carbon dioxide (CO_2) concentration in the atmosphere as a result of human activity, such as farming and the combustion of fossil fuels [22]. CO_2 is among the so-called 'greenhouse gasses' which prevent thermal radiation from diffusing into space. Subsequently, prolonged presence of greenhouse gasses increases the energy balance in the atmosphere and causes elevated average temperatures and exacerbates extreme weather events [81]. As part of the 2015 Paris Agreement 195 countries have pledged to reduce Carbon Dioxide emissions with the aim of limiting global temperature rise to 2°C, ushering in an age of transformation in the way modern societies foresee in their energy demands [71].

Solely phasing in renewable energy sources is insufficient for reaching these goals, as this transformation is too slow for the excessive global emission rates the world is currently seeing. One feasible solution is the storage of CO_2 in geological formations in the subsurface by means of injection into aquifers or depleted hydrocarbon reservoirs. Depleted gas reservoirs have been shown to have suitable characteristics for storage, such as a proven seal and existing infrastructure [51].

Carbon Capture and Storage (CCS) can play a significant role in reducing anthropogenic CO2 emissions while allowing society to keep making use of less clean, traditional energy sources in the time it takes to transition. Studies have shown the importance of CCS for the mitigation of global temperature rise, based among other things on it's role in limiting fossil-fuel emissions in electricity generation and industrial applications. Most of the climate change mitigation pathways projected by the ICC that limit temperature rise to 1.5°C in 2100 thus partially rely on the use of carbon dioxide removal such asCCS technologies [38].

1.1 Carbon Capture and Storage

Due to the large amount of accessible volume, the subsurface is among the prime options for permanently storing the CO_2 volume required to cause a significant effect on global emissions. Geological formations which are considered good targets are characterized by large volume, favourable formation properties and safe trapping stratigraphy, which is necessary to minimize the chance of leakage to the surface on the timescale required for storage to be considered permanent [31]. Alternatively, technological solutions such as foam-assisted CO_2 storage can be employed to reduce the mobility of the injected plume [48]. Three main target geologies as shown in Figure 1.1 considered for CCS are:

- Hydrocarbon bearing reservoirs, either depleted or as part of enhanced hydrocarbon recovery
- Saline aquifers
- Coal beds

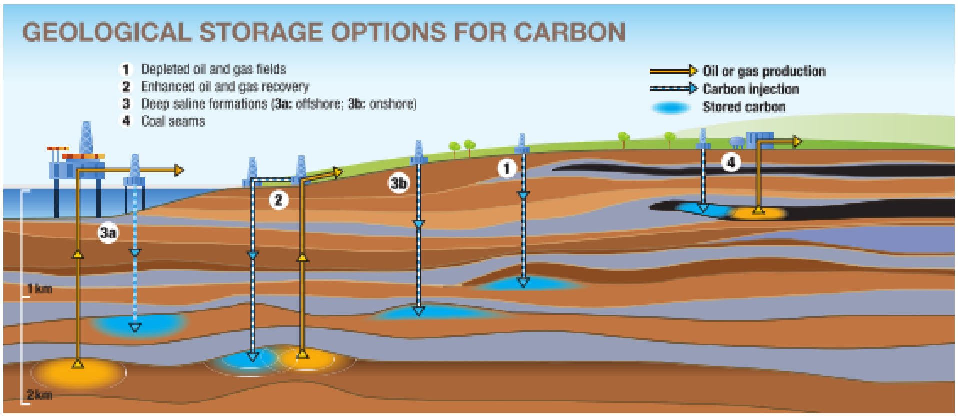
GEOLOGICAL STORAGE OPTIONS FOR CARBON
1 Depleted oil and gas fields
2 Enhanced oil and gas recovery
3 Deep saline formations (3a: offshore; 3b: onshore)
4 Coal seams
Oil or gas production
Carbon injection
Stored carbon
3a
2
3b
1
4
1 km
2km

Figure 1.1: Figure showing different CCS target geologies, after [51]

Of these, the primary options for the sake of CO_2 emission mitigation are saline aquifers and depleted hydrocarbon reservoirs(note that Enhanced Hydrocarbon Recovery with CO_2 injection results in a limited net emission reduction). Saline aquifers generally offer higher storage capacities, are more abundantly present in the subsurface [51]. However, Saline aquifers are commonly undeveloped, and as such little information is available on the sealing capacity and flow properties. Due to being undeveloped, the pressure is normally close to hydrostatic.

On the contrary, considered hydrocarbon reservoirs, either depleted or active in production, will have some form of sealing structure necessary for hydrocarbon trapping, as well as existing infrastructure and some degree of reservoir characterization. Especially in the case for gas reservoirs, this seal can be considered quite safe for use for CCS (CH_4 is a smaller molecule than CO_2). In these types of reservoirs, modelling of dynamic behaviour can be complicated by the numerous phases which can be present at the same time dependant on the type of present hydrocarbon. Arising fluid phase properties such as compressibility and miscibility can give rise to complex dynamic behaviour and impact storage capacity. additionally, pressure can range from anywhere above hydrostatic pressure (i.e. overpressured gas reservoirs) to below 50 bar for depleted gas reservoirs without strong driving mechanism. For depleted gas reservoirs, very low pressure can give rise to Joule-Thompson cooling effects around the injection wellbore [24].

1.1.1 Potential for CCS in the Netherlands

The Netherlands contains over 190 exploited gas fields, both offshore and onshore with the Groningen gas field being the largest gas field in Europe. The majority of these fields is developed and nearly or already at the end of their productive life cycle, and could be repurposed to CO_2 storage facilities [57]. More than 150 of these have been characterized as potential subsurface storage locations, totalling a capacity of around 2.7 Gt as shown in Table 1.2 [27], which as-is would be sufficient to fully store the 2020 total national emission of 166 Mt for over 16 years[21].

Location	Offshore		Onshore*	
	Capacity (Gt)	No. of fields	Capacity (Gt)	No. of fields
Theoretical storage capacity	2.2	222	1.4	172
Practical storage capacity	1.7	104	1.1	54

*Might be considered difficult to develop due to societal resistance

Table 1.2: Dutch CCS potential capacity from [27]

Note that In the Netherlands, political friction following seismic events originating from the Groningen gas field have created societal resistance to onshore activity, culminating in a 2019 decision by the Dutch government to start decommisioning the Groningen field. This has lead to the focus for CCS activity shifting offshore. Especially large offshore fields with high capacities (>100Mt) and favourable reservoir properties as located in the K and L blocks, and fields close to shore (P and Q blocks) are studied for development [27]. These reservoirs are predominantly depleted gas reservoirs without aquifer drive, meaning abandonment pressures are exceptionally low (below 50 bar).

Figure 1.3: The location of the recently approved Porthos CCS project near the Rotterdam Port area [65]

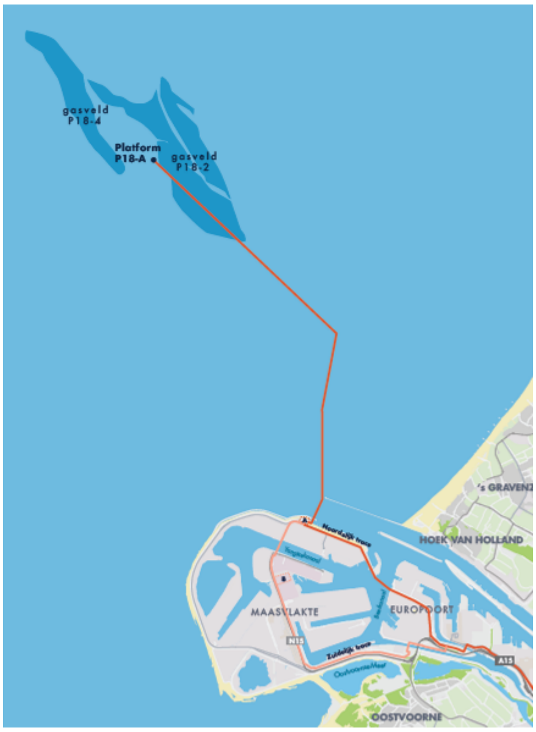

As part of a 2017 Coalition agreement, the Dutch government pledged to capture and store 20 Mt CO_2 as part of their ambition to realize a 49% reduction in emissions in 2030, signifying intent to develop CCS projects. As part of this, in 2020 subsidies were granted for the development of the Porthos CCS project, which aims to store 2-2.5 Mt per year, cutting into the emissions of the Rotterdam Port area industrial zone which makes up over 16% of the total national emissions. The target reservoirs are the P18-4 and P18-2 fields in the aforementioned P-block, chosen due to its strategic location as shown in Figure 1.3.

1.1.2 Challenges for CCS

Despite recent advancements in the field of CCS, some challenges still remain . As mentioned in the previous section, resistance from society can act as a barrier to development onshore, and the awarding of subsidies to the Porthos project was also seen as controversial by some, due to the involvement of large oil companies with the project. One such project which did not succeed was the Barendrecht CCS project, which aimed to store 10 Mt originating from the Shell Pernis refinery under the Dutch city of Barendrecht. Intense resistance from local government and inhabitants ended in the cancellation of further development [19].

An earlier attempt for the P18-4 field called the ROAD project, aiming to store 5 Mt over a span of 5 years, also did not succeed. Here lack of sufficient funding was cited as one of the main reasons for failure [62]. One of the main challenges to be overcome for speedy implementation is the current absence of a revenue model for the sequestration of CO_2, barring any local government subsidies. One novel idea proposed by Randolph and Saar [60] is to use the sequestered supercritical CO_2 as a working fluid for geothermal energy extraction from sedimentary reservoirs which is called Carbon-Dioxide Plume Geothermal (CPG) technology.

1.2 Carbon Plume Geothermal

In order to reach the climate goals set by governments across the globe, it is necessary to reduce and even reverse global carbon emissions, and move to a more sustainable model for energy generation. Within this shift, geothermal energy generation is seen as a promising technology due to it's consistency and wide availability. While conventional geothermal energy systems work by circulating hot brine, the novel approach of Carbon-Dioxide Plume Geothermal (CPG) proposed by Jimmy Randolph and Martin Saar proposes the use of supercritical anthropogenic CO2 as a working fluid [60]. The principle idea of a CPG system may be summarized as follows: CO_2 from local CO_2 emitters is captured employing Carbon-Capture (CC) technologies, after which the CO_2 can be transported to a CPG site and injected into a geologic CO_2 storage formation, resulting in CCS. Then, using a secondary production well, the CO_2 which has been heated by the formation gets produced and put through a combination of turbines and/or heat exchanges, extracting most of the available energy. The CO_2 is then cooled and reinjected. This process is shown schematically in Figure 1.4.

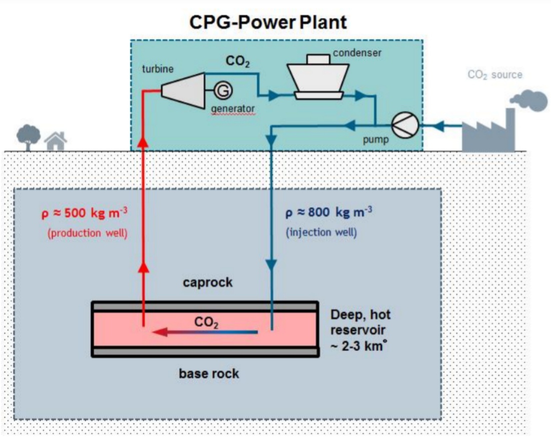

Figure 1.4: Schematic simplified overview of a CPG system set-up from [33]

For CPG, deviating from conventional CCS projects, the CO_2 storage formation needs to exhibit a temperature that is sufficiently high to conduct CPG operations economically, i.e., at least about 100°C. Target reservoirs need to have sufficient permeability of ⩾10 mD (1 mD = 10-15m^2) and need to be overlain by a caprock of sufficiently low permeability of about ⩽0.01 mD to enable efficient and safe CO_2 injection into the reservoir. This is further illustrated in a study by Adams et al., who concluded that CPG systems have up to twice electricity generation potential for shallow (2-3km depth) and low permeability (10-100 mD) reservoirs [1] [33]. The primarily depletion driven depleted gas reservoirs which are considered in the Netherlands for the most part adhere to these requirements, with depths predominantly below 3000m resulting in temperatures with considerable geothermal potential [11] ranging between $100 - 150°C$, as shown in Figure 1.2.

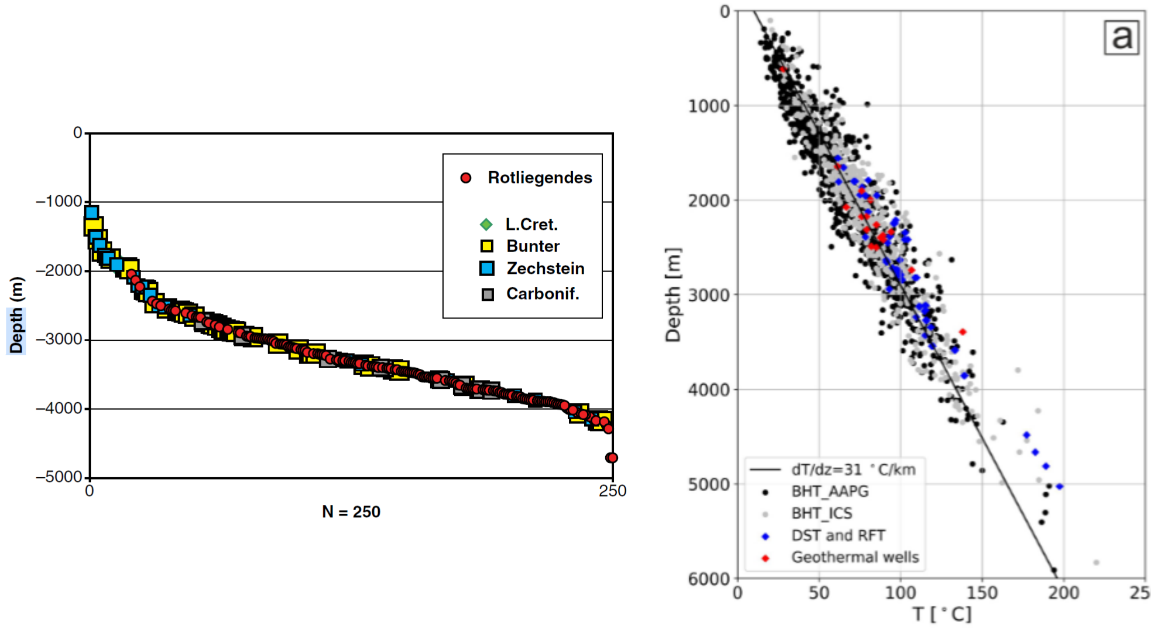

Figure 1.5: Two graphs showing the depth of Dutch gas reservoirs (left) [72] and temperature gradient in the Netherlands (right) [14]

1.2.1 Differences between Carbon Plume Geothermal and Hydrothermal systems

The most evident difference between a Geothermal system based on CO_2 versus H_2O is the distinct common production phases. While water under reservoir conditions can be assumed to be mostly liquid phase, whereas CO_2 under reservoir conditions will be either gaseous or supercritical. This translates to a substantially lower dynamic viscosity for CO_2 which is multiple times less than that of brine [2]. It should be noted that the properties of supercritical CO_2 $(scCO_2)$ are very sensitive to changes in pressure and temperature, and as such a precise figure is dependent on local reservoir conditions. This viscosity difference translates to a lower pressure loss in sedimentary reservoirs compared to brine at comparable mass flowrates. In turn, this allows for higher heat extraction rates [60]. The extracted heat can also be used differently. Direct-Cycle Hydrothermal systems require a temperature of at least 100° at turbine inlet to allow for steam generation, whereas CO_2 can drive a turbine to generate electricity at different ranges of temperatures and pressures. This will be further elaborated on in chapter 2.

Within the reservoir, the aforementioned reduced pressure loss is not only caused by the difference in dynamic viscosity. In fact, the high thermal expansivity of supercritical CO_2 gives rise to a thermosiphon effect, where expansion across the thermal front maintains pressure across the well-to-well section, further reducing pressure drop and reducing or even eliminating parasitic pumping power load [5]. Within the wellbore, transport approaches adiabatic conditions after a short time of continuous production [61]. However, adiabatic expansion in the wellbore causes cooling, converting temperature into pressure. This means that compared to a comparable hydrothermal system, wellhead temperatures will be considerably lower. This is offset by a higher pressure, the energy of which can be exploited with a turbine.

1.2.2 Current Research

The idea of combining CO_2 sequestration and geothermal energy capture is quite a recent idea. Initial research into feasibility was performed by Randolph and Saar [60] using the TOUGH2 simulator, which found favourable heat extraction rates under a variety of reservoir depths. Follow-up research into the physics of CPG explored the pressure maintaining effect of the thermosiphon [5], the adiabatic behaviour and adiabatic cooling in the production wellbore [61]. An important study into the electrical power potential of CPG versus hydrothermal systems found again favourable performance for CPG, as well as the potential to use a direct cycle at lower temperatures where conventional hydrothermal would require indirect binary systems to generate electricity [2]. The economics of CPG were further studied by Hansper et al., finding that an example brownfield CPG system could be competetive with other sources of energy. It should be noted that revenues or costs of CO_2 sequestration were not included in this study [33]. Ezekiel studied the application of CPG to depleted gas reservoirs, finding synergy in combining EGR with CPG to extend the lifetime of gas reservoirs. This study was partially the basis of this research due to the predominance of depleted gas reservoirs considered for sequestration in the Netherlands [28]. It should be noted that in the Netherlands, expected additional gas recovery due to EGR is limited [45]. However, other advantages of using these formations, such as a proven seal and existing infrastructure and reservoir characterization, still exist. All of the aforementioned studies were performed using homogeneous reservoir models. Garapati researched the effect of layering on CPG performance in Brine reservoirs, finding that layer heterogeneity significantly impacted the shape and path of a buoyant CO_2 plume in an aquifer [29]. Xu performed additional research, testing CPG on a simple geostatistical permeability distribution [80]. A recent paper by Adams et al. researched optimal well placement and well pipe diameter, as well as finding that reservoir thickness is positively correlated with average power generation. It should be noted that the majority of these studies have been performed using TOUGH2 on simple reservoir models, with either a completely homogeneous or simple heterogeneous property distribution. This is in part due to simulator limitations. In order to further improve the width of studies to be performed on CPG, value could be added by developing CPG research capabilities on additional reservoir simulators with extended capabilities for modeling thermal multiphase multi-component behaviour efficiently.

1.3 Research Objectives

CPG shows considerable promise as a revenue stream for CO_2 sequestration, and earlier research merits looking into the possibilities of transferring CPG from academia to the real world. Within the Netherlands, CPG within depleted gas reservoirs is interesting due to the abundant potential targets. However, modelling thermal CO_2 injection with hydrocarbon and aquifer presence is complex and highly nonlinear. Current simulators capable of handling this type of problem have other limitations, and as such new avenues of research could be opened up by extending simulation capabilities to new engines. The Delft Advanced Research Terra Simulator (DARTS) [73] offers a very powerful and flexible way to study thermal systems, as shown by extensive uncertainty quantification done by Wang et al. [78] on geothermal systems in complex geologies.

As such, this research sets out to develop simulation capability for CPG in depleted gas reservoirs, as well as test the system on a variety of different parameters influenced by geology. The research question can be formulated as follows:

Using a simulator capable of true heterogeneity, how do different types of real-world heterogeneities/uncertainties affect the viability and performance of a depleted gas CPG system?

1. How do common uncertain parameters influence CPG system behaviour?
2. How does large scale heterogeneity influence CPG performance?
3. How does realistic heterogeneity affect CPG performance?

In order to answer these questions, the following objectives can be defined:

1. Build and validate a model using DARTS capabilities of modelling multiphase multicomponent thermal flow behaviour
2. Perform a sensitivity analysis on varying reservoir parameters
3. Perform studies of different types of heterogeneities on realistic reservoir realizations

It should be noted that this study focuses on reservoir behaviour. As such, posted power outputs are thermal power production, which is indicative but not equal to the resulting exergy, electricity or heating output of the system.

Overview of chapters

This thesis is split up into six chapters. The Introduction, which you are reading now, aims to elaborate on the setting within which this research question was chosen, as well as give background to the different choices made in further chapters. Next, the Literature Study aims to further discuss CPG considerations create a framework for experiments based on a definition of geological heterogeneity, and give a characterization of the reservoir used as a reference to create the static models in this study. The Model chapter concerns itself with the dynamic model which solves the thermal compositional problem of CPG in depleted gas reservoirs, as well as the implementation in DARTS. Subsequently, the Simulation Strategy chapter gives background information on the different experiment setups and procedures used to generate insights. The Results chapter showcases and discusses the model validation and results from different experiments. Finally, the Conclusions chapter will show and discuss research conclusions and recommendations for future work.

Chapter 2

Literature Study

In this chapter, further background information will be given regarding the research topic. Firstly, the CPG cycle and its application to depleted gas reservoirs will be discussed in more detail. Following this, a detailed definition of heterogeneity in reservoirs is given, which forms the basis for the different experiments done. Finally, some background information is given on the reservoir used for realistic reference values.

2.1 Carbon Plume Geothermal

2.1.1 Carbon dioxide as a geothermal working fluid

Using carbon dioxide as a working fluid for geothermal energy systems necessitates different considerations with regards to the type of target reservoir, infrastructure and production design. Next to that, differences in properties and phase behaviour can significantly impact every part of the life cycle. As shown below in subsection 2.1.1, water will most commonly be in liquid phase under reservoir conditions, with surface flashing to gas phase (steam) being possible with considerable temperature. This means that hydrothermal systems can be in most cases assumed to be a single phase, incompressible flow system, greatly reducing simulation complexity. Conversely, CO_2 under reservoir conditions can be either in a gas phase, dense liquid phase or supercritical state depending on pressure and temperature conditions. This means that not only can multiple CO_2 phases can exist in a single simulation, but also that the fluid has varying physical and chemical properties under different P,T-conditions. This means that not only will CO_2 behave differently between two reservoirs with different pressure and temperature, but also within a reservoir with a pressure gradient and thermal front.

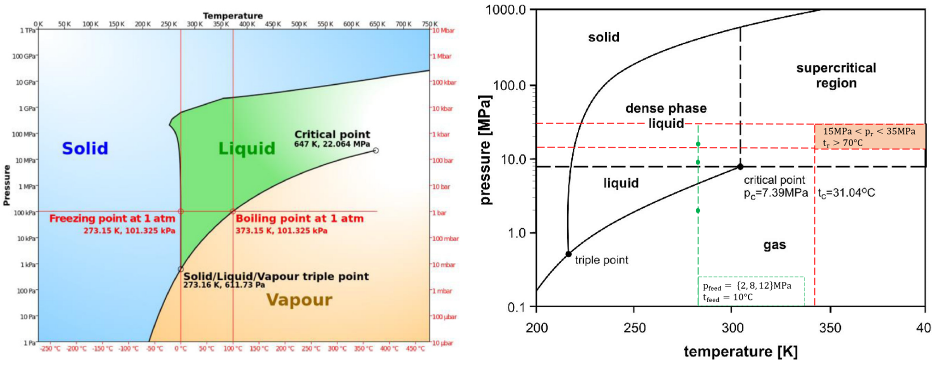

Figure 2.1: Two graphs showing the phase diagrams for water (left) [49] and carbon dioxide with common states for CO_2 (right)

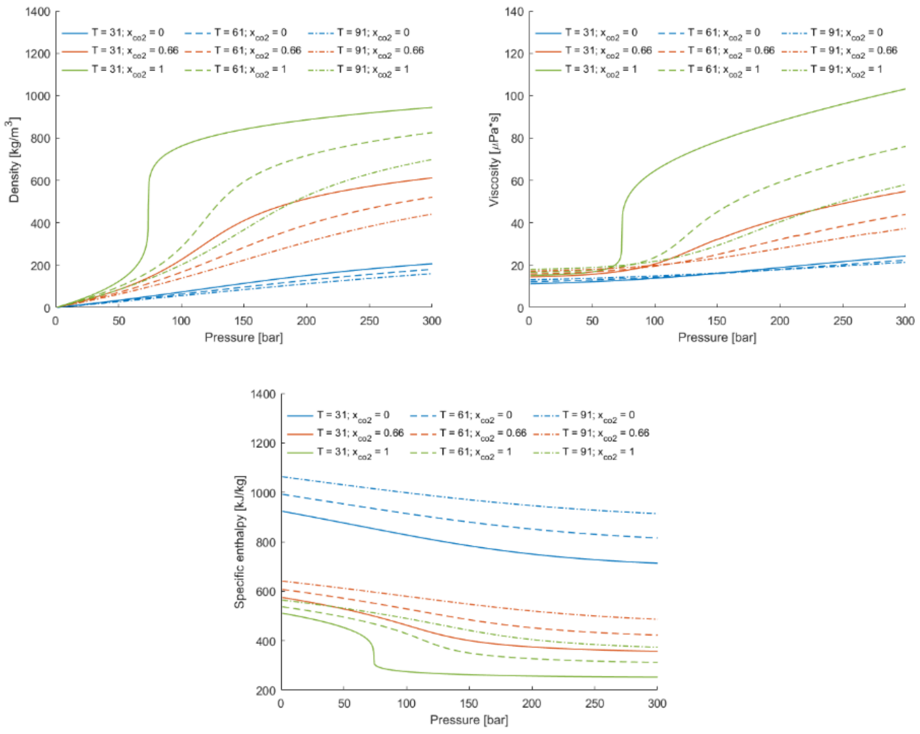

Figure 2.2: Three graphs showing density, kinematic viscosity and specific enthalpy for combinations of CO_2 and CH_4, from [24] using NIST reference data [46]

What this means for reservoir simulation is that a CPG in a reservoir with trace water requires multiple components, multiple possibly compressible phases and strongly nonlinear transport behaviour under varying P, T and composition. To illustrate, Figure 2.2 shows the large variability of CO_2 compared to CH_4 in important properties for mass and energy transport. Clearly observable is the stark difference between sub- and supercritical properties as the critical point of CO_2 is surpassed. Additionally one can observe the larger variability in e.g. dynamic viscosity with changing temperature and pressure compared to CH_4. In order to model thermal behaviour, accurate simulation of many important properties over a range of pressures and temperatures is required.

Corrosion

One important consideration in both CCS and CPG is the corrosivitiy of a near-pure phase. In the presence of water carbonic acid can form which is very potent in corroding iron. Common contaminants such as sulphur and nitrogen can also have an effect on the corrosivity of the phase. Cole [23] characterized four different regimes:

(A) Very low contaminant levels and extremely low water content. Very low corrosion rates occur.

(B) Low contaminant levels and water content below the solubility content. Significant corrosion can occur is H_2O concentration exceeds a critical limit, the exact value of which is poorly studied.

(C) Low contaminant levels and water content above the solubility content. Corrosion rates increase dramatically if an aqueous phase is present.

(D) Moderate contaminant levels and water content above the solubility limit. Poorly studied, but similar behaviour to C expected.

In most surface pipelines, contaminant levels and water content can be closely controlled, allowing for regime A to be present. However, produced CO_2 from a reservoir at connate water saturation will practically always be at solubility limit for water, meaning there exists a real risk for corrosion of the production well and power plant infrastructure. If an aqueous phase is co-produced, this corrosivity can be expected to be more severe still. This means that special equipment will be required to prevent corrosion in the production wells and power plant infrastructure, and that not co-producing an aqueous phase should be preferred in production planning [23].

2.1.2 The Carbon Plume Geothermal Cycle

In order to evaluate the feasibility of a geothermal project, it's necessary to quantify the amount of useful energy the system can produce. It's important to note that the amount of heat energy extracted from the ground is not equal to the amount of power a geothermal power plant can produce. Parasitic power loads such as for pumping or running other surface equipment eat into the net produced power. On a more fundamental level, irreversabilities and inefficiencies in the thermodynamic process mean that the amount of usable work(called exergy) is less than the amount of energy in the system. Therefore, it is important to know the different stages of the thermodynamic cycle of CPG.

Design of cycle

The production process for a simple, direct cycle geothermal system with CO_2 as a working fluid is shown in Figure 2.3 can be described as:

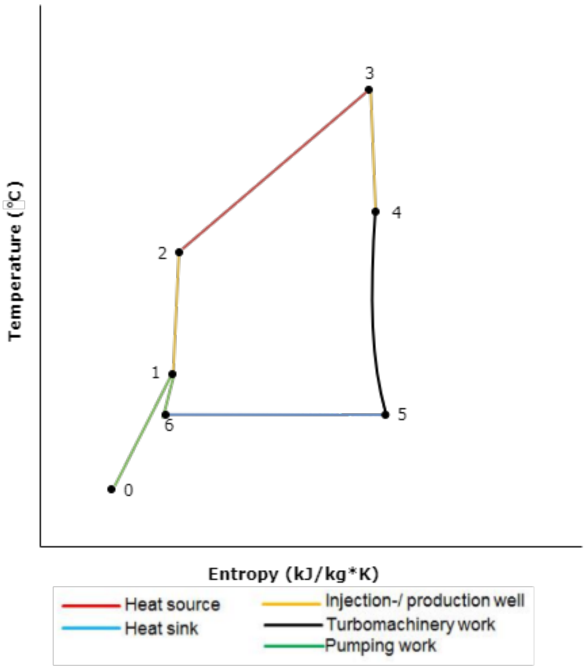

Figure 2.3: Example of CO_2 based geothermal thermodynamic cycle

0. $(P = P_{feed},\ T = T_{feed})$ Pure CO_2 comes into system from emitter (Gas phase in the Netherlands) at state 0, compression to injection pressure and dense state 1.

1. $(P = P_{tfinj},\ T = T_{tf})$ CO_2 travels through the injection well to bottomhole, compressing adiabatically from state 1 to 2 due to increasing hydrostatic pressure.

2. $(P = P_{inj},\ T = T_{inj})$ After reaching bottom hole injection pressure and temperature, the CO_2 is injected into the reservoir, heating up the CO_2 and increasing density. This process is best approached as an isometric heating from Injection conditions to production downhole conditions.

3. $(P = P_{bhp},\ T = T_{bhp})$ CO_2 moves up production well to entry of energy generation installation, expanding due to decompression.

4. $(P = P_{turbinein},\ T = T_{turbinein})$ CO_2 moves through turbine and/or heat exchange, extracting useable work and heat.

5. $(P = P_{turbineout},\ T = T_{turbineout})$ CO_2 gets cooled to reduce entropy/temperature by a cooling tower, condenser and/or heat exchanger for usable heat.

6. $(P = P_{cooled},\ T = T_{cooled})$ CO_2 gets compressed to state 1 injection conditions.

CO_2 feed and compression

The CO_2 enters into the system from outside sources (generally from industry or energy generation processes) after being purified and dried to prevent corrosion. In the Netherlands, current onshore CO_2 transportation is in gas phase with a maximum operating pressure of 20 bar, which is less efficient for transport compared to the liquid phase 100 to 120 bar range used onshore in other countries such as the US & Canada. This is not currently allowed in the Netherlands due to safety concerns, but might become a possibility in the future as CO_2 (re-)use takes off. For offshore CO_2 disposal, CO_2 can be compressed to the aforementioned range at coastal compressor stations, with the stated aim of delivering 80 bar pressure at offshore injection locations [27].

Before CO_2 injection, the CO_2 needs to be compressed to be brought to the required injection conditions. Gas compression is a mature commercial technology used in the natural gas industry. CO_2 compression uses similar equipment, save for modifications to account for the different chemical and physical properties of CO_2. For example, compressors for CO_2 are typically made with carbon steel to account for the corrosivity of CO_2 in the presence of trace water vapour [41].

Well traversion

As the CO_2 phase travels up or down the wellbore, rapidly changing pressure conditions induce compression or expansion of the fluid. Research shows that the well diameter and different resulting flow rates have a significant impact on the expansive cooling or compressive heating of the fluid [28]. Other research shows that heat transfer with the surrounding rock formations is limited, and near-adiabatic conditions are reached after just a few days of continuous circulation [61].

Turbine

There are two overarching types of geothermal power plant designs; direct systems where fluid from the subsurface is directly used to drive a turbine (e.g. dry steam and flash steam geothermal cycles), and indirect cycles where the reservoir fluid goes through a heat exchanger with a working fluid that usually has a lower boiling point than water, allowing turbine expansion work at lower temperatures (binary cycle). For water based geothermal electricity generation, 100° is usually considered the lower bound temperature, with the majority (ca.90%) of generation done by the direct cycle systems at temperatures above 150°C

[60]. A study exploring different CPG plant setups and comparing it's techno-economic performance found that direct cycle CPG makes a lot more economic sense [2]. This is caused by the conversion of heat to pressure during adiabatic expansion in the wellbore, and the previously explained thermosiphon effect. A binary heat exchanger cycle such as an ORC can not take advantage of pressure energy whereas a direct cycle turbine can.

Heat exchangers

After turbine expansion, CO_2 needs to be cooled, condensed and compressed for re-injection. This study will not go into the details of this, but theoretically the heat from this cooling stage could be used for heating purposes. It should however be noted that due to adiabatic cooling in the wellbore, as well as energy transferred out of the phase in the turbine, temperatures will be considerably lower than for a similar hydrothermal system.

Carbon Plume Geothermal in depleted gas reservoirs

Most of the existing research on CPG systems has focused on the injection of CO_2 into brine filled aquifers [2]. Ezekiel and Saar [28] studied the use of depleted gas reservoirs as target for CPG development. This has multiple advantages:

- Gas reservoirs have proven capacity of holding gasses on geological timescale
- CCS can alleviate problems with induced seismicity and subsidence due to reservoir re-pressurization
- Natural gas production in the early stages of development are beneficial to financial feasibility of CCS projects

Figure 2.4 shows a possible development path for a depleted-gas CPG system. The first stages constitute conventional natural gas recovery. Towards the end of the conventional reservoir lifetime, CO_2 is injected to concurrently with CNGR in order to drive out natural gas. After this stage the reservoir can either go into a conventional CCS stage, re-pressurizing the reservoir, or CPG can be directly started at depleted pressures. After thermal depletion of the reservoir, CO_2 is stored indefinitely akin to a conventional CCS project. Naturally, CPG systems can also start using brownfield depleted gas reservoirs, or even by 'heat mining' existing CCS sites. In this study focus is on the CPG stage and the EGR and repressurization steps are not studied and a repressurized, CO_2 filled reservoir is assumed unless stated otherwise.

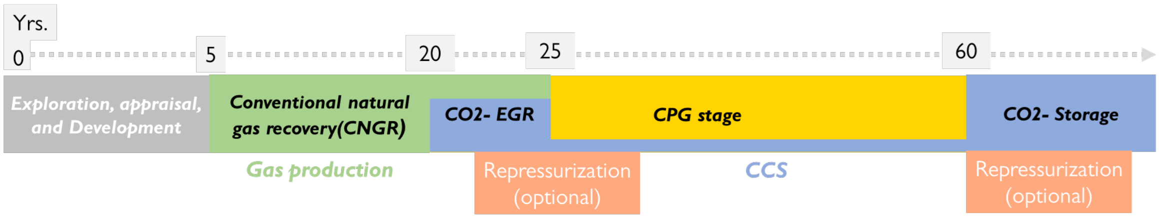
Yrs.
0
5
20
25
60
Exploration, appraisal, and Development
Conventional natural gas recovery(CNGR)
CO2- EGR
CPG stage
CO2- Storage
Gas production
Repressurization (optional)
CCS
Repressurization (optional)

Figure 2.4: Example of CPG being added to the lifecycle of a gas reservoir, modified after [28]

Methane-Carbon Dioxide interactions

Under reservoir conditions, both CH_4 and CO_2 persist in a gas like phase. This means that there is no existent interfacial tension between the front between the original reservoir fluid and injected carbon dioxide. This means that in simulation, the two components can be treated as a single phase, which can be referred to as gas, non-aqueous or supercritical. Please note that in this study, these terms are used interchangeably when referring to the fluid phase. It is noted that large density differences between the two components does inhibit mixing to some degree, meaning some semblance of a displacement front can be seen during the EGR stage [56]. Due to this lack of interfacial tension, the two components will readily mix, necessitating the use of a separator before the turbine stage.

Joule-Thompson cooling

When injecting CO_2 in depleted gas reservoirs, abandonment pressures below the critical pressure of CO_2 can give rise to strong expansion near the injection well. This expansion can give rise to the Joule-Thomson effect, which is the change in temperature of a substance caused by adiabatic expansion during a substantial reduction in pressure. This was extensively studied by Creusen [24]. This effect can be avoided by starting EGR at higher pressures, or by limiting injection rates when dealing with abandoned wells at very low pressure.

2.2 Heterogeneity

Most sedimentary reservoirs are laid down during a long-term deposition process, the characteristics of which vary with deposition environments in both space and time. These depositional environments can vary depending on the location of deposition as shown in Figure 2.5.

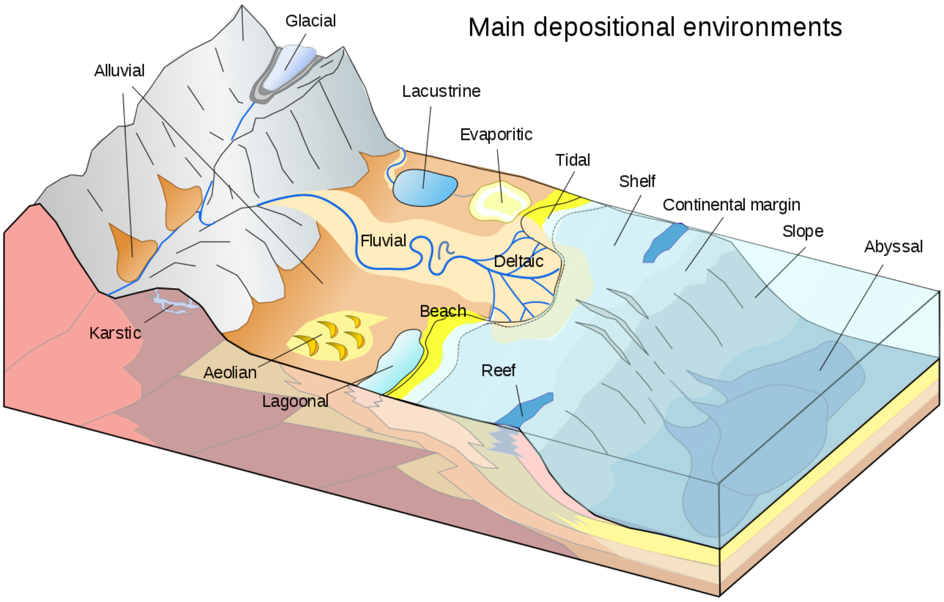

Figure 2.5: Different types of depositional environments within a sedimentary system [55]

Following deposition and subsequent burial, these reservoirs can be further altered by diagenetic processes such as compaction, dissolution and cementation. Heterogeneity is a blanket term for the spatial variability of reservoir properties caused by differences in depositional environments and subsequent diagenesis. If the reservoir has the same properties over the entire volume, it is said to be homogeneous. It should be noted that no reservoir can be called truly homogeneous, but can vary in heterogeneity. In a novel system such as CPG, where complicating thermal processes due to the geothermal nature are combined with the strong temperature-dependant properties of CO_2 it becomes difficult to generalize knowledge about brine-based geothermal or isothermal multiphase process behaviour in the presence of heterogeneity. In order to test for the effect of heterogeneity, it is first important to define it, and how one can quantify it.

2.2.1 Types of heterogeneity

The most important characteristic engineering implication for geological heterogeneity on reservoir behavior is the extreme variability in properties within the reservoir itself, both laterally and vertically, and within short distances. These properties may include permeability, porosity, relative permeability behaviour, faults and fractures, as well as thermal properties such as conductivity and heat capacity. Generally, heterogeneity quantification is focused on permeability. This is done because it is the very thing that defines flow, and as such is a product of other heterogeneities such as clay content, cementation and porosity. Secondly, the variability of permeability is commonly a lot larger than for other properties. A very heterogeneous reservoir might for example have porosity values between 0% and 30%, which would correspond to permeability variations of several orders of magnitude [44]. For geothermal purposes the second method of energy transfer, conduction, should also be considered. For a proper reservoir description, we need to predict the variation in these reservoir properties as a function of spatial locations and spatial resolutions. There are two classes of heterogeneity that can be defined; areal and vertical, stemming from the two principal geological directions; Same location over time and varying location at the same moment in time [6].

2.2.2 Scales of heterogeneity

Apart from different directions, heterogeneities can occur at any scale within the reservoir as seen in Figure 2.6. For isothermal flows, the impact of these heterogeneities is well studied. However, their impact on thermal characteristics, even more so for a fluid with strongly temperature-dependant properties such as CO_2, is less well known. It is important to take into account which heterogeneity scales are important for thermal CO_2 injection, as the possibility of conduction and convection versus only convection has implications for the effect of different types of heterogeneity on 'thermal sweep efficiency'.

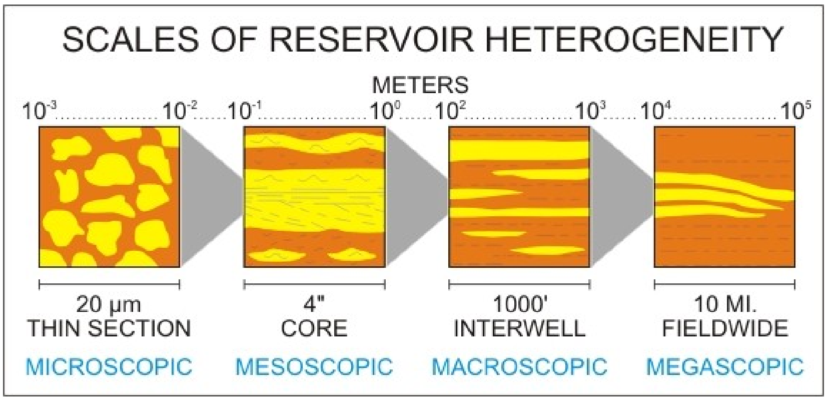

Figure 2.6: Image showing the different relevant scales for heterogeneity

Microscopic Heterogeneity

During hydrocarbon production, all scales are important for the determination of reservoir behaviour. On the microscopic scale, effects like cementation can induce connectivity issues in the pore structure, meaning the injection fluid does not displace all the original pore fluid. While this is detrimental for the sweep of hydrocarbons, on the timescale of a geothermal development heat conduction can easily siphon the heat from adjacent. Other effects to consider rock conductivity and heat capacity. Fluid conductivity should also be tested. for example, it was shown by [8] that water filled pores in sandstone can increase effective thermal conductivity by as much as 47%.

Mesoscopic Heterogeneity

On the mesoscopic scale, intra-formation heterogeneity due to e.g. different facies can induce anisotropy into the upscaled permeability, meaning that e.g. within a sandstone facies flow is possible in the horizontal, but not the vertical. While not directly a thermal property, this might reduce the effect of buoyancy caused by CO_2 heating up. As the density of CO_2 is strongly temperature dependant, it is important to test this effect. Another property which can suffer from anisotropy at this scale is thermal conductivity [17], where deposited bands of insulating minerals can act as 'insulating' layers against e.g. vertical conduction.

Macroscopic Heterogeneity

On the macroscopic scale, different facies can have different upscaled heterogeneities. Normally, a well is divided into productive and unproductive sections, where the volume fraction of productive layers is called the net-to-gross ratio (N/G). At this scale, the spatial location of producing and non-producing layers becomes an important factor. For example, a N/G = 0.5 reservoir consisting of a 50 m thick productive layer overlain by a 50 m thick unproductive layer will not be able to siphon all heat from the unproductive layer, whereas an alternation of ten 10 m thick layers has a far greater surface area available for heat conduction, greatly increasing total energy production. Another heterogeneity that can have large effects are the presence of fractures, which can dominate flow behaviour.

Megascopic Heterogeneity

On the megascopic scale, heterogeneities to consider are bounding faults and different formations can influence the large scale reservoir architecture, which determine the boundaries of the reservoir model and well placement. In this study, we will only consider the effect of within-reservoir heterogeneity. A short summary of the different heterogeneity scales and what to test for is shown in Table 2.7:

Scale	Variables to consider
Microscopic	Connate water saturation and it's effect on thermal behaviour. Relative permeability curves giving rise to different flow behaviour. Varying rock properties due to mineralogical differences.
Mesoscopic	Effects of permeability anisotropy, as well as possible effects of thermal conductivity anisotropy
Macroscopic	Effect of within-formation N/G and reservoir architecture on heat conduction.
Megascopic	Effect of driving mechanisms, large faults (out of scope for this study)

Table 2.7: Heterogeneity considerations across different scales

Vertical heterogeneity

The first dimension in which reservoirs are split up into representative units is the vertical. Due to the changes in depositional environments over time, a section of rock often shows dramatic changes in properties along the borehole. Usually, a reservoir is split up into different layers corresponding to different formations. These are then normally split up into producing and non-producing, which is the basis for the bulk N/G of a reservoir.

For the purpose of hydrocarbon recovery, two methods are commonly used to quantify vertical heterogeneity on the macroscale; the Dykstra-Parson permeability variation and the Lorenz coefficient [6]. Both of these methods are statistical ways of characterizing deviation from an idealized homogeneous reservoir. However, these methods do not take into account the way the different layers are ordered, which is an important factor for the actual heat conduction behaviour of the gross reservoir. A new method for quantifying the degree of layering is described in the following chapter on heterogeneity quantification will be discussed.

Garapati et al. [29] researched the effect of layering on CPG performance in a brine filled reservoir. He found that the system can be best upscaled with the arithmetic mean method. He also mentions that the buoyancy of CO_2 in brine means that the system is very sensitive to highly permeable formations near the top of the reservoir. In a CPG-methane-brine system however, the plume has a density between that of brine and methane, and will 'float' on top of the GWC. Also, a constant anisotropy ratio $\frac{k_x}{k_z}$ of 2 is assumed. In reality, mesoscale heterogeneity such as small bands of clayey material or stylolites can induce larger anisotropy, counteracting gravity effects.

Areal heterogeneity

Where layering in the vertical direction is commonly caused by changing depositional environments at one location over time, areal or horizontal heterogeneity within a formation is caused by changing facies over space at the same point in time. mathematically characterizing areal heterogeneity is exceedingly difficult, as the variability does not show patterns(e.g. layering), but it completely dependant on the lateral variation in the depositional environment, which can vary strongly as shown in Figure 2.8.

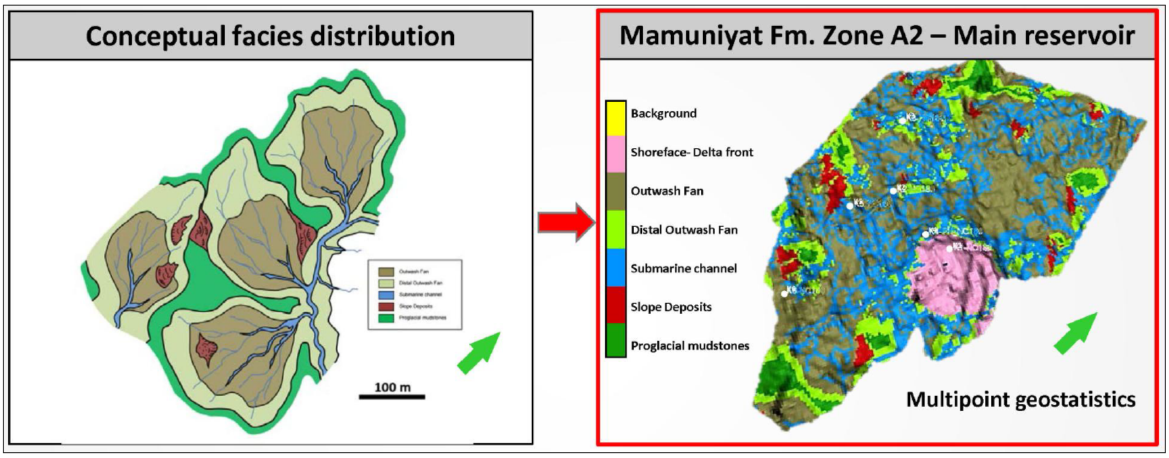
Conceptual facies distribution
Outwash Fan
Distal Outwash Fan
Submarine channel
Slope Deposits
Proglacial mudstones
100 m
Mamuniyat Fm. Zone A2 – Main reservoir
Background
Shoreface- Delta front
Outwash Fan
Distal Outwash Fan
Submarine channel
Slope Deposits
Proglacial mudstones
Multipoint geostatistics

Figure 2.8: Example from the Libyan K-field showing how areal heterogeneity translates to complex reservoir facies distribution [67]

It is very difficult to accurately translate the effects of areal heterogeneity in a 2D environment. That is why in this study, porosity-permeability heterogeneity will be tested on a 3D box model.

2.2.3 Quantifying Heterogeneity

There are several methods for establishing a geologically realistic reservoir model for a formation, e.g. a process based or stochastic approach. Process-based modeling is done by simulating the actual depositional process, which offers highly detailed geologically realistic reservoir models, but is very time consuming to create. Stochastic methods such as Sequential Indicator Simulation (SIS) and other variogram-based simulation techniques are easy to quantify and perform uncertainty analysis on, but lack of geological realism. Accurate simulation of complex geological features such as continuous channel sands is impossible using merely two-point statistical correlations. Another approach is object based modelling, where physical geological objects are placed in their respective depositional environment [37]. In this study, a simple SIS facies model combined with SIS porosity distribution is used to model reservoir property distribution. This will be further elaborated on in the Reservoir Model section.

2.3 Reservoir Model

When assessing the performance of a CPG system, it is not possible to use the majority of CCS research as an anologue. For a CPG system, not mass flow rate or sweep efficiency, but energy production is the quantity of interest. This has implications for the response of the system to uncertain variables. For example, impermeable but conductive layers and non-communicating reservoir sections can still contribute to energy production. On the other hand, new, thermal spatial variables such as heat capacity and thermal conductivity are introduced which can strongly affect heat reserves and transfer.

Likewise, conventional water-based geothermal system behaviour is also difficult to translate to a CPG system, due to drastically different thermal and flow properties between CO_2 and water under reservoir conditions, as well as the presence of multi-phase behaviour under the presence of a GWC and connate water saturation.

Thus, in order to explore the sensitivity of a CPG system to real life conditions, a sensitivity study and subsequent Uncertainty Quantification will be performed on a reservoir model. The Pernis (PRN) field in the Netherlands was chosen as basis for the box models used to explore sensitivity to different parameters, due to the available data and reservoir model. First, a quick introduction on the geological setting is given. Then, important model values are quantified for use in experiments.

2.3.1 Geological setting

Local Geology

The Pernis field is situated under Rotterdam as seen in section 2.3.1 in the West-Netherlands basin (WNB), a sedimentary basin stretching from the province of Brabant, through Zuid-Holland, far into the North Sea. The Pernis gas field is part of the Rijnland Group, which is part of the WNB and was deposited during the lower Cretaceous, between 130-100MA. The hydrocarbons have migrated upwards into the formation, originating from Carboniferous and Jurassic deposits such as the Posidonia Shale [40]. The Rijnland group was deposited in environments varying from coastal to outer-neritic environments, with variation in deposits caused by changes in sea level and onshore sediment production. The Pernis field is overlain by the Chalk Group and North Sea Group. Well data on the underburden has not been obtained, but likely consists of the Schieland group, as is shown by a crossections from [40] made with data from deeper wells in the adjacent Pernis-West field. For the purpose of this study, we are mainly interested in the thermal properties of the underburden, so a basic description of the lithology suffices. As both of these groups are characterized by For this study, the reservoir geology and both over- and underburden are relevant for their disposition to flow, sealing capacity and thermal properties.

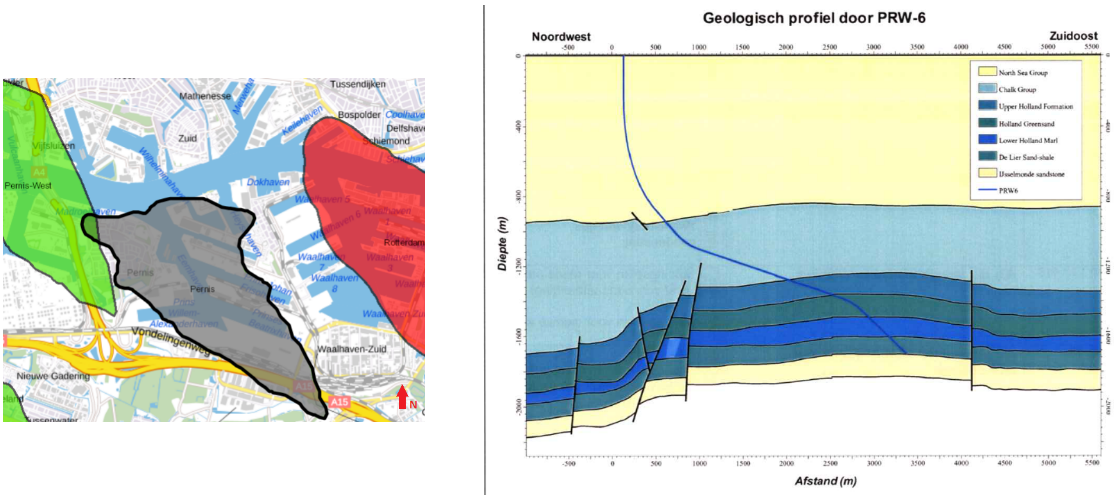
Mathenesse
Tussendijken
Bospolder
Delfshaven
Schiemond
Zuid
Vijfsluizen
Pernis-West
Dokhaven
Waalhaven
Rotterdam
Pernis
Vondelingenweg
Waalhaven-Zuid
Nieuwe Gadering
A4
A15
N
Geologisch profiel door PRW-6
Noordwest
Zuidoost
Diepte (m)
Afstand (m)
-500
0
500
1000
1500
2000
2500
3000
3500
4000
4500
5000
5500
400
800
1200
1600
2000
North Sea Group
Chalk Group
Upper Holland Formation
Holland Greensand
Lower Holland Marl
De Lier Sand-shale
IJsselmonde sandstone
PRW6

Figure 2.9: Figures showing geographical location of the PRN in Rotterdam, with neighbouring fields Pernis-West (PRW) and the Rotterdam Field (RTD) (left) and seismic interpretation of PRN (right)

As shown in section 2.3.1, the Rijnland Group in the Pernis field can be further separated into 5 different members with differing depositional environment and subsequent reservoir properties. A succinct geological description of the underburden, overburden and five reservoir groups is given following [16] in Table 2.10.

Table 2.10: Pernis reservoir lithology according to [16]

	Geological Unit	**Abbrev.**	**Age**	Thickness	**Depositional environment**	**Lithology**
		-	Ma	m	-	-
Under-burden	Schieland Group	SL	161-130	100+	Prograding proximal marine setting	Grey and variegated claystones, coaly to clayey sandstones, rare coal seams and local calcareous intercalations
Reservoir	Ijsselmonde Sandstone Member	KNNSY	±128	100-200	Prograding shallow marine, shoreface backbarrier environment	Massive fine- to medium grained sandstone formation, alternated by 5-10m thick claystone beds caused by bioturbation and lagoons
	De Lier Member	KNNSL	±125	50-100	Prograding coastal system to continental shelf	Alternating claystones with very fine to fine grained sandstones with frequent siderite concretions
	Lower Holland Marl	KNGLL	125-113	100-200	Transition from middle to outer continental shelf	Alternating sandy,silty claystones with argillacious sandstones
	Holland Greensand	KNGLG	113-100	up to 130	Moderate to deep marine, during sea level rise	Fine to very fine grained sandstones with local siltstones and claystones, strongly bioturbated
	Mid Holland Claystone	KNGLM	113-100	50-100	Moderate to deep marine	Marls and marly claystones, very fine grained
Over burden	Chalk Group	CK	100-60	50-300	Retrograding shallow marine	Carbonate-dominated, e.g. bioclastic and marly limestones

Reservoir structure

Within the reservoir, the de Lier and Holland Greensand have been used as productive storage layers during historic production, and have been perforated to that end. The seals for these layers are the Lower Holland Marl and Mid-Holland Claystone respectively. The fines and carbonates in these layers have sufficiently low permeability to prevent further hydrocarbon migration. For the purposes of the reservoir simulation, the non-productive layers will be assumed to have a zero permeability and S_w of 1. Porosity will taken into account, as immobile water still has an effect of the thermal properties of the bulk volume.

The Rijnland formation was deposited during the extensional regime caused by the Late Kimmerian rifting phase. During the deposition of the overlying Chalk formation, the regio underwent tectonic inversion, causing complete or partial removal of the Rijnland Group in some places in the region. This inversion has caused heavy NW-SE faulting across the entire region, including the Rijnland group. This faulting caused strong deformation of the system, with faults, anticlines and synclines.

2.3.2 Modelling values

The top of the Rijnland group is located at a depth of +- 1300m down to around 1700m. With pressures running from 142 to 146 bar. Temperatures vary between 60 and 70 degrees. This is too low to properly compare to other literature on CPG. This means that in this study, the reservoir is assumed to be deeper, resulting in a pressure of 250 bar and a temperature of $110°C$.
A petrophysical analysis was performed by [16] using five wells from the adjacent Pernis West and Rotterdan fields, with an additional well PRW-06 which perforates the PRN field. GR, SP and caliper logs were used to identify facies and permeable zones due to lacking core data. Sonic, Density and Neutron logs were used to calculate porosity. Additionally, a petrophysical evaluation by the NAM on the KNNSL and KNGLG formations in a nearby group was used to get some extra information about reservoir quantities. It should be taken into account that these values are from a different location, which induces some uncertainty in the values used [54].

Porosity-Permeability

Density and thermal neutron logs from well PRW-06 can be used to determine the porosity and permeability. This is done by averaging density and neutron log porosity readings, and accounting for clay volume reducing the effective porosity with Equation 2.1

$$\phi_E = \phi_T \left(1 - V_{sh}\right). \tag{2.1}$$

De Boer et al. [16] found porosities from nearby wells shown in Figure 2.11 with the majority of measurements between 0.15-0.3 for the Greensand and 0.1-0.25 for the de Lier member. They determined poro-perm relations for the two layers [16] with Equation 2.2 (note: these equations are different from the ones used in [54] in the Monster field):

$$\begin{aligned} k_{\text{Greensand}} &= 10^{-3.81+18.9*\phi} \\ k_{\text{DeLier}} &= 10^{-3.11+18.4*\phi}. \end{aligned} \tag{2.2}$$

The resulting permeability is given in mD.

Saturation and relperm

De Boer et al. [16] uses multiple values for the saturation parameters during uncertainty quantification. In this study, we assume absence of oil in the reservoir, and as such only values relating to gas and water are shown in Table 2.12.

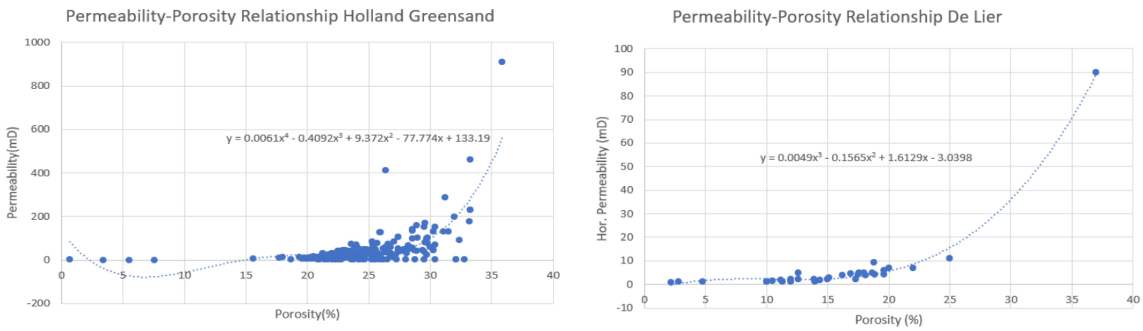

(a) Poro-perm relationship of HG based on Well RTD-06

(b) Poro-perm relationship of DL based on Well DL-17

Figure 2.11: Porosity-permeability graph of PRN storage layers from [16]

	min	avg	max
Initial gas saturation ($S_{g,i}$)	0.55	0.7	0.85
Initial water saturation ($S_{w,i}$)	0.45	0.3	0.15
Residual Gas saturation ($S_{g,r}$)	0.1	0.175	0.25
Connate Water saturation ($S_{w,c}$)	0.15	0.175	0.2

Table 2.12: Saturation values for the Pernis field from [16]

In the study, the micro-DARSim Pore-Network Simulator was used to fit the Brooks-Corey curves to capillary pressure data. Assumed values in the study are $n_w = 1.9$, $n_g = 3$ and 1 for both endpoint drainage permeabilities. The study also notes that introducing CO_2 in the gas mixture leads to a sharp increase in non-wettability of the vapor phase, leading to changes in relative permeabilities and residual saturations.

Water saturation can be calculated from effective porosity and resistivity logs using the Waxman-Smits method. However, due to the lack of Waxman-Smits parameters in the logs for Pernis, saturation-height functions established for the equivalent layers (Holland Greensand and de Lier) in the adjacent Rotterdam Field. The Holland Greensand saturation height function is given by:

$$Sw = (1.289506915 - 2.47139 * \phi) * (HAGWC/22.3)^{0.01949198 - 2.743 * \phi^2}, \tag{2.3}$$

with the HAGWC being the height in m above the theoretical GWC at 1437 m. For the de Lier formation, the water saturation height function is defined by Equation 2.4

$$Sw = \left((1.3 - 4.2 * \phi) + ((HAGWC)/38.3 * (37.5 - 79.6 * \phi))^{-0.8}\right) - 0.1, \tag{2.4}$$

where HAGWC is the height in meters above a theoretical GWC at 1641 m.

Thermal Properties

Two thermal properties are important for the performance of any geothermal system; thermal conductivity and heat capacity. Thermal conductivity determines the speed of heat exchange under a temperature gradient, and is very important for heat production [76]. This variable varies with mineral composition, fluid presence, pressure and temperature. However, no studies have been done on the thermal properties of certain rocks in the WNB. As such, it is assumed he studied reservoir storage layers contain shale or sandstone. For simplicity, these two rock types are assumed to have a normal distribution taken from [77], namely for shale

(μ_{sh} = 190.1 kJ/m/day/K, σ_{sh} = 8.64 kJ/m/day/K) and sandstone (μ_{sst} = 259.2 kJ/m/day/K, σ_{sst} = 8.64 kJ/m/day/K). For the homogeneous models used in testing the mean is used as the constant value.

The other important thermal property is the specific heat capacity of rocks, which is a measure of the amount of energy required to change the temperature of a unit of mass. This varies for changing temperatures, pressures and mineralogy. Little is known about the variation of specific heat capacity in the WNB. Willems et al. [79] assumed two different values for the two different lithologies, being $C_{sst} = 1.93 MJ/m^3/K$ and $C_{sh} = 2.47 MJ/M^3/K$.

Salinity

Schlumberger [54] performed a petrophysical evaluation of formation water salinity in the nearby Monster field, and found salinities of 80 ppm for both formations, which translates to 1.368 mol/kg. As water will not be used as working fluid, specific salinity mainly affects the solubility of CO_2, and any effects that might arise from interaction with an aquifer.

Chapter 3

Simulation Model

This chapter concerns itself with the description of the active model built with the Delft Advanced Research Terra Simulator (DARTS) with the goal of simulating real world behaviour of a CPG system. Firstly, the model will be described, stating the main assumptions, simplifications made, and discussing the objectives of the model. Following this, the governing equations for the mass and energy balance will be worked out together with the simulation strategy used for solving them. The next section Thermodynamics elaborates on the thermodynamic model describing component phase partitioning. To conclude, the physical properties of the active model are discusses, which is split up into a parts flow properties and phase-specific properties. The used equations are validated in chapter 5. Complementary to this model are a variety of static models and experiments used to generate insights. These models will be further elaborated on in chapter 4. In order to ensure the model is working correctly, it's of paramount importance to validate the component phase partitioning, as well as the different flow and thermal properties of the entire system. Where possible, experimental data is compared to similar model outputs. If data is not available, a visual comparison with graphs from other papers is made. First, the component phase partitioning of the EOS will be tested. Following that, properties will be validated for the range 50-400 bar and 35-130$^\circ C$. The model validation is extensively described in Appendix B.

3.1 Model Description

The injection of CO_2 in a depleted gas reservoir system can be described as a multi-component, multi-phase system. For our simulation, we consider a system consisting of four components: CO_2, CH_4, H_2O and NaCL. In a real gas reservoir, multiple components such as H_2S, N2 and other hydrocarbons can be present. Impurities such as H_2S, SO_2 and N_2 [53] can be present in the injected CO_2 stream, and the brine can contain a wide variety of dissolved minerals depending on the regional mineralogy, such as dissolved carbonates and other salts. For convenience and computational efficiency, these trace components are omitted, and it is assumed that these four dominant components are sufficient to adequately describe the system.

Several phases can occur in the reservoir during the project lifetime depending on local conditions. These phases can be a liquid aqueous phase (AqP), a non-aqueous liquid phase (NAqP), a non-aqueous gas phase (g) and a separate solid salt phase (s) [24]. The aqueous phase is a brine consisting predominantly of water (H_2O) with dissolved salt components and traces of dissolved non-aqueous components (i.e. CO_2 and CH_4). For the purposes of this simulation, the dissolved salt is assumed to consist of 100% NaCl. The non-aqueous phase consists of a mixture of the non-aqueous components (CO_2 and CH_4), of which the composition can vary from pure CO_2 to pure CH_4. Additionally, the non-aqueous phase can contain some dissolved or vaporized H_2O.

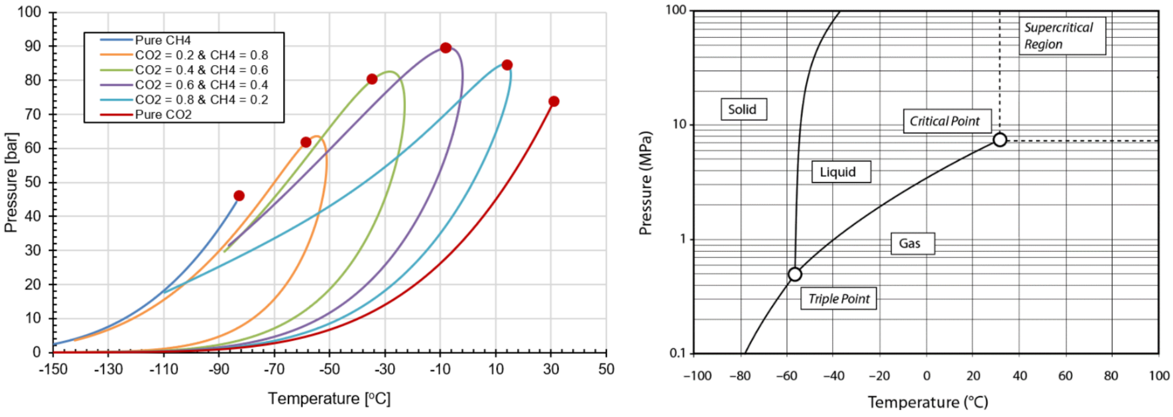

Figure 3.1: Figures showing the phase envelope and critical points for binary CO_2-CH_4 mixtures (left) and a phase diagram for pure CO_2 (right) from [24]

Depending on local conditions all of these phases can coexist in the reservoir. This can vary from a single phase system (i.e. only the gas phase) to a four phase system where the liquid aqueous phase, non-aqueous phases in both liquid and vapor conditions and solid phase are present. for temperatures above $31°C$, the non-aqueous liquid phase can not exist. In order to simplify the model, temperature and pressure limits can be chosen to limit the amount of possible phases. As can be seen in Figure 3.1 for reservoir conditions CO_2 is nearly always supercritical, except for cold injection in very low-pressure reservoirs. Problems arising from this effect are discussed in chapter 2.

3.1.1 Modelling objectives and assumptions

In order to be able to properly study thermal behaviour of CO_2 injection, several processes need to be modelled:

1. Phase behaviour resulting from component equilibrium phase partitioning under varying temperature, pressure and salinity
2. Convective flow of mass through the formation
3. Convective and conductive flow of energy through the formation

The assumptions made to simplify the modelling of these processes are as follows:

1. Darcy's law applies
2. No chemical reactions occur in the reservoir
3. Instantaneous thermodynamic equilibrium
4. Brine salinity stays constant over space and time
5. Slight compressibility of reservoir rock
6. Diffusive mass transfer is neglected
7. Unless stated otherwise, the effect of capillary pressure is neglected (relative permeability curves still apply)

3.2 Governing Equations

The proposed system can be characterized as a CO_2 injection into a dry gas hydrocarbon reservoir with a present GWC. In order to simplify the initial system, it is assumed only three components (CO_2, CH_4, Brine) and two phases (NAqP, AqP) are present. Supercritical phases do not have interfacial tension and thus can be considered to be the same phase as gas. The initial gas phase is assumed to consist of CH_4 with trace water vapour. The initial aqueous phase consists of H_2O with dissolved NaCL and trace CH_4 [24]. Due to desire to study thermal effects, both mass and energy conservation equations will need to be considered.

3.2.1 Mass Balance Equation

The MBE for a control volume with n_p phases and n_c components can be written as Equation 3.1:

$$\frac{\partial m_c}{\partial t} + \nabla \cdot l_c + q_c = 0, \quad c = 1, \ldots, n_c, \tag{3.1}$$

where for a given control volume, m_c is the molar mass of component c, l_c is the total flux of component c, and q_c is the source/sink term for component c. This means that for any system, there are n_c-dimensional vectors defining flow in porous media for these components Equation 3.2:

$$m_c = \phi \sum_{p=1}^{n_p} \rho_p s_p x_{cp}, \tag{3.2a}$$

$$l_c = \sum_{p=1}^{n_p} \left(\rho_p x_{cp} \mathbf{u}_p + s_p \rho_p \mathbf{J}_{cp} \right), \tag{3.2b}$$

$$q_c = \sum_{p=1}^{n_p} \rho_p x_{cp} q_p. \tag{3.2c}$$

After substitution, it gives rise to the following equation:

$$\frac{\partial}{\partial t} \left(\phi \sum_{p=1}^{n_p} x_{cp} \rho_p s_p \right) + \nabla \cdot \sum_{p=1}^{n_p} \left(x_{cp} \rho_p \mathbf{u}_p + s_p \rho_p \mathbf{J}_{cp} \right) + \sum_{p=1}^{n_p} x_{cp} \rho_p q_p = 0, \quad c = 1, \ldots, n_c. \tag{3.3}$$

Here, $\mathbf{u}_p$ describes fluid flow in the reservoir using Darcy's law as defined by Equation 3.4:

$$\mathbf{u}_p = -K \frac{k_{rp}}{\mu_p} \left(\nabla p_p - \gamma_p \nabla D \right), \quad p = 1, \ldots, n_p. \tag{3.4}$$

The diffusion is determined by the diffusion tensor $\mathbf{J}_{cp}$ which is defined for component c in phase p by Equation 3.5 (for our model, diffusion is neglected and this value is set to 0):

$$\mathbf{J}_{cp} = -\phi D_{cp} \nabla x_{cp} = 0. \tag{3.5}$$

The saturation of phase p, used for several flow related properties (e.g. k_{rp}), is the volume fraction of void occupied by phase p and defined by the following relations Equation 3.6:

$$s_p = \frac{v_p / \rho_p}{\sum_{p=1}^{n_p} v_p / \rho_p}, \tag{3.6a}$$

$$\sum_{p=1}^{n_p} s_p = 1. \tag{3.6b}$$

Porosity is not a constant variable. As pressure changes, the rock compresses or expands, changing porosity as defined by Equation 3.7. c_r is rock compressibillity. For a depleted gas reservoir, the reference pressure p_{ref} is taken to be the reservoir pressure before development

$$\phi = \phi_0(1 + c_r(p - p_{ref})). \tag{3.7}$$

3.2.2 Energy Conservation Equation

In the absence of work done on and by the system, the energy conservation equation for a system with N_p phases can be described in vector notation by Equation 3.8:

$$\frac{\partial U}{\partial t} + \nabla \cdot \Phi + q + \tilde{Q} = 0, \tag{3.8}$$

where U describes the change of system internal energy over time, Φ describes heat advection due to mass transport, q describes heat conduction and $\tilde{Q_p}$ function as an energy source/sink term.

For a porous media system with n_p phases these components are described by Equation 3.9:

$$\begin{aligned}
U &= \phi \sum_{p=1}^{n_p} \rho_p s_p U_p + (1-\phi)U_r, && (3.9a)\\
\Phi &= \sum_{p=1}^{N_p} h_p \rho_p u_p, && (3.9b)\\
q &= -\nabla \cdot (\kappa \nabla T), && (3.9c)\\
\tilde{Q} &= \sum_{p=1}^{n_p} h_p \rho_p \tilde{q_p}. && (3.9d)
\end{aligned}$$

Substituting Equation 3.9 into Equation 3.8, we have got the ECE in Equation 3.10:

$$\frac{\partial}{\partial t}\left(\phi \sum_{p=1}^{n_p} \rho_p s_p U_p + (1-\phi)U_r\right) + \nabla \cdot \sum_{p=1}^{n_p} h_p \rho_p u_p - \nabla \cdot (\kappa \nabla T) + \sum_{p=1}^{n_p} h_p \rho_p \tilde{q_p} = 0. \tag{3.10}$$

3.2.3 Operator Based Linearization

The system of nonlinear equations is solved by means of a molar formulation, meaning all variables are computed with mol as measurement of mass. The primary variables required for solving are pressure, temperature and composition. In order to linearize the nonlinear system of equations, the Newton-Rhapson method is conventionally used. The resulting linear system of equations on each iteration is expressed by:

$$J\left(\omega^k\right)\left(\omega^{k+1} - \omega^k\right) + r\left(\omega^k\right) = 0. \tag{3.11}$$

In the conventional linearization approach, the Jacobian is assembled with accurate evaluation of all property values and their derivatives with respect to the nonlinear unknowns, whereas often the variation in these variables per timestep is small and/or negligible due to the commonly large uncertainties associated with subsurface engineering problems [76]. In highly non-linear systens, such as models with high fidelity or models where behaviour is strongly dependant on the primary variables (such as with CO_2), this procedure often requires many iterations for convergence, slowing down simulation. In this study, the Operator Based Linearization (OBL) approach proposed by Voskov [73] is used as a way to reduce the iterative demands of solving highly nonlinear systems. The method is based on the idea of grouping elements from different terms in the conservation equations into operators that are fully defined by functions of the physical state.

In order to solve the system, the mass and energy conservation equations Equation 3.3 and Equation 3.10 are reordered and written as a set of operators dependant on physical state $\boldsymbol{\omega}$. The mass balance conservation in discretized operator form with upstream weighting of the physical state for determination of flux-related properties is written as Equation 3.12 [75]:

$$V\phi_0\left[\alpha_c(\omega)-\alpha_c\left(\omega_n\right)\right]-\Delta t \sum_{l\in L(i)}\sum_{j=1}^{n_p}\left[\Gamma^l\beta_{cj}^l\left(\omega^u\right)\Delta\psi_j^l+\Gamma_d^l\gamma_j^l(\omega)\Delta\chi_{cj}\right]=0, \tag{3.12}$$

where V is the control volume, ω_n is the physical state of block i at the previous timestep, ω is the physical state of block i at the new timestep, ω^u is the physical state of the upstream block, Γ^l and Γ_d^l are respectively the fluid and diffusive transmisibilities, and $L(i)$ is interface i of the control volume.

Here the subscript n denotes the value at the previous timestep. For simplicity sake, as well as limitations of the current engine, capillarity and diffusion are disregarded. This reduces the diffusion term(γ_{cp}^l) to zero, meaning that the operators that define the mass balance without chemical reactions can be defined by Equation 3.13:

$$\alpha_{cf}(\omega)=\left(1+c_r\left(p-p_{ref}\right)\right)\sum_{j=1}^{n_p}x_{cj}\rho_j s_j,\ c=1,\ldots,n_c, \tag{3.13a}$$

$$\beta_{cj}(\omega)=x_{cj}\rho_j k_{rj}/\mu_j,\ c=1,\ldots,n_c,\ j=1,\ldots,n_p, \tag{3.13b}$$

$$\gamma_j(\omega)=\left(1+c_r\left(p-p_{ref}\right)\right)s_j,\ j=1,\ldots,n_p, \tag{3.13c}$$

$$\chi_{cj}(\omega)=D_{cj}\rho_j x_{cj},\ c=1,\ldots,n_c,\ j=1,\ldots,n_p. \tag{3.13d}$$

It should be noted that diffusion operator χ_{cj} is always zero in our model due to disregarding this effect. Modelling the effect of gravity and capillary effect in DARTS is done with the phase-potential-upwinding (PPU) strategy [43] [47]. The potential difference of phase j on interface $l(i)$ between block 1 and 2 can written as:

$$\Delta\psi_j^l=p_1-p_1^c\left(\omega_1\right)-\left(p_2-p_2^c\left(\omega_2\right)\right)-\frac{\rho_j\left(\omega_1\right)+\rho_j\left(\omega_2\right)}{2}g\left(z_2-z_1\right), \tag{3.14}$$

where p_j^c and ρ_j denote capillary pressure and density of phase j respectively. These state dependant variables are added as operators to the system. In this model, unless otherwise specified, capillary pressure is neglected and set to 0. State only dependant variables are used in the OBL framework for interpolation. This means that in this configuration, the model will have n_c of α, $(n_c \times n_p)$ of β, n_p of γ, $(n_c \times n_p)$ of χ, n_p of p^c and n_p of ρ operators required for the MBE. The operators related to unused physics are defined as zero to keep the system consistent.

The discretized energy conservation equation without chemical reactions in operator form is given by Equation 3.16:

$$V\phi_0\left[\alpha_{ef}(\omega)-\alpha_{ef}(\omega_n)\right]-\Delta t\sum_{l\in L(i)}\sum_{j=1}^{n_p}\left[\Gamma^l\beta_{ej}^l\left(\omega^u\right)\Delta\psi_j^l+\Gamma_d^l\gamma_j(\omega)\Delta\chi_{ej}\right]+ \tag{3.15}$$

$$\left(1-\phi_0\right)VU_r\left[\alpha_{er}(\omega)-\alpha_{er}\left(\omega_n\right)\right]-\Delta t\sum_l\left(1-\phi_0\right)\Gamma_d^l\kappa_r\alpha_{er}(\omega)\Delta\chi_{er}=0.$$

Here the operators are defined by Equation 3.16:

$$\alpha_{ef}(\omega) = (1 + c_r (p - p_{ref})) \sum_{j=1}^{n_p} \rho_j s_j U_j, \tag{3.16a}$$

$$\beta_{ej}(\omega) = h_j \rho_j k_{rj} / \mu_j, \ j = 1, \ldots, n_p, \tag{3.16b}$$

$$\chi_{ej}(\omega) = \kappa_j T_j, \ j = 1, \ldots, n_p. \tag{3.16c}$$

In the simulation, the rock internal energy as well as rock conductivity, are defined as separate state dependant variables given by:

$$\alpha_{eri}(\omega) = \frac{U_r}{1 + c_r (p - p_{ref})}, \quad \alpha_{erc}(\omega) = \frac{1}{1 + c_r (p - p_{ref})}, \ \chi_{er}(\omega) = T_r, \tag{3.17}$$

where α_{eri} and α_{erc} represent respectively the rock internal energy and thermal conductivity. This means that in order to solve the energy conservation equation, 1 of α_e, n_p of β_e, n_p of χ_e and 3 operators for rock energy need to be defined.

3.3 Thermodynamic Model

In systems consisting of multiple phases and components, the fraction of components in each phase the system converges to for a certain pressure and temperature is called the local thermodynamic equilibrium. The value of this equilibrium can be described with the chemical potential of every component as partitioned in each phase. The chemical potential of a component c in phase α is defined by Equation 3.18

$$\mu_{c,\alpha} \equiv \mu_{c,\alpha}^0 + RT \ln(f_{i,\alpha}) \quad c = 1, \ldots, n_c, \tag{3.18}$$

where $\mu_{i,\alpha}^0$ and $f_{i,\alpha}$ denote respectively the chemical potential and fugacity of component c in phase α at reference temperature, and T and R respectively denote the temperature and gas constant. The fugacity is computed with Equation 3.19:

$$f_{c,\alpha} = p \phi_c x_{c,\alpha}, \tag{3.19}$$

where ϕ_c denotes the fugacity coefficient of component c.

Thermodynamic equilibrium is defined as the point where the chemical potentials of a component in every phase is equal. For example, thermodynamic equilibrium for a component between phases α and β is defined by Equation 3.20

$$\mu_{c,\alpha}(P, T) - \mu_{c,\beta}(P, T) \equiv 0 \quad c = 1, \ldots, n_c. \tag{3.20}$$

Accurate thermodynamic models for the phase partitioning behaviour of the varying component for models with brine and a single gas component exist. However, most of these models are valid only under absence of extra components and impurities. The modelling of CO_2 injection into a depleted gas reservoir requires a thermodynamic equilibrium model capable of handling a multi-component gas phase consisting of CO_2, CH_4 and potentially impurities such as SO_2 and N_2 in conjuction with the aqueous brine phase [24].

Models with these capabilities have previously been developed, such as by ZiabakhshGanji [82] and Battistelli [12]. The ZiabakhshGanji model is publicly available and ignores some second order component-component interactions, e.g. by assuming the fugacity of the components in the vapour phase are independant of composition. This eliminates some iterative demands for extra efficiency, and makes the model straightforward for implementation. The model uses two different approaches for the computation of the thermodynamic equilibrium of H_2O and other gaseous components respectively, due to the limiting applicability of certain physical laws with regards to the aqueous component, which will be discussed in a separate section.

3.3.1 Non-aqueous component phase partitioning

By choosing the phases to be Aq and NAq (where NAq can be any non-aqueous phase, such as gas, liquid or supercritical), and substituting Equation 3.18 for each phase into Equation 3.20, we get the following expression Equation 3.18 for a component c (excluding H_2O):

$$\frac{\mu^o_{c,NAq} - \mu^o_{c,Aq}}{RT} = \ln\left(\frac{f_{c,Aq}}{f_{c,NA}}\right). \tag{3.21}$$

Since the solubility of the non-aqueous components in our model is relatively low, the fugacity for the gaseous components in the aqueous phase can be replaced by the activity a [70], which is given by Equation 3.22, where N_w and γ_c are the molality of the water and the component activity coefficient:

$$f_{c,Aq} = a_c = N_w \gamma_c x_{c,Aq}. \tag{3.22}$$

Substituting Equation 3.19 and Equation 3.22 into Equation 3.18 gives rise to an expression for the equilibrium constant K^0_c:

$$\frac{\mu^0_{c,NAq} - \mu^0_{c,Aq}}{RT} = \ln\left(\frac{N_w \gamma_c x_{c,Aq}}{p \phi_c x_{c,NAq}}\right) = \ln\left(K^o_c\right). \tag{3.23}$$

K^0_c can be described in terms of Henry's constant $K^0_c = \frac{k_h}{N_w}$. equating this to the the inside of the ln term of Equation 3.23 and rewriting to separate the mass fractions we get the following equation for the equilibrium of a non-aqueous component between the aqueous and another phase:

$$K_c = \frac{x_{c,Naq}}{x_{c,Aq}} = \frac{k_{H,c}\gamma_c}{p\phi_c}, \quad c \neq H_2O, \tag{3.24}$$

where the fugacity coefficient ϕ_c, Henry's constant k_H and γ_c need to be computed separately.

Fugacity coefficient

The fugacity coefficient must be derived from the PVT properties of the system by utilizing an equation of state. Many different types of EOS's exist, such as Cubic equations in volume (Redlich-Kwong [63], Peng-Robinson [59]) and modified Van der Waals EOS models such as Soave Redlich-Kwong [68]. Other studies create models based on modified RK EOS to represent gas mixture properties. Here, the PR EOS is chosen due to it's good accuracy around the vapour-liquid boundary. It should be noted that cubic equations struggle to accurately represent fluid behaviour around the critical point, which might give rise to a source of error for simulations close to the CO_2 critical point[42]. Following PR, the equation for the fugacity coefficient is given by Equation 3.25:

$$\ln\left(\phi_i\right) = \frac{B_i}{B}(Z-1) - \ln(Z-B) + \frac{A}{2.828B}\left[\frac{B_i}{B} - \frac{2\sum_j x_{i,NA} a_{ij}}{a}\right] \ln\left[\frac{Z+2.414B}{Z-0.414B}\right]. \tag{3.25}$$

The expression for compressibility factor Z is given by [59] as:

$$Z^3 - (1-B)Z^2 + \left(A - 2B - 3B^2\right)Z - \left(AB - B^2 - B^3\right) = 0, \tag{3.26}$$

where parameters A and B are functions of pressure and temperature defined by Equation 3.27:

$$A = \frac{a(T)P}{(RT)^2}, \quad B = \frac{bP}{RT}, \tag{3.27}$$

where

$$a(T) = 0.45724\frac{R^2T_c^2}{P_c}\alpha(T), \quad b = 0.07780\frac{RT_c}{P_c}, \tag{3.28}$$

and

$$\alpha(T) = \left[1 + \left(0.37646 + 1.4522\omega - 0.26992\omega^2\right)\left(1 - \sqrt{\frac{T}{T_c}}\right)\right]^2. \tag{3.29}$$

In Equation 3.3.1 and Equation 3.29 (T_c, P_c) denote respectively the critical temperature and pressure, and ω is the accentric factor. For mixed systems, mixing rules given in Equation 3.30 are used to obtain values for a and b representative for the system:

$$a = \sum_i\sum_j y_i y_j a_{ij}, \quad a_{ij} = \sqrt{a_i a_j}\left(1 - k_{ij}\right), \quad b = \sum_i b_i y_i, \tag{3.30}$$

with k_{ij} denoting the binary interaction coefficient between component i and j, the values of which are shown in Table A.4.

Due to being a cubic equation, Equation 3.26 can give either one or three possible root values for Z as a solution. a strategy for finding the correct root is proposed by [12]. If only one root remains, this is taken to be the value for Z. If three roots are given, the intermediate, imaginary root is discarded, leaving two real values for compressibility; the low value Z_l and the high value Z_h. Here, the Z_l is taken to be the compressibility of the liquid phase, and Z_h is the compressibility of the gas phase. As the fugacity coefficient in our system is only needed for the gasueous phase Z_h is chosen. Optionally, NAq phase density can be optionally corrected with a volume shift technique from [58], which can be used if extra accuracy is desired, but this is not part of the scope of this study.

Henry's constant and activity coefficient

For the top part of Equation 3.24, Henry's constant k_h and the activity coefficient γ_i also need to be determined. [7] gives Equation 3.31 as a virial-like correlation for the thermodynamic properties of the aqueous phase components at infinite dilution with the use of empirical parameters which are independant of pressure and temperature:

$$\ln\left(k_H\right) = (1-\eta)\ln f^0_{H2O} + \eta\ln\left(\frac{RT}{Mw}\rho^0_{H2O}\right) + 2\rho^0_{H2O}\Delta B, \tag{3.31}$$

where η is a constant for each dissolved gas in water, and f^0_{H2O} and ρ^0_{H2O} are the fugacity and density of pure water respectively. ΔB is a measurement of the difference in interaction between dissimilar solvent molecules, given by Equation 3.32:

$$\Delta B = \tau + \Gamma P + \beta\sqrt{\frac{10^3}{T}}, \tag{3.32}$$

with $\tau, \beta\ and\ \Gamma$ denoting adjustable parameters. It should be noted that this model has only been validated up to 100°C, and might constitute a cause for error for higher temperatures.

[82] added Γ in order to account for the increased solubility of SO_2, and can be set to zero for our situation. The values used for the determination of ΔB are taken from [82] and are shown in Table A.1.
In order to calculate the activity coefficient γ_i for the different gas components, an approach similar to [26] is used. the change in activity coefficient due to solute interactions is based on a virial expansion of Gibbs excess energy as given by Equation 3.33:

$$\ln(\gamma_i) = \sum_C 2m_c\lambda_{i-C} + \sum_A 2m_A\lambda_{i-A} + \sum_C\sum_A m_A m_C \zeta_{i-A-C}, \tag{3.33}$$

where m_c and m_a respectively denote anion and cation molality, and λ_{i-C} and ζ_{i-A-C} are second and third-order interaction parameters, the values of which are given in Table A.2 and Table A.3. λ_{i-A} is assumed to be 0. Temperature and pressure dependency of the interaction parameters is accounted for using Equation 3.34:

$$\text{Par}(T,P) = c_1 + c_2T + \frac{c_3}{T} + c_4P + \frac{c_5}{P} + c_6\frac{P}{T} + c_7\frac{T}{P^2} + \frac{c_8P}{630-T} + c_9T\ln P + c_{10}\frac{P}{T^2}. \tag{3.34}$$

3.3.2 Aqueous component phase partitioning

For the H$_2$O component in the system a similar procedure is used to define phase partitioning. However, Henry's law is not applicable to the computation of the fugacity of the H$_2$O component in the aqueous phase, because it assumes a very low concentration for the computed component. An alternative method for the equilibrium constant for water is given by [70]:

$$K_{H_2O} = \frac{f_{H_2O_{(g)}}}{a_{H_2O(l)}}. \tag{3.35}$$

Inserting Equation 3.19 into Equation 3.35 gives rise to Equation 3.36:

$$f_{H_2O,NA} = p\phi_{H_2O}x_{H_2O,NA} = K_{H_2O}a_{H_2O,Aq}. \tag{3.36}$$

Because the solubility of gaseous components in the aqueous phase in the considered temperature range(30-130°C) is low, the activity a can be reasonably approximated by the amount of aqueous component in the aqueous phase($x_{H_2O,Aq}$). The equilibrium constant as a function of pressure and temperature is defined by Equation 3.37:

$$K_{H_2O}(p,T) = K^0_{H_2O}(p_0,T)\exp\left[\frac{(p-p_0)V_{H_2O}}{RT}\right], \tag{3.37}$$

where V_{H_2O} denotes the average partial volume of water in the aqueous phase within the pressure interval $(p-p_0)$, with p_0 the reference pressure taken to be 1 bar. $K^0_{H_2O}$ is defined with a straightforward relation from [70] given by Equation 3.38 where θ is the temperature T in °C:

$$\log\left(K^0_{H_2O}\right) = -2.209 + 3.097\times10^{-2}\theta - 1.098\times10^{-4}\theta^2 + 2.048\times10^{-7}\theta^3. \tag{3.38}$$

Combining Equation 3.36 and Equation 3.37, and rewriting to separate the phase mass fractions, we get Equation 3.39 for the equilibrium constant K_{H_2O}:

$$K_{H_2O} = \frac{x_{H_2O,NAq}}{x_{H_2O,Aq}} = \frac{K^0_{H_2O}(p_0,T)\exp\left[\frac{(p-p_0)V_{H_2O}}{RT}\right]}{p\phi_{H_2O}}. \tag{3.39}$$

3.3.3 Flash

With the computed K values, it becomes possible to calculate the phase partitioning of the components between the Aq-NAq phases with the use the Rachford Rice equation given in Equation 3.40:

$$\sum_{i=1}^{N_c} \frac{z_i\left(K_i-1\right)}{1+\beta\left(K_i-1\right)}=0, \tag{3.40}$$

where z_i denotes the mole fraction of the individual components in the entire system. β is initially estimated, and then iteratively computed. This gives the following solution for the component phase partitioning:

$$x_{i,Aq}=\frac{z_i}{1+\beta\left(K_i-1\right)}, \quad x_{i,NA}=\frac{K_i z_i}{1+\beta\left(K_i-1\right)}. \tag{3.41}$$

3.4 Physical Properties

In order to correctly show the behaviour of our system in the reservoir, physical properties of the fluid resulting from the computed phase partitioning need to be characterized. The used correlations are shown in section 3.4 for an overview.

Property	Correlation	Name	Citation	Pressure (bar)	Temperature (K)	Salinity (M)
x, y, V	EOS	ZiabakhshGanji	[82]	1-600	278-403	0-6
k_r	Relperm	Brooks-Corey	[18]	N/a	N/a	N/a
ρ_{NAqP}	ρ_{NAqP}	PR	[59]	N/a	N/a	N/a
μ_{NAqP}	μ_{NAqP}	Carr	[20]	N/a	N/a	N/a
	μ_{CO_2}	Heidaryan CO2	[35]	75-1014	310-900	N/a
	μ_{CH_4}	Heidaryan CH4	[34]	30-1014	300-400	N/a
H_{NAqP}	H_{NAqP}	Guo	[32]	1-1000	273-573	N/a
λ_{NAqP}	λ_{NAqP}	Amooey	[10]	1-300+	290-800	N/a
ρ_{AqP}	ρ_{brine}	Spivey	[69]	1-2000	278-548	0-4.3
	$\rho_{brine+CO_2}$	Garcia	[30]	N/a	278-573	0-4.3
μ_{AqP}	μ_{brine}	Batzle and Wang	[13]	1-500	278-523	0-4+
	$\mu_{brine+CO_2}$	Islam and Carlson	[39]	1-600	293-378	N/a
H_{AqP}	H_{AqP}	Guo	[32]	1-1000	273-573	0-6
	Δh_{salt}	Michalides	[52]	N/a	373-573	N/a
	P_{sat}	Antoine	[64]	N/a	273-643	N/a
λ_{AqP}	λ_{AqP}	Sharqawy	[66]	N/a	273.15-363	0-2.5

Table 3.2: Correlations used in the model with their validity ranges

3.4.1 Flow properties

Relative permeability

In multiphase systems, differences in wettability and interfacial tension inhibit flow through pore throats. This means that depending on the saturation the effective permeability will be less than the absolute permeability of the rock. The equation to compute effective permeability of phase i is given by Equation 3.42:

$$k_{e,i}=k * k_{r,i}, \tag{3.42}$$

where k is the rock absolute permeability and $k_{r,i}$ is the relative permeability of phase i. The equation used in this model for the computation of the phase relative permeability is the commonly used Brooks-Corey equation [18], given in Equation 3.43 as:

$$
\begin{aligned}
k_{\mathrm{r,w}} &= k_w^0 \left(\frac{S_{\mathrm{w}} - S_{\mathrm{w,c}}}{1 - S_{\mathrm{w,c}} - S_{\mathrm{g,r}}} \right)^{n_{\mathrm{w}}}, \\
k_{\mathrm{r,g}} &= k_g^0 \left(\frac{S_g - S_{\mathrm{g,r}}}{1 - S_{\mathrm{w,c}} - S_{\mathrm{g,r}}} \right)^{n_{\mathrm{g}}},
\end{aligned}
\tag{3.43}
$$

where $k_{r,i}$ are phase relative permeabilities between 0 and 1, k_i^0 are phase endpoint permeabilities denoting the relative permeability at maximum phase saturation, $S_{w,c}$ and $S_{g,r}$ are the irreducable saturations for the water and gas phases at and below which the phase is not mobile and n^w, n^g are phase exponents which govern the shape of the relative permeability curves, the values of which are dependant on the capillary behaviour of the system. The result are curves for every phase correlating phase saturation with relative permeability, an example of which are the relative permeability curves used in this study in Figure 3.3.

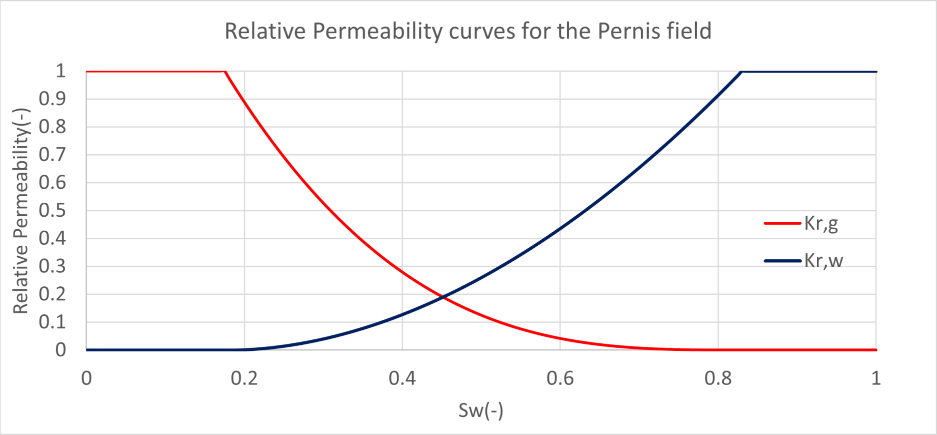

Figure 3.3: Relative permeability curves using Brooks-Corey for the Pernis field

3.4.2 Non-aqueous phase properties

The NAq phase consists predominantly of CO_2 and CH_4 with trace amounts of H_2O. Under reservoir conditions this mixture is often supercritical, meaning that it does not follow ideal gas property behaviour. However, due to it's lack of interfacial tension, this phase can be approximated as a gas with extra correlations required to predict phase properties.

Density of non-aqueous phase

The density of the non-aqueos phase can be readily calculated with the molar volume obtained from the Peng-Robinson EOS (PR-EOS) [59]. The PR-EOS provides a good fit of the vapour pressure for most substances, but the prediction of molar volume and, hence, density, is rather poor. However, Hekayati [36] demonstrated that this deviation is mainly present for pressures and temperatures near the critical point, which is not the case in most of our models where reduced pressure far larger than 1.

$$
\rho = \frac{M_w}{V_{M_g}}, \quad V_{M_g} = \frac{Z * R * T}{p}, \tag{3.44}
$$

where V_{M_g} is the molar volume of the phase, Z is retrieved from Equation 3.26 and M_w is the phase molar mass given by:

$$
M_w = \sum_{i=nc} Mw_i * y_i. \tag{3.45}
$$

Viscosity of the non-aqueous phase

The non-aqueous phase in this model consists of CO_2 and CH_4 with trace water. In this model, the effect of water vapour on NAqP viscosity is assumed negligible due to it's low mole fraction and disregarded. When discussing viscosity we mean the dynamic viscosity which is used in Darcy's law. In order to compute the phase viscosity, the correlation from [20] will be used. It is important to note that this equation is an averaging method, and does not take into account any molecular interaction between the components:

$$\mu_g = \frac{\sum_i \mu_{g,i} \cdot y_i \cdot \sqrt{M_{w,i}}}{\sum_i y_i \cdot \sqrt{M_{w,i}}}, \tag{3.46}$$

where $\mu_{g,i}$, y_i and $M_{w,i}$ are the pure component viscosity, NAqP phase mole fraction and pure component molecular weight of component i respectively. The pure component equivalent viscosities are computed with correlations from [34] and [35] and are discussed in the next paragraphs.

Pure CO_2 viscosity There are multiple existing correlations for computing the viscosity of supercritical CO_2. The equation used in this research from Heidaryan [35] is used for its simplicity in implementation, as well as its accuracy in predicting between 75 and 1014 bar and 310 to 900 Kelvin. The equation is independent of pressure, meaning inaccuracies in density predictions do not propagate to the viscosity prediction. It should be noted that the proposed equation is a fitted polynomial, and as such this model should not be extended outside the validated range:

$$\mu = \frac{A_1 + A_2 p + A_3 p^2 + A_4 \ln(T) + A_5(\ln(T))^2 + A_6(\ln(T))^3}{1 + A_7 p + A_8 \ln(T) + A_9(\ln(T))^2}. \tag{3.47}$$

Here p is the pressure in bar, T is the pressure in Kelvin, and the resulting μ is expressed in Centipoise (Cp). A_{1-9} denote fitting parameters which are specified in Table A.5.

Pure CH_4 viscosity Similarly to CO_2, a correlation from Heidaryan [34] is used to predict the viscosity of CH_4 due to its simplicity in implementation. as well as its accuracy in predicting between 30 and 1014 bar and 300 to 400 Kelvin. The equation is independent of pressure, meaning inaccuracies in density predictions do not propagate to the viscosity prediction. It should be noted that the proposed equation is a fitted polynomial, and as such this model should not be extended outside the validated range.

$$\mu = \frac{A_1 + A_2 p_\mathrm{r} + A_3 p_\mathrm{r}^2 + A_4 p_\mathrm{r}^3 + A_5 T_\mathrm{r} + A_6 T_\mathrm{r}^2}{1 + A_7 p_\mathrm{r} + A_8 T_\mathrm{r} + A_9 T_\mathrm{r}^2 + A_{10} T_\mathrm{r}^3}, \tag{3.48}$$

where p_r is the reduced calculated with the reservoir pressure p and CH_4 critical pressure in bar $p_r = \frac{p}{p_c}$, T_r is the reduced temperature obtained with $T_r = \frac{T}{T_c}$ in Kelvin, and the resulting μ is expressed in Centipoise (Cp). A_{1-10} denote fitting parameters specified in Table A.6.

Enthalpy of the non-aqueous phase

Perhaps the most important property to model for our simulator is the enthalpy of the non-aqueous phase, which governs the relative energy of the phase as it interacts with the model. The enthalpy model for this research is based on a method of Guo [32], with additional consideration for the enthalpy of water vaporization.

$$H_\text{gas} = H_\text{ideal} + \left(H_\text{gas} - H_\text{ideal}\right) = \sum_k x_k H_{k,\text{ ideal}} + \Delta H_\text{deviation} + \Delta H_{vap,H_2O}, \tag{3.49}$$

where X_k and $H_{k,ideal}$ denote the NAqP mole fraction and ideal component enthalpy of component k. $\Delta H_{vap,H_2O}$ is the change in enthalpy caused by the vaporization of water into the non-aqueous phase, conveniently described with $\Delta H_{vap,H_2O} = 40.8 * x_{H_2O}$ in $\frac{kJ}{mol}$ where $40.8\frac{kJ}{mol}$ is the enthalpy of vaporization for water. In this work the enthalpy of mixing is disregarded, as it's magnitude is far smaller than that of the other considered sources of enthalpy change[24]. The ideal component enthalpy is described by Equation 3.50 [9]:

$$H_{k,\text{ ideal}} = RT^* \left[\sum_{i=0}^{6} \frac{a_{i,k}}{i+1} \tau^{i+1} + a_7 \ln \tau + \sum_{8}^{12} \frac{a_{i,k}}{7-i} \left(\frac{1}{\tau}\right)^{i-7} \right] + H_{int,k}, \tag{3.50}$$

where R is the ideal gas constant, τ is the relative temperature given by $\tau = \frac{T}{1000K}$ and the other variables are described in Table A.7. The reference state for the enthalpy function given by $H_{int}$is atmospheric pressure and 25°C.For gas mixtures representative coefficients can be obtained by taking the molar fraction average values as shown in

$$a_{\text{k, mix}} = \sum_{k=1}^{N} x_k a_{i,k}, \quad H_{\text{int ,mix}} = \sum_{k=1}^{N} x_k H_{\text{int },k}. \tag{3.51}$$

The enthalpy deviation of a real gas system is described by the Peng-Robinson Equation of State with Equation 3.52. This value is computed during the EOS operation Equation 3.26, where $\frac{da}{dT}$ is computed with a simple numerical forward difference scheme

$$\Delta H_{\text{deviation}} = H_{\text{gas}} - H_{\text{ideal}} = RT(Z-1) + \frac{T\frac{da}{dT} - a}{2\sqrt{2}b} \ln \left(\frac{Z + (1+\sqrt{2})B}{Z + (1-\sqrt{2})B} \right). \tag{3.52}$$

Thermal conductivity of the non-aqueous phase

While not very significant for the overall magnitude of thermal conductivity, phase thermal conductivity can play a role over longer times or in highly porous reservoirs. In order to get reasonable values for the thermal conductivity of the non-aqueous phase an equation from Amooey [10] is used. In this model, the thermal conductivity of the phase is based completely on that of CO_2, which is an assumption that can be made due to the small impact of this property, as well as the fact that thermal gradients will mostly occur in areas with CO_2 transport occurring, as the injected fluid which induces the gradient is assumed to be (nearly) pure CO_2. The equation is given by Equation 3.53:

$$\lambda(mW/(mK)) = \frac{A_1 + A_2\rho + A_3\rho^2 + A_4\rho^3T^3 + A_5\rho^4 + A_6T + A_7T^2}{\sqrt{T}}, \tag{3.53}$$

where ρ is the phase density and T is temperature in Kelvin, which is valid for densities from 1-1200 kg/m^3 and temperatures from 290-800K. $A1-7$ are tuned coefficients given by Table 3.4:

Coefficient	Tuned coefficient
A_1	-105.161×10^0
A_2	0.9007×10^0
A_3	0.0007×10^0
A_4	3.50×10^{-15}
A_5	3.76×10^{-10}
A_6	0.7500×10^0
A_7	0.0017×10^0

Table 3.4: Tuned coefficients from [10] used in Equation 3.53

3.4.3 Aqueous phase properties

The aqueous phase consists of water, NaCl, dissolved CO_2 and trace amounts of dissolved CH_4. Proper modelling of the aqueous phase is important to give insight into multi phase interactions, as well as proper thermal behaviour between the two phases, Two important assumptions are made to simplify the model. In the computation of properties, the effect of CH_4 on AqP properties is neglected due to it's very limited presence in the phase. Secondly, salt concentration does not vary throughout the phase, meaning that no concentration or dilution occurs when water evaporates or enters the system. This also means that the effects of salt precipitation on permeability shown by [24] are not taken into account.

Density of aqueous phase

The density of the aqueous phase is calculated in two steps; firstly brine density is computed, and secondly a correction is applied for the presence of dissolved CO_2,

Brine density

An empirical correlation developed by Spivey and McCain Jr. based on the IAPWS-95 international standard equation of state is used for the computation of brine density. The correlation is valid for a temperature range of 273 to 548K, pressure range from 0.1-200 MPa and salinity levels from 0-25 wt% NaCl [69]. The formulation of brine solution density is shown here in Equation 3.54:

$$\rho_b\left(p,T,C_m\right) = \rho_{b0}\left(T,C_m\right)\exp\left[I_b\left(p,T,C_m\right) - I_b\left(p,T,C_m\right)\right], \tag{3.54}$$

where $\rho_{b,0}$ is the brine solution density in $\frac{g}{cm^3}$ (this is converted to $\frac{kg}{m^3}$ for Equation 3.61) taken at reference pressure $p_0 = 70$MPa, and I_b is an empirically derived parameter. The brine density at reference pressure ρ_{b0} is defined as:

$$\rho_{b0} = \rho_{w0} + D_{Cm,2}(T)C_m^2 + D_{Cm,3/2}(T)C_m^{3/2} + D_{Cm,3}(T)C_m + D_{Cm,1/2}(T)C_m^{1/2}, \tag{3.55}$$

where $D_{Cm,1-5}$ are empirical parameters dependent on temperature using Equation 3.56 with the coefficients in Table A.8. This computation is done by replacing a with the variable to be computed, which is used for multiple parameters in the correlation. C_m is the NaCl molality in moles/kg.

$$a(T) = \frac{a_1\left(\frac{T}{100}\right)^2 + a_2\left(\frac{T}{100}\right) + a_3}{a_4\left(\frac{T}{100}\right)^2 + a_5\left(\frac{T}{100}\right) + 1}. \tag{3.56}$$

The density of pure water at reference pressure $\rho_{w,0}$ is computed with Equation 3.57:

$$\rho_{w,0}(T) = \frac{D_{w1}\left(\frac{T}{100}\right)^2 + D_{w2}\left(\frac{T}{100}\right) + D_{w3}}{D_{w4}\left(\frac{T}{100}\right)^2 + D_{w5}\left(\frac{T}{100}\right) + 1}. \tag{3.57}$$

where $D_{w,1-5}$ are empirical parameters from Table A.9, and T is the temperature in degrees Celcius. I_b from Equation 3.54 is derived with Equation 3.58:

$$I_b\left(p,T,C_m\right) = \int_p c_b dp = \frac{1}{E_b\left(T,C_m\right)}\ln\left|E_b\left(T,C_m\right)\left(\frac{p}{p0}\right) + F_b\left(T,C_m\right)\right|, \tag{3.58}$$

where E_b and F_b are empirical temperature and salinity dependent parameters calculated with Equation 3.59:

$$\begin{aligned} E_b(T, Cm) &= E_w(T) + E_{Cm}(T) * Cm, \\ F_b(T, Cm) &= F_w(T) + F_{C_m,2/3}(T) C_m^{2/3} + F_{C_m,1}(T) C_m + F_{C_m,1/2}(T) C_m^{1/2}, \end{aligned} \tag{3.59}$$

where $E_{Cm,i}$, $F_{C_m,i}$, E_w and F_W are computed with Equation 3.56 and coefficients from Table A.9 and Table A.10. Brine compressibility c_b is obtained from Equation 3.60:

$$c_b\left(p, T, C_m\right) = \left(\frac{1}{p_0}\right) \frac{1}{E_b\left(T, C_m\right)\left(\frac{p}{p_0}\right) + F_b\left(T, C_m\right)}. \tag{3.60}$$

Dissolved CO$_2$ correction

Subsequently, a correction needs to be made for the effect of dissolved CO$_2$ on density. for this the correlation from Garcia [30] is used, which gives aqueous phase density with:

$$\frac{1}{\rho_{aq}} = \frac{x_{Co_2} V_{\phi,CO_2}}{M_T} + \frac{M_{H_2O} x_{H_2O}}{\rho_b M_T}, \tag{3.61}$$

where ρ_b is the brine density computed by Equation 3.54 and M_{H_2O} and M_T are the molecular weights of water and the brine. The apparent molar volume of dissolved CO$_2$ in $(\frac{m^3}{mol})$ V_ϕ was found by [30] to be independent of pressure under 300°C, and is calculated with:

$$V_\phi = 37.51 - 9.585e - 2 * T + 8.740e - 4 * T^2 - 5.044e - 7 * T^3, \tag{3.62}$$

where T is temperature in degrees Celcius.

Viscosity of aqueous phase

Similarily to the density, the aqueous phase viscosity calculation is split up into two parts; the computation of brine viscosity and a correction for dissolved CO$_2$. For the computation of brine viscosity, a correlation from Batzle and Wang [13] is used for it's simplicity, and it's validity over a very large range; up to 500 bar pressure and 523K temperature. When discussing viscosity we mean the dynamic viscosity which is used in Darcy's law. The validity range is not mentioned explicitly, but the paper shows results for curves up to 240,000 ppm or more than 4 molal, which would be safe to assume as an upper bound. The equation is given by Equation 3.63:

$$\eta = 0.1 + 0.333S + \left(1.65 + 91.9S^3\right) e^{-\left[0.42\left(S^{0.8} - 0.17\right)^2 + 0.045\right] T^{0.8}}, \tag{3.63}$$

where S is the NaCl weight fraction in $(\frac{ppm}{10^6})$ and T is the temperature in degrees Celsius. After the brine viscosity is computed, a simple correlation from Islam and Carlson corrects for the effect of dissolved CO$_2$ on the phase viscosity. The correlation is valid for 1-600 bar and from 293 up to 378K [39]. However, The authors mention that the effect of CO$_2$ on viscosity strongly diminishes with temperature, with the effect at 373K being only a 0.6%. This means that while extra care should be taken in validation to see if further extension to e.g. 400K is possible, it's probably possible to extend the correlation to higher temperatures. The correlation is as follows:

$$\mu_{\text{brine}+\mathrm{CO}_2} = \mu_{\text{brine}}\left(1 + 4.65 x_{\mathrm{CO}_2}^{1.0134}\right). \tag{3.64}$$

Enthalpy of aqueous phase

The enthalpy of the aqueous phase is based on the correlation of [32] and is valid for temperatures between 0 and 300 °C, from solution saturation pressure to 1000 bar and from 0-6 mol/kg NaCl. The equation for pressure-independent brine enthalpy at saturation pressure is given by:

$$H_{\text{brine}}^{\text{saturation}} = x_1 H_{\text{water}} + x_2 H_{\text{salt}} + \Delta H_{\text{salt -dissolved}}\,, \tag{3.65}$$

where $H_{water,salt}$ are pure component enthalpies in kJ/kg at reference temperature 0 degrees celcius and $\Delta H_{\text{salt -dissolved}}$ is the deviation from the ideal enthalpy by mixing, computed with Equation 3.67. The ideal component enthalpies are computed with:

$$\begin{aligned} H_{\text{water}} &= 0.12453 \times 10^{-4} T^3 - 0.45137 \times 10^{-2} T^2 + 4.81155T - 29.578 \\ H_{\text{salt}} &= \left[-0.83624 \times 10^{-3} T^3 + 0.16792 T^2 - 25.9293T\right] \tfrac{4.184}{58.44}, \end{aligned} \tag{3.66}$$

where T is in degrees Celcius. Next the enthalpy of salt dissolution is computed used the Michaelides [52] correlation given by Equation 3.67:

$$\Delta H_{salt-dissolved} = \frac{4.184}{1000 + 58.44 C_m} \sum_{i=0}^{3} \sum_{j=0}^{2} a_{ij} T^i C_m^j, \tag{3.67}$$

where $x_1 = 1000/(1000{+}58.44{*}C_m), x_2 = 58.44{*}C_m/(1000{+}58.44{*}C_m)$ with C_m salt molality in mol/kg, T is temperature in $^\circ C$, and the values for a_{ij} are listed in Table A.11. The resulting enthalpy is in kJ/kg. Next, a pressure correction given in Equation 3.68is applied to account for the deviation from the saturation pressure using a correlation from Spivey, McCain and North [32]:

$$H_{\text{brine-revised}} = H_{\text{brine}}^{\text{saturation}} + \int \left[V - T \left(\frac{\partial V}{\partial T} \right)_P \right] dP, \tag{3.68}$$

which can be simplified due to the low compressibility of the aqueous phase, resulting in Equation 3.69:

$$H_{\text{brine-revised}} \cong H_{\text{brine}}^{\text{saturation}} + \left(V - T \left(\frac{\partial V}{\partial T} \right)_P \right) \cdot (P - P_{\text{saturation}}\,)\,. \tag{3.69}$$

This equation can be solved by taking $V = 1/\rho_a q$ and applying a simple forward difference scheme on Equation 3.54. The saturation pressure P_{sat} is computed using the Antoine equation by Roizard [64]:

$$\mathrm{P} = 10^{(\mathrm{A-B/(T+C)})}, \tag{3.70}$$

where T is in $^\circ C$ and P is in mmHg and needs to be converted. For $T < 100^\circ C$, $[A,\ B,\ C] =$ $[8.07131,\ 1730.63,\ 233.426]$. For $100^\circ C < T < 370^\circ C$, $[A,\ B,\ C] = [8.140191,\ 1810.94,\ 244.485]$. The average is used on $T = 100^\circ C$ to smooth the function. In order to account for the enthalpy of dissolution of gas into the aqueous phase, Guo proposes the use of the following equations:

$$\frac{\partial ln H_{\text{coeff}}}{\partial (1/T)} = \frac{\Delta H_{\text{gas – dissohed}}}{R}, \tag{3.71}$$

where R is the ideal gas constant, and H_{Coeff} is the Henry's Law coefficient computed with Equation 3.72:

$$H_{\text{coeff}} = K_h \gamma. \tag{3.72}$$

Here K_h is Henry's constant, and γ is the activity coefficient, both of which are already computed during the phase partitioning procedure of the Fugacity-Activity model in the previous section. This equation accounts for the effect of salinity on the enthalpy of solvation of gasses [32]. The methodology used for computing these variables is different from [32], which reduces the valid range of the model to the range of the PR-EOS. The equation is solved with a forward difference scheme on Equation 3.31 and Equation 3.33. It is important to note here that only the effect of CO_2 dissolution is considered.

Thermal conductivity of the aqueous phase

Similar to the non-aqueous phase, the thermal conductivity of the aqueous phase could play a significant role in aquifer interaction in high porosities. In this model, a modified version of an equation from Sharqawy [66] for thermal conductivity of salt water is used. This equation holds for a a wide range of salinities, but does not correct for the effect of pressure differences, the modification of is fitted based on reference data and given in Equation 3.73. As the thermal conductivity of a control volume is dominated by that of rock due to it's larger volume fraction, the main goal of this property is to give a reasonable value for thermal conductivity in porous water-filled formations. The thermal conductivity of the aqueous phase is given by Equation 3.73:

$$\lambda_{aq}(W/(mK)) = \frac{\lambda_{pure}}{0.00022S + 1}, \tag{3.73}$$

where S is salinity in g/kg, P is pressure in bar and λ_{pure} is fresh water thermal conductivity given by Equation 3.74:

$$\lambda_{pure} = 0.797015 \times T^{*-0.194} - 0.251242 \times T^{*-4.717} + 0.096437 \times T^{*-6.385} - 0.032696 \times T^{*-2.134}, \tag{3.74}$$

W=where T^* is dimensionless temperature given by $T^* = T(K)/300$.

Chapter 4

Simulation Strategies

In this chapter, The strategies and procedures used for using the model and generating results will be described. Firstly, some general simulation procedures regarding the model, initalization and data processing will be discussed. Following this, The set-up for the different experiments performed will be discussed. The experiments are as follows:

1. 2D Macroscale Heterogeneity Study, testing the effect of variation within-formation layering, net-to-gross and reservoir architecture on CPG performance
2. 2D Sensitivity Study, testing sensitivity of CPG to reservoir properties arising from microscale heterogeneity, as well as some other variables of interest
3. 3D Study, testing the effect of porosity and facies distributions on a 3D high-resolution ensemble of box models.

4.1 Simulation Strategies for Model

Manual corrections to model values

Equation 3.47 from [35] is the equation used to predict the viscosity of CO_2 in the supercritical region. However, because the correlation is empirical, it is not possible to use the equation outside of the validated range of pressure and temperature. In the case for this correlation, the viscosity actually can become negative at sub-critical pressures. In order to prevent any model problems at low pressure conditions, the viscosity of CO_2 is set constant at 0.018 Cp at pressures below 72 bar. In order to ensure a smooth transition, the average of 0.018 and the result from Equation 3.47 is used between 72 and 77 bar. The result of this modification is illustrated in Figure B.4 in chapter 5. Additionally, the used for thermal conductivity of brine does not take into account the effect of pressure [66]. In order to account for this, an additional pressure term $(+5 * 10^{-5} * P)$ is added to Equation 3.74 by fitting the model output to experimental data from [46]. The resulting pressure dependency can be seen in Figure B.14, showing sufficiently accurate modelling of brine thermal conductivity over our range of interest.

Saturation initalization

One challenge with initializing the reservoir is the proper initalization of phase saturation. The DARTS model used works with a molar based notation, whereas the resulting molar initialization needs to amount to the required saturation. For example, wrongly initializing connate water saturation could allow for water production where there should be none. Thus, an algorithm is required to convert desired saturation to molar composition. Gas Saturation in the model is calculated by:

$$S_g = \frac{\rho_{m,aq}}{\frac{\rho_{m,naq}}{V} - \rho_{m,naq} + \rho_{m,aq}}, \tag{4.1}$$

with $\rho_{m,i}$ being the molar density of phase i and V the vapor fraction of the control volume. The required molar densities and vapor fraction are all results from the fugacity-activity model, flash and properties calculations. As such, they are fundamentally dependant on the four state variables $P,\ Z_{CO_2},\ Z_{CH_4},\ T$, as well as the in this model invariant salt molality C_m. This means the problem is ill-defined, as there are five variables for a single known variable (the desired S_g). However, when initializing the reservoir, we assume constant $P,\ T,\ C_m$ throughout the reservoir. In order to reduce the problem further, we can use the fact that there are two clear initial states we are interested in:

1. Before CO_2 development, only trace (e.g. $Z_{CO_2} = 1e-3$), is present.
2. After EGR and repressurization and at the onset of the CPG stage, predominantly CO_2 with trace CH_4 (e.g. $Z_{CH_4} = 10^{-2}$) is present.

Thus, an assumption is made that one of the gaseous components has constant composition for a certain saturation value. This reduces the problem to a single unknown, allowing us to solve for composition. As an example; assuming for a control volume in the gas cap a before-development reservoir initalization could be $S_{g,req} = 1 - S_{w,c}, Z_{locked} = Z_{CO_2} = 10^{-3}$. An inital guess is made:

$$S_{g,i} = f(P_{res}, Z_{locked}, Z_{not\ locked,i}, T_{res}), Z_{H_2O,i} = \frac{1 - Z_{locked}}{2}, \tag{4.2}$$

where $Z_{not\ locked,i} = \frac{1-Z_{locked}}{2}$. We make use of the fact that in our system, we know that CH_4 and CO_2 favour the non-aqueous phase, whereas H_2O favours the aqueous phase. Thus, we use the following algorithm for converging to the correct saturation:

$$Z_{not\ locked,i+1} = \begin{cases} Z_{not\ locked,\ i} + \delta, & \text{if } S_{g,i} < S_{g,req}, \\ Z_{not\ locked,\ i} - \delta & \text{if } S_{g,i} > S_{g,req}, \\ Z_{not\ locked,\ final} & \text{if } S_{g,i} \approx S_{g,req}, \end{cases} \tag{4.3}$$

where δ is a converging parameter. In this model $\delta = \frac{abs(S_{g,i} - S_{g,req})}{10}$, gave the best results for convergence. Initialization was chosen to be converged for $\delta \leqslant 10^{-5}$.

Energy production data plotting

In order to acquire useful insights from plotting thermal production information, some extra steps need to be taken. There are three types of data that need to be produced; produced temperature, cumulative energy extraction and energy extraction rate. produced temperature is simply retrieved from the engine, or with a simple rate-weighted averaging method if two sets of perforations are used as is the case in the 2D experiments. For the energy extraction rate, a method similar to [74] is used for the showing the correct energy values. In this conversion, we assume that injection is 100% CO_2, and for production we also assume 100% CO_2 in the gas phase during the CPG stage, as the energy from water and methane is not necessarily extracted by the direct cycle turbine. This assumption can be made as CPG only starts when the produced gas phase contains a very high fraction (>97%) CO_2.
The molar heat extraction rate of CO2 is given by:

$$Q_{CO2} = (E_{CO2,out} - E_{CO2,in}) * q_{CO2,out}, \tag{4.4}$$

where Q_{CO2} is the heat extraction rate, either in Kj/day or kW, $q_{CO2,out}$ is the molar CO_2 production rate in Kmol/day, and $E_{CO2,in,out}$ are the molar enthalpies in kj/kmol at bottomhole injector and producer respectively. The bottomhole molar injection energy is relative, and is defined as:

$$E_{in} = H_{in} - H_{surface}. \tag{4.5}$$

Where H_{in} is the enthalpy of pure CO_2 at bottomhole conditions, and $H_{surface}$ is the reference enthalpy at standard surface conditions, here chosen to be gas phase at 298.15 K and 1.01325 bar. Conveniently, the integration constants of the enthalpy functions is chosen such that H = 0 for surface conditions.

Over- and underburden

In order to ensure the reservoir boundary does not affect the thermal behaviour of the reservoir, all models are 'insulated' between a large overburden consisting of impermeable rock, and a large underburden which can either consist of impermeable rock or permeable aquifer to simulate an infinitely extending aquifer depending on the run. To allow for a sufficiently accurate thermal gradient on the boundaries while limiting the number of required cells, over- and underburden cells are modelled to grow exponentially in thickness away from the formation as shown in Figure 4.1.

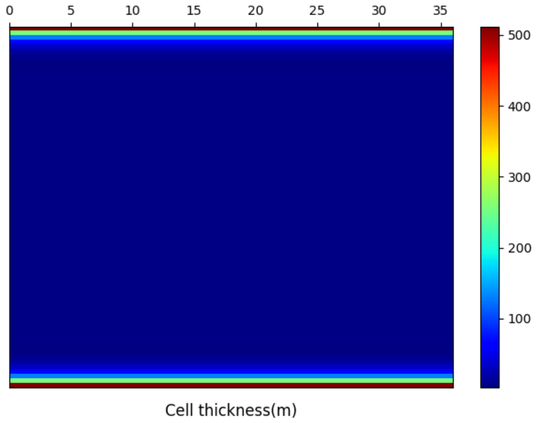

Figure 4.1: Model cell thickness growing exponentially in over- and underburden

4.2 Experiment Setup for Macroscale Heterogeneity

This experiment sets out to test the effect of formation net-to-gross ratio (N/G) and the specific architecture of this net-to-gross to CPG performance on a simplified synthetic 2D reservoir model. As discussed in the literature study, classical measures of heterogeneity such as the Dykstra-Parson coefficient don't translate well to geothermal problems as they do not take into account the conductive flux originating from the distribution of impermeable rock within the formation. To this end, it is useful to study both the effect of net-to-gross, as well as the distribution of net and gross rock within a formation. The following experiment is set-up:

1. Create a pseudorandom realization of layer cake models with a certain sum N/G, creating sets of different N/G (from 0.2 to 0.8)
2. Measure the amount of contact surface for each realization
3. Run large amount (5000) realizations, ordering their outcomes into sets of N/G. OBL supporting points can be reused as the dynamic model stays the same.

4. Analyze factors such as N/G, lifetime, energy production and importance of conduction.

4.2.1 Synthetic reservoir ensemble for layering study

Reservoir description

The synthetic reservoirs are loosely based on the Pernis reservoir model. Important to note is the BHP control. At the time of running this experiment, mass or volumetric rate control did not yet work sufficiently well. This means that for changing N/G ratios, the flow rate through the reservoir will vary. This is accounted for in the analysis of the results. The model used one injector and one producer placed at the edges of the 2D reservoir model, and the starting time of simulation is at the start of the CPG stage, meaning trace CH_4 with predominantly CO_2 in the NAqP. Both over- and underburden are impermeable rock. The reservoir configuration is shown in Table 4.2.

Table 4.2: Reservoir specifics for the 2D Macroscale ensemble generation

Formation	**Unit**	**Value**	**Control**	**Unit**	**Value**
Formation dx	m	360	Well control	-	BHP
Formation dy	m	180	Bottom-hole pressure	bar	±50
Formation dz	m	300	Boundaries	-	no flow
dx	m	5	Overburden thickness	m	
dy	m	100	Injection temperature	K	308
dz	m	10	Injection ZCO2	-	1
Temperature	K	383			
Pressure	bar	250			
Salinity	mol/kg	1.368			
Sandstone	**Unit**	**Value**	**Shale**	**Unit**	**Value**
phi	-	0.175	phi	-	0.01
k	mD	6	k	mD	1.00E-12
Heat Capacity	kJ/m^3	1930	Heat Capacity	kJ/m^3	2470
Thermal Conductivity	W/mK	259.2	Thermal Conductivity	W/mK	190.1
$\frac{kv}{kh}$	-	0.8	$\frac{kv}{kh}$	-	0.8
$S_{w,c}$	-	0.175	$S_{w,c}$	-	0.175
$S_{g,i}$	-	0.825	$S_{g,i}$	-	0.05

Ensemble generation

In order to generate an ensemble of models with randomized layer architecture and varying N/G a procedure based on integer partitioning is used. Firstly, the total reservoir thickness is split up into layers according to the vertical cell thickness. Then, the layers are split up according to the specified N/G ratio. Integer partitions (all the ways an integer can be split up into smaller integers) of the resulting numbers are computed, and the resulting vectors are joined and shuffled. An example of the generation of a pseudo-random layer distribution is shown in Figure 4.3.

The amount of possible integer partitions grows incredibly fast with increasing integer. For the model in this report, splitting up 30 in N/G ratios of 0.2 to 0.8, and combining and shuffling the integer partitionings resulted in $1.7 * 10^5$ different configurations. In order to reduce modelling time, 5000 models were randomly sampled. The N/G distribution of the sampled models is shown in Figure 4.4.

It can be seen from the figure that the models with a more even net-to-gross were favoured in sampling. This is caused by the method of generation. For every N/G, the total number

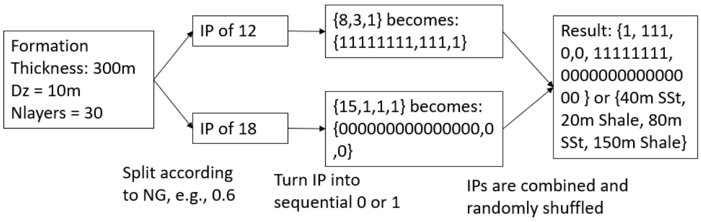
Formation
Thickness: 300m
Dz = 10m
Nlayers = 30
IP of 12
IP of 18
{8,3,1} becomes:
{11111111,111,1}
{15,1,1,1} becomes:
{000000000000000,0
,0}
Result: {1, 111,
0,0, 11111111,
0000000000000
00 } or {40m SSt,
20m Shale, 80m
SSt, 150m Shale}
Split according
to NG, e.g., 0.6
Turn IP into
sequential 0 or 1
IPs are combined and
randomly shuffled

Figure 4.3: Schematic example of layering generation framework

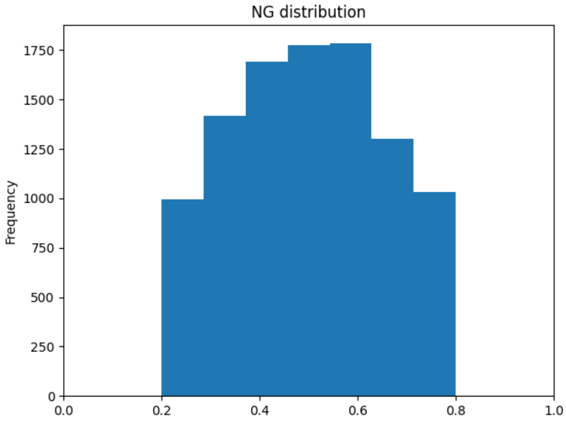

Figure 4.4: N/G distribution of the sampled reservoir realizations

of combinations is the product of the two integer partition vectors. $IP(15) \times IP(15)$ results in a larger number amount of combinations than $IP(6) \times IP(24)$, and as such the number of reservoir realizations there is larger. There are still enough models at the extremities in order to get decent insights at this specific configuration, but it should be noted that this discrepancy might increase when the total number of layers increases. That means care should be taken when copying this procedure to see if the resulting distribution is good enough. A few examples of the resulting reservoir configurations with varying N/G and distributions are shown in Figure 4.5.

4.2.2 Experiment analysis

At the macroscale, the N/G of a reservoir can influence the total amount of heat extracted and the lifetime of the reservoir quite strongly. [25] showed the effect of N/G on the lifetime on low-enthalpy brine based geothermal systems. A first order measurement of heterogeneity effect can be measured in a similar fashion by relating lifetime to N/G. The next order is to explore the effect of N/G difference on lifetime. As an analogue one could think of a radiator. Conduction and convection, the surface area vs. volume ratio determines the efficiency at which energy transport can take place. In a layer cake model, this is quite easy to write down quantitatively:

Assume a reservoir with total nondimensionalized volume of 1. then:

$$V_{reservoir} = \frac{N}{G} * 1 = \frac{N}{G}. \tag{4.6}$$

A single productive layer will have two sides connected to over- and underburden, two layers will have 4 etc. for a layer-cake reservoir model of top-down area $A = w * l$, the contact area with unproductive layers is:

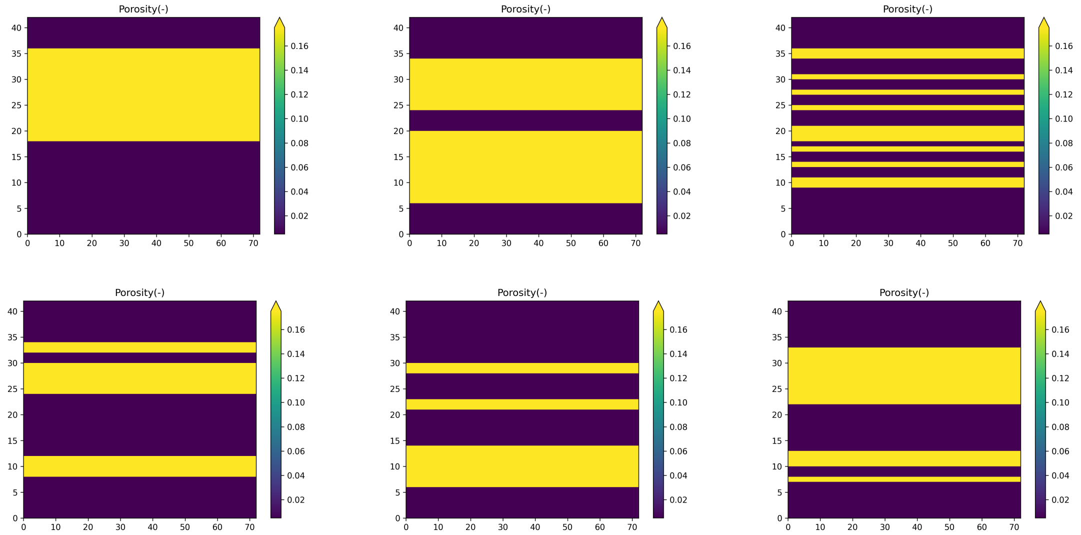

Figure 4.5: Array of some possible reservoir realizations

$$A_{contact} = 2 * N_{producing} * A. \tag{4.7}$$

By combining N/G and $N_{producing}$, We can get an idea of the effect of N/G segmentation on reservoir performance. This can be measured in reservoir lifetime.

Thermal Péclet number

A second measure, as used in [77], in to use the thermal Péclet number. The thermal Péclet number quantifies the relative strength of advection and conduction during heat transport. Because impermeable parts of the reservoir do not allow flow, but do allow conduction, this number can give insight into the relative importance of recharging over time. The thermal Péclet number is defined mathematically as Equation 4.8:

$$\mathrm{Pe} = \frac{Advective\ thermal\ transport\ rate}{Conductive\ thermal\ transport\ rate} = \frac{\sum_{p=1}^{n_p} \int_t h_p \rho_p Q_p dt}{\sum_{i=1}^{n_c} \int_t \int_{\Omega_{ci}} \mathrm{div}(\kappa \nabla T) d\Omega dt}, \tag{4.8}$$

where Q_p refers to phase flow rate (AqP, NAqP) at the production well. Ω_{ci} denotes the control volume of the i^{th} cell. This combination gives the fraction of produced heat brought about by thermal conduction.

4.3 Experimental Setup for Sensitivity Study

4.3.1 Synthetic reservoir for 2D sensitivity

A lot of microscale and mesoscale heterogeneities can be described by a change of a property in the bulk rock. For example, stylolites and laminations can be described by their effect of reducing vertical permeability, introducing permeability anisotropy. A good way to test this is by creating a 2D model based on the Pernis reservoir and subsequently changing a single parameter and testing it's impact on reservoir performance. Other uncertain parameters not related to microscale heterogeneity can also be tested this way. In order to improve readability of effects of single variable changes, the complexity of the reservoir needs to be toned down significantly. To this effect, the Pernis reservoir lithology is simplified to shale layers consisting of the Schieland Group, Lower Holland Marl and Mid Holland Claystone, and sandstone layers consisting of the Ijsselmonde Sandstone Member, De Lier Member and Holland Greensand. The resulting lithology and thicknesses for the 2D model are shown in Table 4.6. The Ijsselmonde sandstone member is considered to be filled with water, with the GWC on the border between the Ijsselmonde and De Lier Members. Instead of gaussian distributed values, constant values are used for the different properties.

Table 4.6: Lithology to 2D reservoir model conversion

Function	**Geological Unit**	**Abbrev.**	**Layer thickness**	**Type**
-	-	-	m	-
Underburden	Ijsselmonde SSt. Member	KNNSY	Boundary	Sst. Aquifer
Reservoir	De Lier Member	KNNSL	75	Sst. Gas Bearing
	Lower Holland Marl		50	Shale
	Holland Greensand	KNGLL	75	Sst. Gas Bearing
Overburden	Mid Holland Claystone		Boundary	Shale

Many values are required or initalizing the 2D model. for this model, the dimensions were chosen to resemble a doublet in a 1 km^2 five-spot pattern, as this configuration is chosen in other research on CPG [28] [29]. Reservoir pressure and temperature were increased to 250 bar and 110K in order to simulate a deeper reservoir location compared to the real Pernis field, which lies at only about 1300-1800 m depth. This change brings the model more in line with other CPG research and the target CCS reservoirs in the Netherlands. The Pernis field was chosen as a reference due to the availability of a real reservoir model. For this run, two separate producer-injector pairs are used for each of the productive layers in order to see the different behaviour in reservoirs with and without a GWC. The location of wells is shown in Table 4.3.1. The Holland Greensand member is perforated over the length of the formation, and the de Lier Member is perforated for the upper 30m section to limit upconing of the underlying aquifer brine.

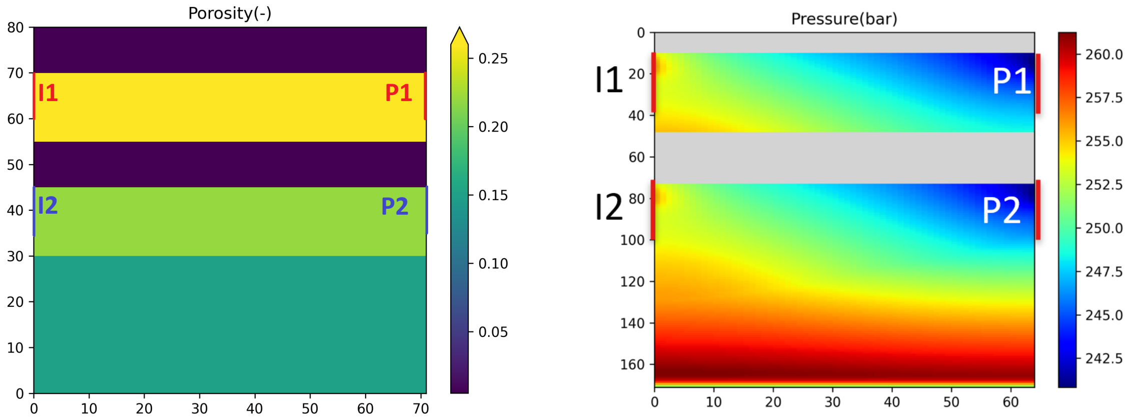

Figure 4.7: Well locations shown together with the different layers (left) and in a pressure profile plot during a run (right)

For the well control, volumetric rate control was used in order to have a more or less consistent production rate between different runs for better comparison. The control rates are based on bottomhole volume. It should be noted that due to the changing density of CO_2 under varying pressure and temperature, mass flow rate will not be completely consistent over time. Mass control rate was not supported by the simulator at the time of performing this research, and thus volumetric rate control was chosen as a second best for keeping consistent production figures. It should also be noted that the base case vertical permeability anisotropy was set from 0.8 in the real reservoir to 0.3 in order to keep the effect of coning in line. Upconing of brine will be further discussed in the results. Chosen values for the reservoir, the different formations and run control for the base case model are shown in Table 4.8.

Table 4.8: Properties for the base case reservoir model

Formation	**Unit**	**Value**	**Control**	**Unit**	**Value**
Formation dx	m	710	Well control	-	Volumetric rate
Formation dy	m	400	Gas injection rate	m3/day	2200
Formation dz	m	Varying	Inj. BHP constraint	bar	+125
dx	m	10	Gas production rate	m3/day	1700
dy	m	400	Prod. BHP constraint	bar	-150
dz	m	5	Boundaries	-	no flow
Temperature	K	383	Injection T	K	308
Pressure	bar	250	Injection ZCO2	-	1
Salinity	mol/kg	1.368			
Greenland Sst.	**Unit**	**Value**	**De Lier Sst.**	**Unit**	**Value**
Layer thickness	m	75	Layer thickness	m	75
ϕ	-	0.26	ϕ	-	0.22
K	mD	9.29	K	mD	17.6
Heat Capacity	kJ/m^3K	1930	Heat Capacity	kJ/m^3K	1930
Conductivity	kJ/(mdayK)	259.2	Conductivity	kJ/(mdayK)	259.2
$\frac{Kv}{Kh}$	-	0.3	$\frac{Kv}{Kh}$	-	0.3
$S_{w,c}$	-	0.175	$S_{w,c}$	-	0.175
$S_{g,i}$	-	0.825	$S_{g,i}$	-	0.825
Shale	**Unit**	**Value**	**Ijsselmonde Sst.**	**Unit**	**Value**
Layer thickness	m	Varying	Layer thickness	m	Varying
ϕ	-	0.01	ϕ	-	0.15
K	mD	1.00E-03	K	mD	4.47
Heat Capacity	$kJ/(m^3K)$	2470	Heat Capacity	kJ/m^3K	2470
Conductivity	kJ/(mdayK)	190.1	Conductivity	kJ/(mdayK)	190.1
$\frac{Kv}{Kh}$	-	0.3	$\frac{Kv}{Kh}$	-	0.3
$S_{w,c}$	-	0.175	$S_{w,c}$	-	0.175
$S_{g,i}$	-	0.05	$S_{g,i}$	-	0.05

2D Sensitivity study analysis

The different parameters of interest for the sensitivity study are divided into five different categories. The Initial State parameters concern the state parameters and salinity which govern the dynamic model. These experiments aim to explore how different initial states influence CPG performance. The next group called Reservoir parameters, concern reservoir structure and permeability variability. The aim of these tests is to explore how different permeability regimes and larger structures within the reservoir influence CPG performance. The relative permeability category consists of variables that govern the Brooks-Corey equation for relative permeability given in Equation 3.43. The Thermal category explores the effect of uncertainty in thermal rock properties that might arise from different minerologies. To conclude, the Control section includes a comparative test that aims to clarify some interesting behaviour that was found during testing regarding well configuration. An overview of the different tests and quantities is shown in Table 4.9.

4.4 Experimental Setup for 3D Simulation

In order to properly test the effect of porosity-permeability heterogeneity, it is better to test on 3D models. The reason for this is that flow paths can move in three dimensions, and thus might be able to go around flow baffles. Models were generated using a Petrel Pernis model from [16].

Table 4.9: Overview of different parameters tested in the 2D sensitivity study, * signifies base case variable

Category	**Variable**	**Description**	**Low**	**Mid**	**High**	**Unit**
Initial state	Pres	Reservoir Pressure	220	250	270	bar
	Tres	Reservoir Temperature	90	110*	130	C
	Cm	Brine Salinity	0	1.368*	3	mol/kg
Reservoir	Dlayer	Separating layer thickness	5	50*	100	m
	Kv/Kh	Permeability Anisotropy	0.3*	0.5	0.8	
	K	Permeability factor	1*	-	5*	-
Relperm	Ng	Brooks Corey gas exponent	1	3*	5	-
	Nw	Brooks Corey water exponent	1	1.9*	3	-
Thermal	Rcond	Thermal conductivity(factor)	0.5	1*	1.5	-
	Hcap	Heat Capacity(factor)	0.8	1*	1.2	-
Control	Rate	Overinjection	0	-	500*	m3/day

4.4.1 3D Box models

For this experiment, a Pernis model developed in Petrel was used to generate box models of the reservoir. The facies and resulting porosity distribution is made using sequential gaussian simulation constrained to well data. In order to test variations in both facies distributions and porosity distributions, 25 facies realizations were generated with 4 porosity realizations for each facies realizations for a total of 100 models. From this model a $1km^2$ box was extracted centered around the Eemshaven-1 (EEM-01) well. The location of the box model in the Pernis model is shown in Figure 4.10.

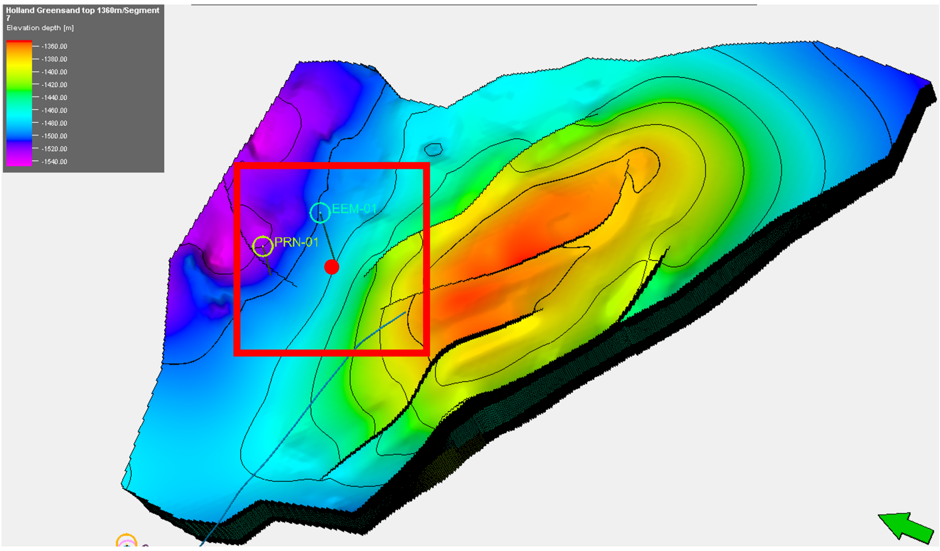

Figure 4.10: 3D Box model from the Pernis Petrel model [16]

Figure 4.11 shows the x and y directions of two reservoir realizations, centered on the EEM-01 well. Here we can see that while there are distinct differences in the location and size of shale patches as well as the distribution of porosity, the well constraint ensures that the realizations are not completely random.

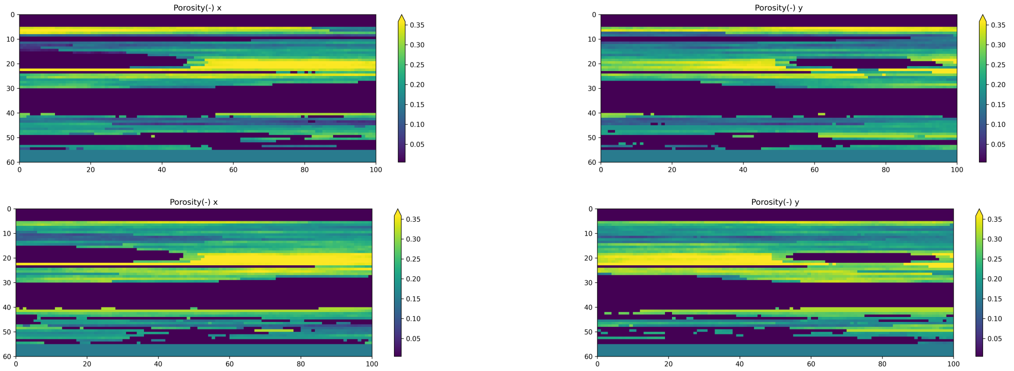

Figure 4.11: Crosssections of 3D Box realizations centered on the EEM-01 Well. Left to right, top to bottom: Realization 40 x and y direction, Realization 80 x and y direction

In order to eliminate the effect of reservoir boundaries, a 5-spot injection-production pattern with producer in the middle was chosen. Making the assumption that the 5-spot configuration continues around throughout the reservoir, the boundaries of the box model denote no-flow boundaries between two adjacent 5-spots. A schematic description of this 5-spot pattern is shown in Figure 4.12. Initialization procedure is similar to Table 4.8, with the only difference being that $\frac{K_v}{K_h} = 0.8$ in this test. Wells are perforated along the entire length of the productive formation. Specific rates for the tests are discussed in the results.

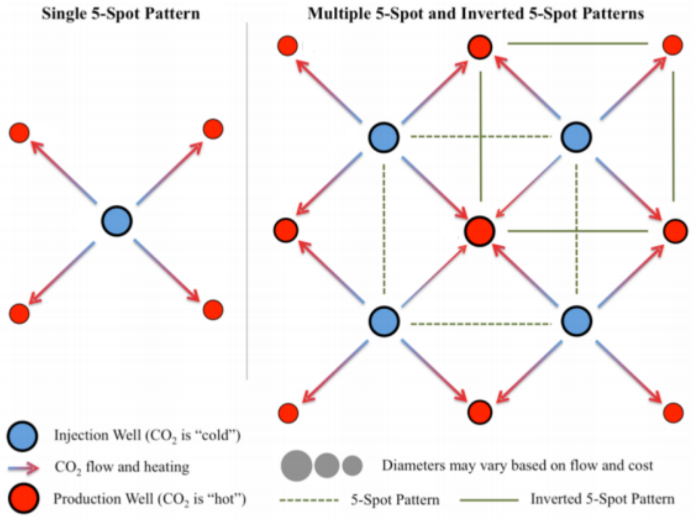
Single 5-Spot Pattern
Multiple 5-Spot and Inverted 5-Spot Patterns
Injection Well (CO$_2$ is "cold")
CO$_2$ flow and heating
Production Well (CO$_2$ is "hot")
Diameters may vary based on flow and cost
5-Spot Pattern
Inverted 5-Spot Pattern

Figure 4.12: Schematic description of 5-spot pattern, modified after [15]

Quantifying areal heterogeneity

In order to have a benchmark to compare the 3D heterogeneous systems to, every realization will be upscaled to homogeneous layers with representative average permeability and porosity. for quantifying heterogeneous systems, the geometric mean is the most accurate of the upscaling techniques [6] given by Equation 4.9:

$$\mathrm{k_{avg}} = \exp\left[\frac{\sum_{i=1}^{\mathrm{n}} \left(\mathrm{V_i} \ln\left(\mathrm{k_i}\right)\right)}{\sum_{\mathrm{i}=1}^{\mathrm{n}} \mathrm{V_i}}\right], \tag{4.9}$$

where $V_i,\ k_i$ respectively denote volume permeability of cell i It should be noted that the permeability correlations from Equation 2.2 concern the productive facies in the formations, and do not take into account the presence of impermeable shale patches, Thus, the geometric mean permeability is calculated from the with-layer net rock. In order to keep the resulting volume consistent. Porosity is calculated with the volumetric average over the gross formation.

Chapter 5

Simulation Results

In this chapter, the results from the various experiments performed are showcased and discussed. Firstly, the results from the 2D Macroscale heterogeneity experiments is showcased. Then, the various 2D Sensitivity experiments are discussed. Finally, the results from the 3D experiments are shown. The set-up for each experiment is discussed in detail in chapter 4.

5.1 Results from the Macroscale Experiments

In this section, the results from the 2D Macroscale heterogeneity will be shown and discussed. As there are 5000 models, this will mainly be done by means of analyzing metadata such as net-to-gross, lifetime cumulative energy production and Thermal Péclet number. First, energy production will be discussed. Then, some information on the recovery factor is shown. The recovery factor here is described as the cumulative energy produced as a fraction of the extractable energy in the formation at t=0. Finally, some figures showing the importance of conduction using the Thermal Péclet number are discussed. Figure 5.1 shows some of the temperature distributions at thermal breakthrough.

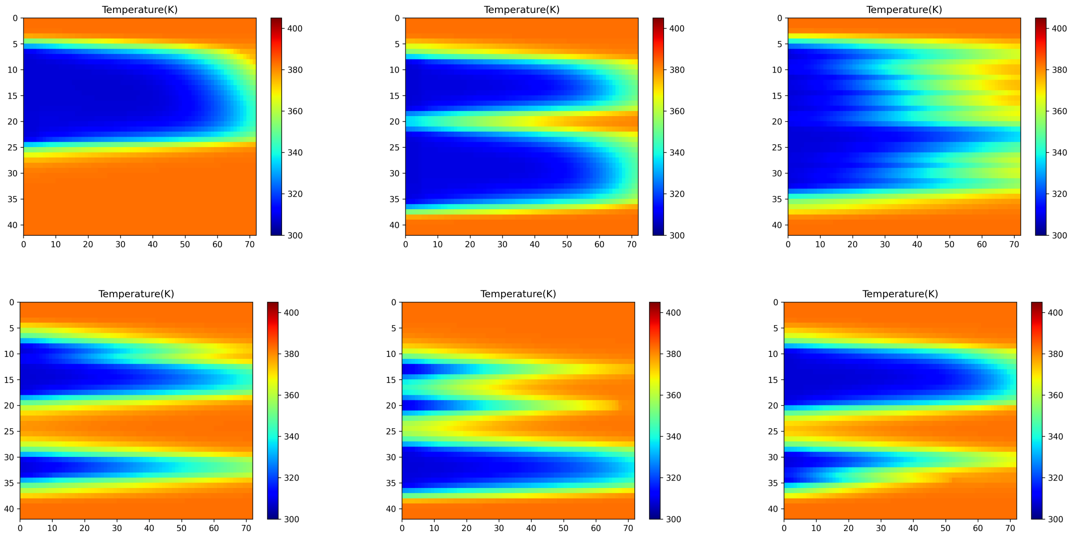

Figure 5.1: Array of the temperature distribution at thermal breakthrough for the realizations from Figure 4.5

5.1.1 Energy extraction

One issue we need to account for is the use of BHP control. This means that a N/G = 0.8 will have twice the production rate of a N/G = 0.4, simply due to fact that there is more net rock to conduct fluid. As such, we try to characterize the effect of layering by measuring the cumulative produced energy, but scaling for the amount of net productive rock in each realization. The resulting figure gives an insight into the energy produced for a certain height of a productive formation surrounded by a large amount (low N/G) of unproductive rock versus the same height of productive formation surrounded by more productive rock (high N/G). Figure 5.2 Shows histograms plotting cumulative produced energy normalized on N/G with data points grouped on Net-to-Gross and the amount of layers present in the reservoir. For the latter, the distinction was made between 'massive' formations consisting of two or less productive layers, 'mixed' formations consisting of 3 to 4 layers and 'layered' reservoirs consisting of more than 4 productive layers.

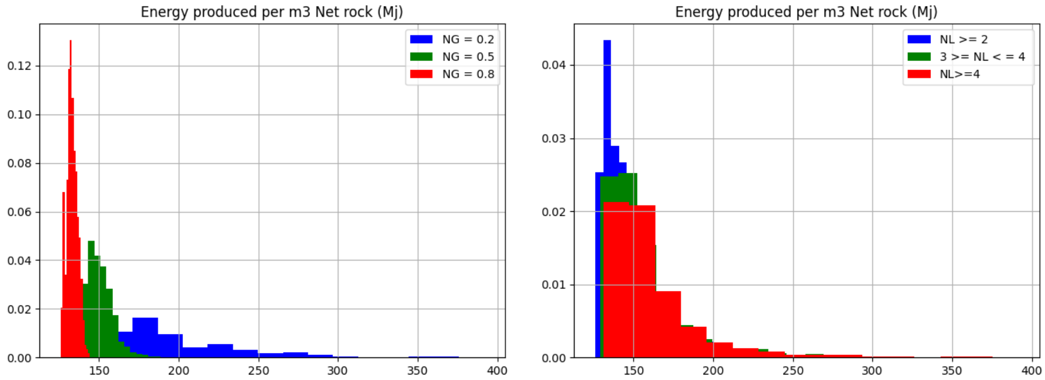

Figure 5.2: Histograms of energy produced per volume of net rock

From Figure 5.2 we can note a few observations. For one, the variance in energy density increases dramatically with reducing N/G. It also appears that the mean energy density increases with decreasing N/G. Looking at the figure comparing different degrees of layering, it is more difficult to observe any clear link between the two parameters. Looking at the scatter plot for the entire data set in Figure 5.3, we can see a very clear trend in the link between N/G and energy produced per net rock. With increasing net-to-gross, both the average energy density and spread in results reduces quite strongly. This might indicate that at high N/G ratios, layer architecture is not very important to thermal recharge. At low N/G, the spread in the effect of thermal recharge from unproductive layers increases dramatically, with the most segmented N/G = 0.2 realizations producing more than 2.5 times the amount of energy compared to high N/G realizations.

Looking at the scatter plot for layering, the results are more difficult to interpret. There appears to be a slight increase in the minimum energy density with increasing degree of layering, as well as a dramatic increase in spread. However, from 12 contacts onwards, the distribution appears to converge to a lower point again. This can be caused by two effects. Firstly, Figure 5.4 shows that highly layered reservoirs are highly underrepresented in the data set, meaning the trends we see for high contact numbers might not be generalizable. Secondly, Due to the maximum amount of layers of 30 over the entire reservoir, high amount of contact surfaces can only occur in realizations with a N/G closer to 0.5. For example a N/G=0.2 realization contains 60m of productive formation, with at a vertical resolution of 10m has a maximum amount of 12 contact surfaces. This is thus mostly an artifact of the statistical set-up of the experiment, and it is difficult to make any rigorous conclusion about the effect of layering on CPG performance.

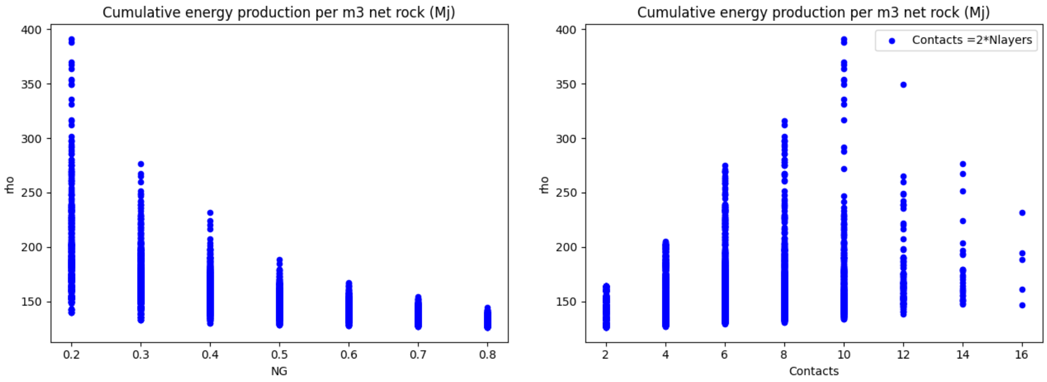

Figure 5.3: Scatter plots of energy produced per volume of net rock

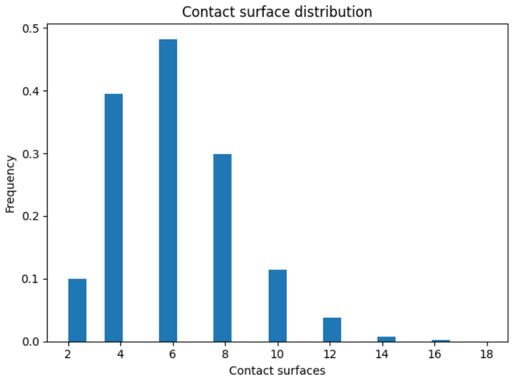

Figure 5.4: Histogram of contact surfaces over entire dataset

Another way of characterizing thermal performance is by scaling the cumulative energy production to the amount of injected CO_2, which would compare realizations based on the 'effort' required to produce the energy. Figure 5.5 shows a less clear trend towards either layering or N/G, apart from lower N/G exhibiting a wider variance in results. This would make sense, seeing as there is a maximum amount of energy CO_2 can extract per pass, and any additional energy from thermal recharge would be translated in a longer lifetime.

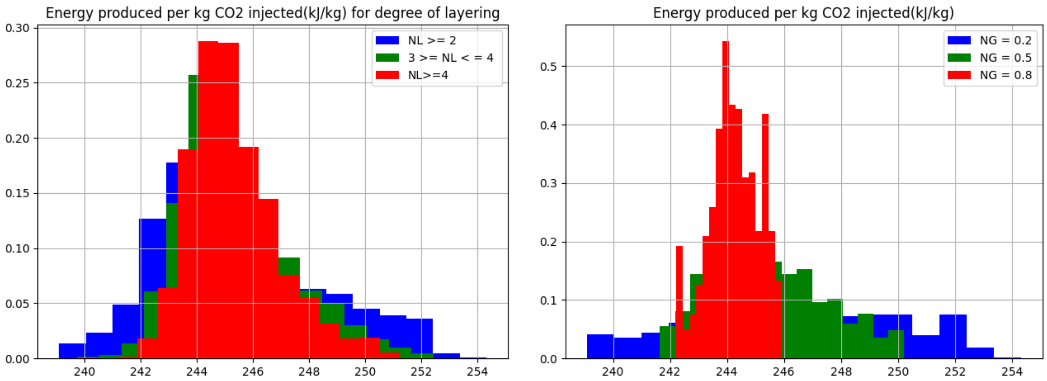

Figure 5.5: Base case plots of reservoir thermal properties

5.1.2 Recovery factor

Secondly, an analysis was made on the basis of the thermal recovery factor. This recovery factor is defined as the cumulative produced energy divided by the total extractable rock energy present in the (gross) formation at t=0 Figure 5.6 Shows inconclusive results for the degree of layering, but shows a clear increase of RF with increasing N/G. This is in agreement with [3], who showed CPG performs better as productive reservoir thickness increases. It does however seem that the RF does not increase proportionally to the N/G. A factor 4 increase of N/G from 0.2 to 0.8 shows a roughly factor 3 increase in RF from 0.1 to 0.3. Also, the low N/G realizations are fat-tailed, meaning the probability is skewed towards higher RF compared to a normal distribution.

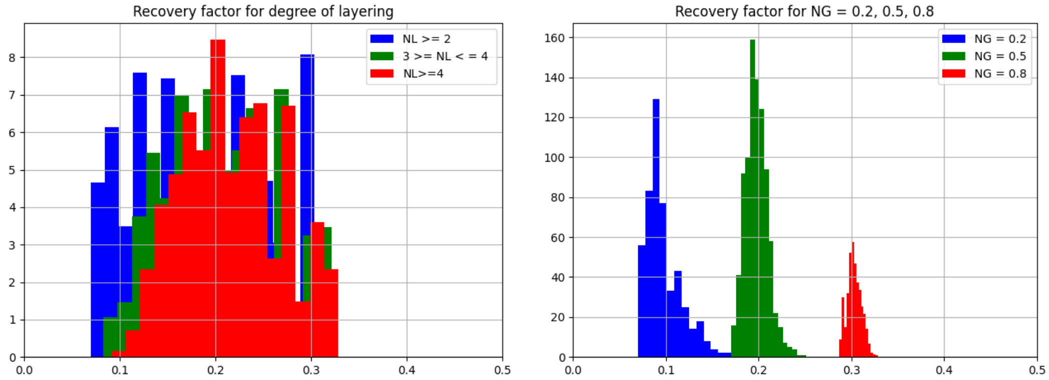

Figure 5.6: Histograms of Recovery Factors

Looking at the recovery factor scatter plots in Figure 5.7, we observe that this fat-tailed distribution at low N/G is caused by the degree of layering, with high N/G realizations showing little variation based on degree of layering. We also note that again, higher N/G is associated with a higher RF, but not in a 1-to-1 ratio.

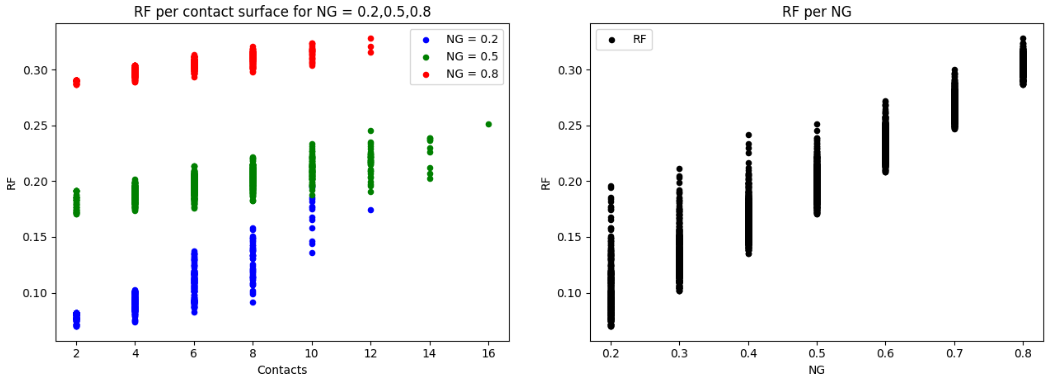

Figure 5.7: Scatter plots of Recovery Factor

5.1.3 Importance of conductive flux

Finally, we analyze the importance of conductive flux using the Thermal Pe outlined by Equation 4.8. Figure 5.8 shows the progression of all realizations over time plotted as a function of the Thermal Pe. The first thing to observe is that the Thermal Pe varies between roughly 2.5 and 4.7 on a log 10 scale, which indicates that convective flux is dominant in every single realization. There is however a difference in order of magnitude of importance when comparing massive vs layered reservoirs following the aforementioned definition. We observe that layered reservoirs show a lower spread in Thermal Pe progression, as well as longer lifetime caused by this increased conduction. For the N/G case, we observe clear differences again in both the order of magnitude of the Thermal Pe, and also in the resulting lifetime. Here the distinction is a lot clearer. We can thus infer that conduction is never enough to maintain a steady state (which would be a Thermal Pe of 1). We also also see that N/G is a better indicator that layering architecture for importance of conductive flux.

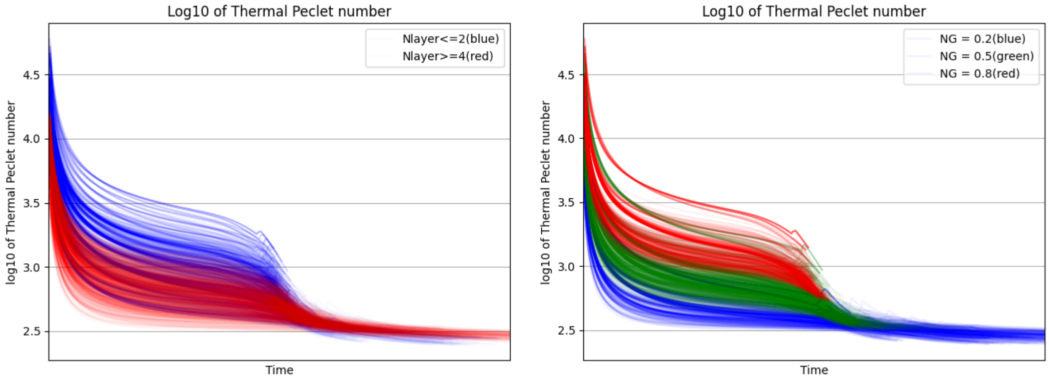

Figure 5.8: Base case plots of reservoir thermal properties

5.2 Results of Sensitivity Study

5.2.1 Base case

In this section, the results from the Base Case will be discussed in detail in order to provide a clear reference for the other sensitivity studies. Figure 5.9 shows the phase densities and viscosities after 15 years of CPG. It should be noted that the y and x axis of the graphs denote cell count, not distance. Reservoir dimensions are given in Table 4.8. From this graph, we can clearly infer the the effect of the thermal front on phase properties. For example, the cold non-aqueous phase has a significantly higher density and viscosity compared to the hot non-aqueous phase. This difference is less pronounced for the aqueous phase, indicating that phase interactions throughout the reservoir will change as the cold front progresses.

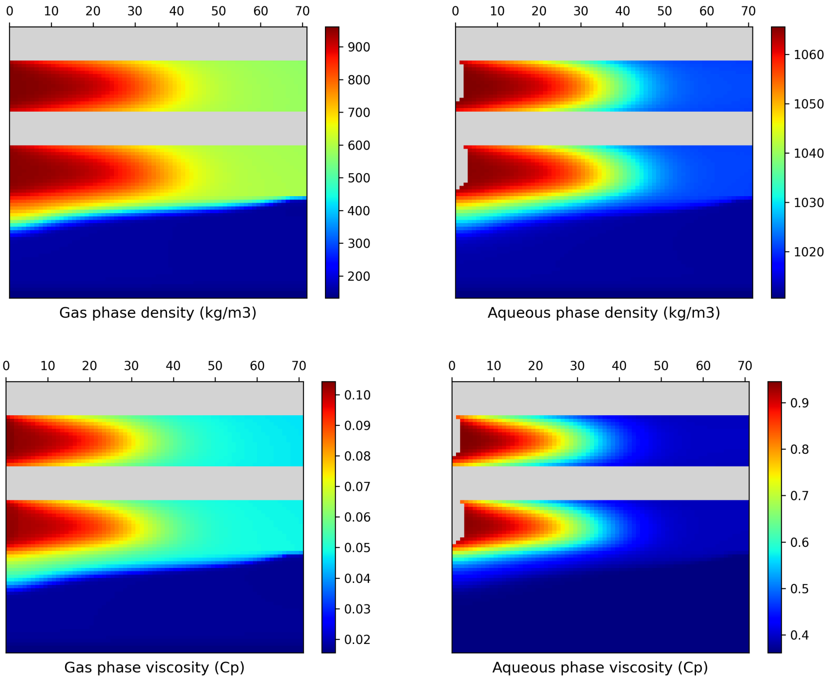

Figure 5.9: Base case plots of phase densities and viscosities after 15 years of CPG

Figure 5.10 Shows the distribution of temperature in the reservoir after 15 and 60 years of CPG. here, we can see that the CO_2 in the 'de Lier' formation goes down into the aquifer, increasing the contact area with hot reservoir rock. We also observe the temperature in the separating layer being close to equilibrium with the productive formations, meaning most of the heat has conducted out.

Figure 5.11 shows the gas saturation distribution after 15 and 60 years of CPG. The first thing to note is the reservoir dry out near the injection well. This reservoir dry-out could result in salt precipitation and the formation of skin, which is not taken into account in this model and could reduce injectivity [24]. Also, we can observe the strong aquifer displacement which necessitated reducing vertical permeability. looking at Figure 5.9, it can be seen that cold, dense supercritical CO_2 has a density approaching that of the aqueous phase, meaning displacment occurs easily. Also note the effect of brine upconing after 60 years of production. Again, the density of cold CO_2 reduces the critical coning velocity of the aquifer, in turn allowing for upconing to occur toward the end of the lifetime of the CPG stage.

Figure 5.12 shows mass production rates, energy extraction rates, cumulative energy extracted and production temperature for the base case model. We can observe a sharp drop in temperature as the cold front nears the production wells. temperature and energy extraction

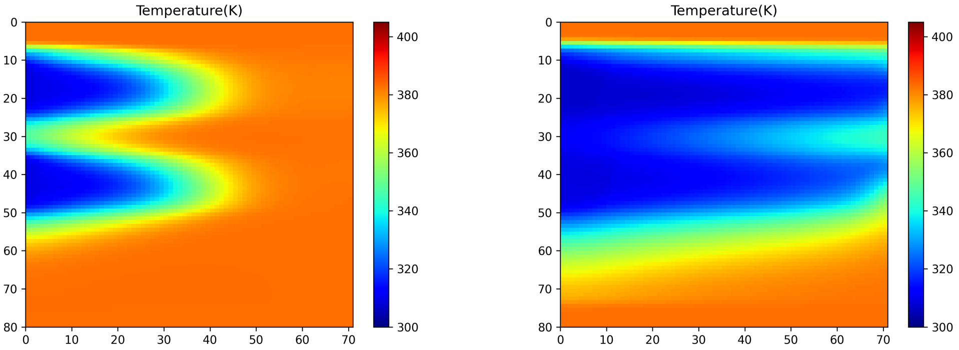

Figure 5.10: Base case thermal profile after 15 and 60 years of CPG

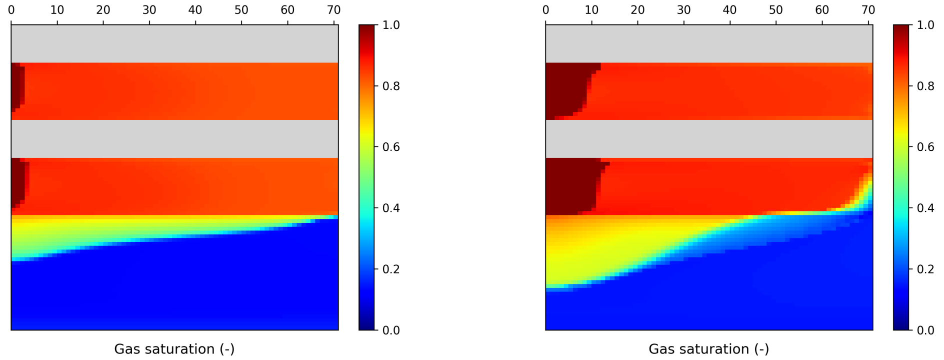

Figure 5.11: Base case saturation profile after 15 and 60 years of CPG

rate graphs both show a spike around 53 years, which indicates the BHP constraint is met and the production well can not sustain the required volumetric rate at the density of CO_2 at that temperature. The production rate for CO_2 shows some complex behaviour which is difficult to analyze in detail without looking at the individual production wells. It is however important to note that even though there exists brine upconing there is little produced water. More insightful is analyzing the production wells individually, which allows investigating the effect of aquifer presence. Figure 5.13 Shows the above mentioned graphs, split up into P1 in the 'Holland Greensand' formation and P2 in the 'de Lier' formation. It can be observed that total energy extracted is very similar. Production temperature profiles look similar until diverging after 40 years around 335K. This is caused by P1 showcasing a strong drop in pressure, leading to the reaching of the 100 bar well constraint after 53 years. As CO_2 shows strong expansivity, a sharp drop in pressure is associated with a drop in temperature due to expansive cooling, leading to a link between BHP and production temperature as shown here and in Figure 5.14.

Looking at the split-production rates in Figure 5.13, We can see that in the first 5-10 years of production, overinjection in both layers causes a steady rise in BHP as seen in Figure 5.14. This in turn increases density, causing a steady slight increase in mass production rate at constant volumetric rate. At P2, this overinjection even causes pressure to rise above the 250 bar initial state, leading to a slight increase in production pressure around year 20. However, after 25-30 years, the cold front with reduced mobility has progressed enough to induce a drop in producer BHP. In P2, we can observe some form of drive caused by the aquifer, which in reality is the rebounding of the depression in the aquifer caused by the injection pressure as

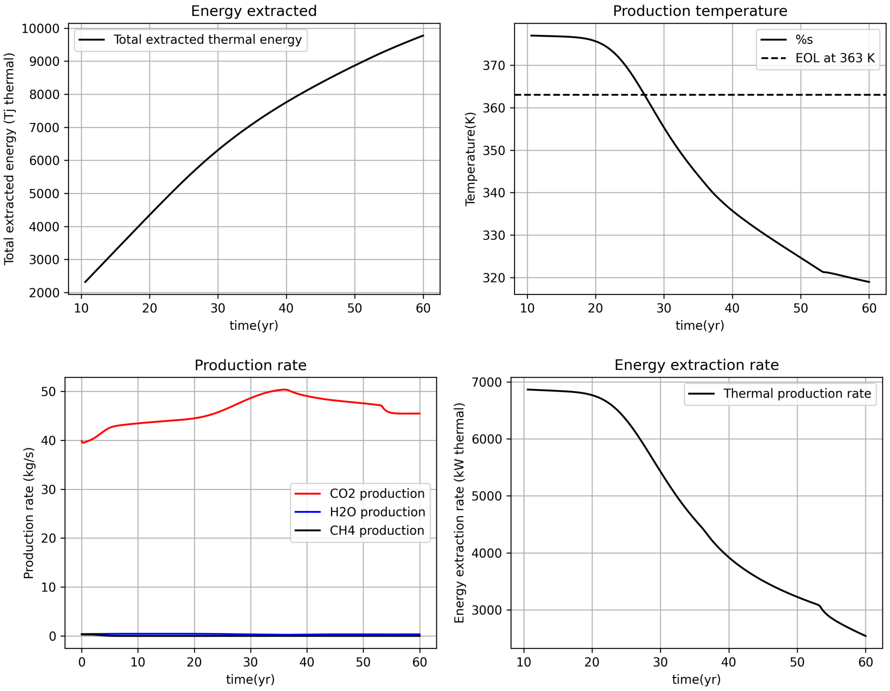

Figure 5.12: Base case production data

seen in Figure 5.11. In this figure, one can even observe the line from which water is starting to imbibe into the non-aqueous phase below the original aquifer line. This rebounding effect is not present for P1, which in turn shows a steep decline in BHP until the constraint is hit as shown in Figure 5.14. This indicates that the specified volumetric flow rate can not be sustained in this reservoir at low temperatures.

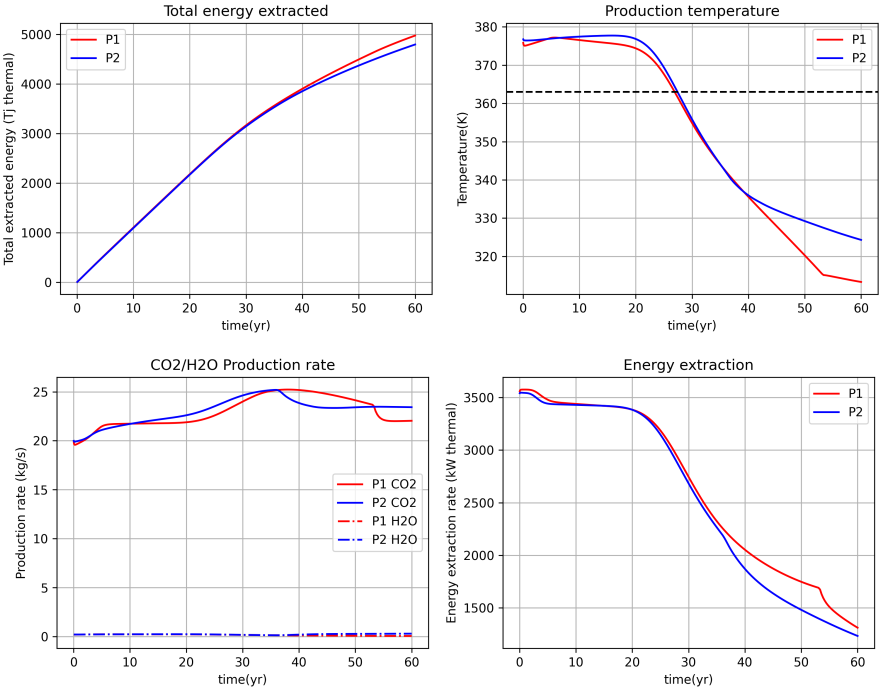

Figure 5.13: Base case production data per production well

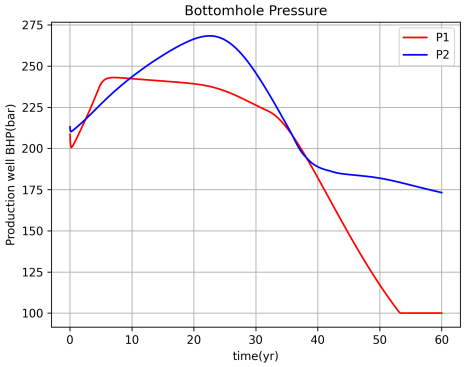

Figure 5.14: Comparison between the two reservoir segments, 1 is upper and 2 is lower

5.2.2 Initial state parameters

Reservoir pressure

In this sensitivity study, initial reservoir pressure was varied from 220 to 270 bar. It was not possible to go wider, as the very large well constraints at +125 and -150 bar would put BHP outside of the validated pressure range. Complete reservoir production graphs are shown in Figure C.1. Figure 5.15 shows the well production data. We can observe that initial reservoir pressure does not significantly impact cumulative energy production or production temperature until after year 40, when temperatures diverge due to diverging BHP values as shown in Figure C.2. The mass production rate does show some erraticity, mainly in the form of a drop in mass flow rate between years 30 to 40 for P2.

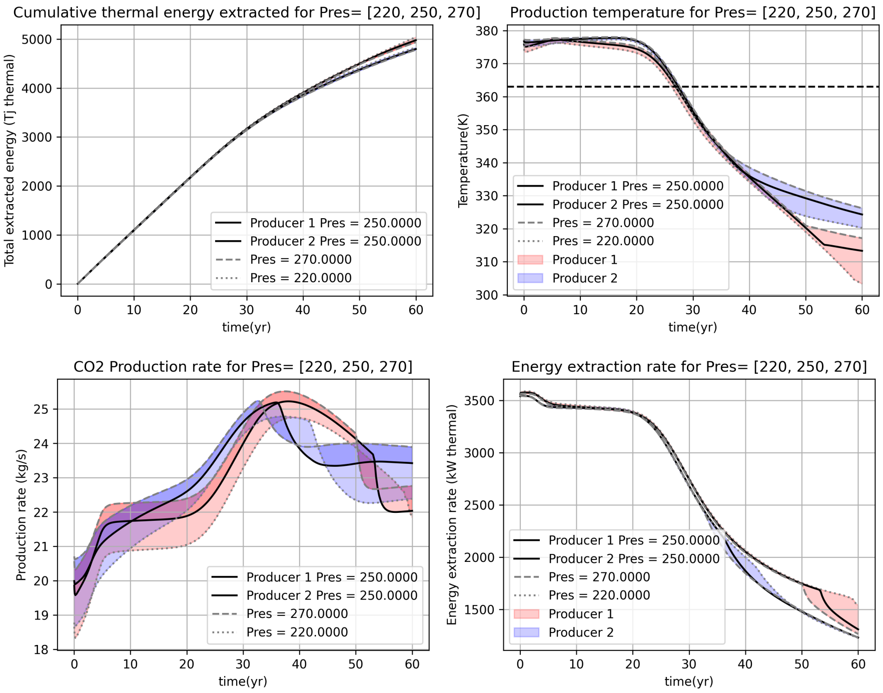

Figure 5.15: Production graphs for reservoir pressure sensitivity test per well

Looking at the saturation profiles in Figure 5.16, we can see that this is probably caused by different mobility contrasts between the aqueous and non-aqueous phases. From this, it can be inferred that as the operating pressure of a reservoir or in the region of a producer reduces, coning issues reduce as well.

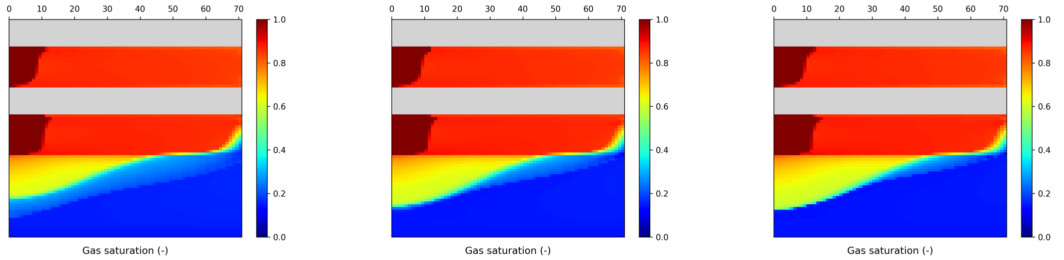

Figure 5.16: Reservoir pressure sensitivity saturation profile after 60 years of CPG. From left to right: low case, base case, high case

Reservoir temperature

In this sensitivity study, initial reservoir temperature was varied from 90 to 130 $^{\circ}C$. Complete reservoir production graphs are shown in Figure 5.17. Figure C.3 shows the well production data. For this dataset, P1 at low temperature hit the well constraint in year 40 as shown in Figure 5.19, making the mass production rate graph for well difficult to read. From this, we can infer that higher temperatures not only increase the amount of extractable energy, but also require lower BHP to produce. This limits expansive cooling and further enhances CPG performance. Thus, in this section the reservoir wide production graphs are discussed. In the figure below it can be seen that apart from the expected variation in production temperature and energy extracted, production profiles look rather similar.

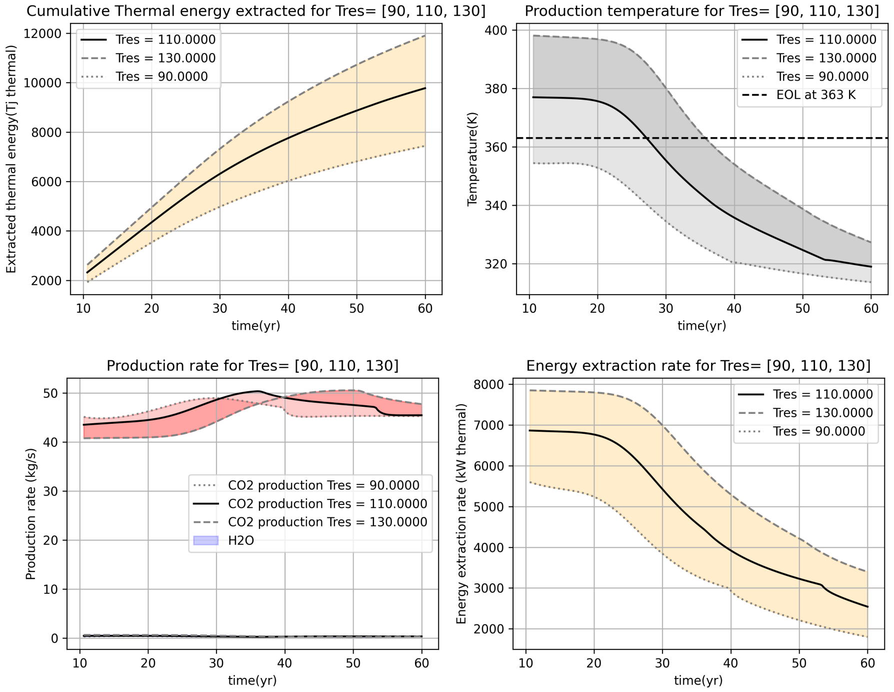

Figure 5.17: Production graphs for reservoir temperature sensitivity test

The main differences are seen in the severity of brine upconing. Figure 5.18 shows the different saturation profiles after 60 years of CPG. The arrival of the aqueous phase upconing at the production well is associated with a drop in mass flow rate, as reduced relative permeability in the blocks adjacent to the well necessitate a drop in BHP to keep volume constant, which is associated with reduced density due to expansion. Thus, we can infer that apart from energy considerations, increasing temperature is associated with reduced aqueous phase upconing.

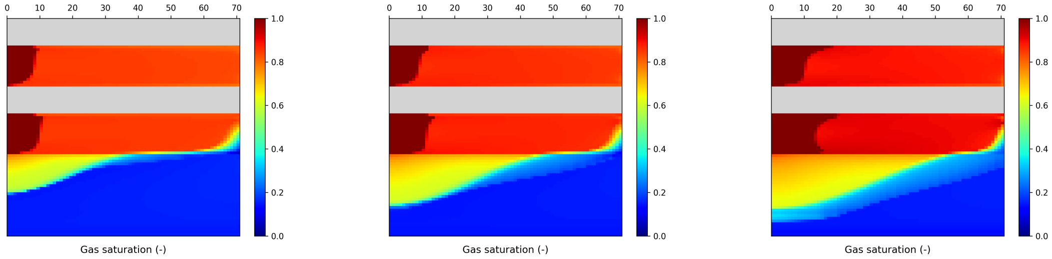

Figure 5.18: Reservoir temperature sensitivity saturation profile after 60 years of CPG. From left to right: low case, base case, high case

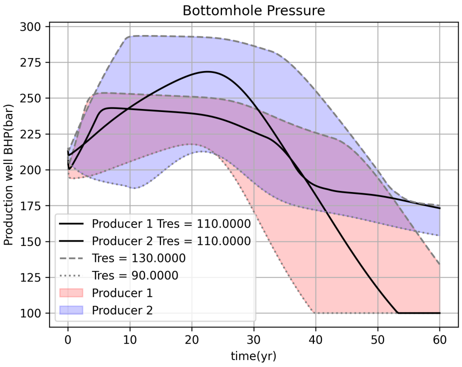

Figure 5.19: Production graphs for reservoir temperature sensitivity test per well

Brine salinity

Three salinities were tested; 0, 1.368 and 3 mol/kg. Salinity affects component phase partitioning, as well as the density of the aqueous phase. Figure 5.20 Shows the resulting saturation profile after 60 years of CPG. We observe that increasing brine salinity greatly reduces the entry of CO_2 into the aquifer.

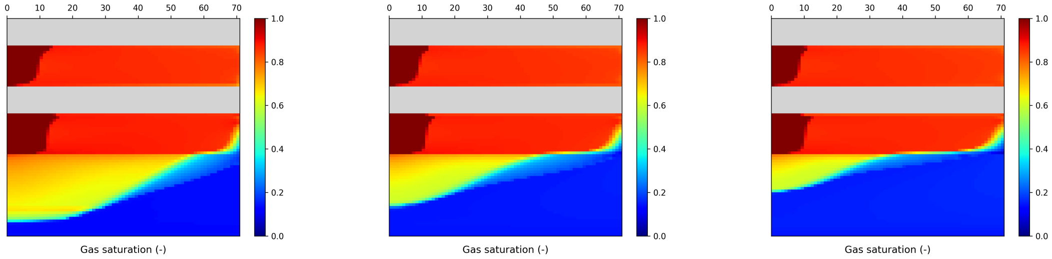

Figure 5.20: Brine salinity sensitivity saturation profile after 60 years of CPG. From left to right: low case, base case, high case

Figure C.4 shows the reservoir wide production graphs. Figure 5.21 shows the production profile split up per formation. It is clear that here as well, the increased density of the aqueous phase reduces the onset of brine upconing. However, we can also observe that there is some perturbation in the mass production rate for P1, which is not expected. One possible explanation is that increasing salinity is associated with reduced brine enthalpy. This means that the temperature front will progress faster. We can see this clearly from the production temperature, which starts dropping earlier for the Cm = 3 case compared to the Cm = 0 case. This also changes the onset time of the BHP perturbations earlier describes caused by the progressing cold front. This showcases some difficulty with analyzing CPG systems: keeping constant production conditions is very difficult to do, as any control variable which might change also influences density and temperature of the produced fluid.

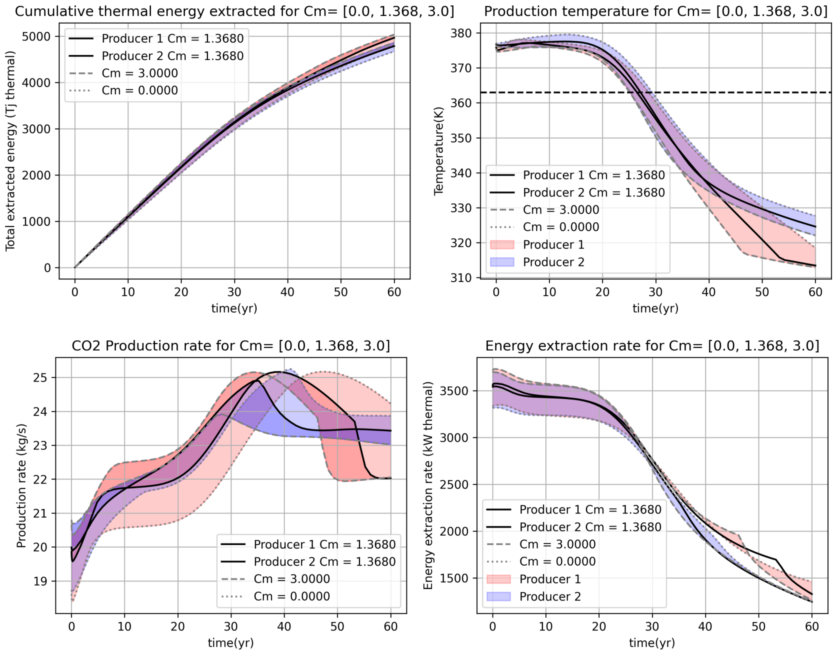

Figure 5.21: Production graphs for salinity sensitivity test per well

Figure 5.22 shows the progression of bottom hole pressure in the sensitivity for both wells. We can see here that the faster progression of the cold front has a significant impact on the BHP required to sustain a volumetric rate, in turn affecting the behaviour of mass production rate.

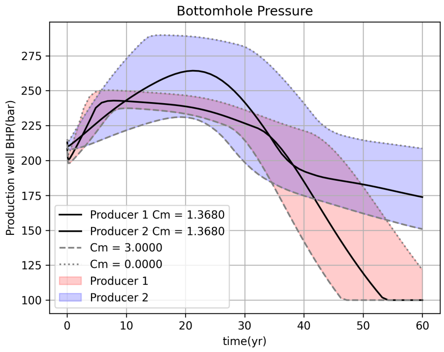

Figure 5.22: Bottomhole pressure profile for the Salinity sensitivty test

5.2.3 Reservoir parameters

Separating layer thickness

In this section, the difference in separating thickness layer and its effect on thermal recharge is explored. Figure 5.23 shows the different configurations, with 5 m being a flow baffle with low recharge potential, whereas the 100 m thick layer has considerable recharge potential and effectively isolates the two formations. We can see that the 5 m layer is completely cooled down after lifecycle, whereas the 100m reservoir still has considerable temperature in the middle.

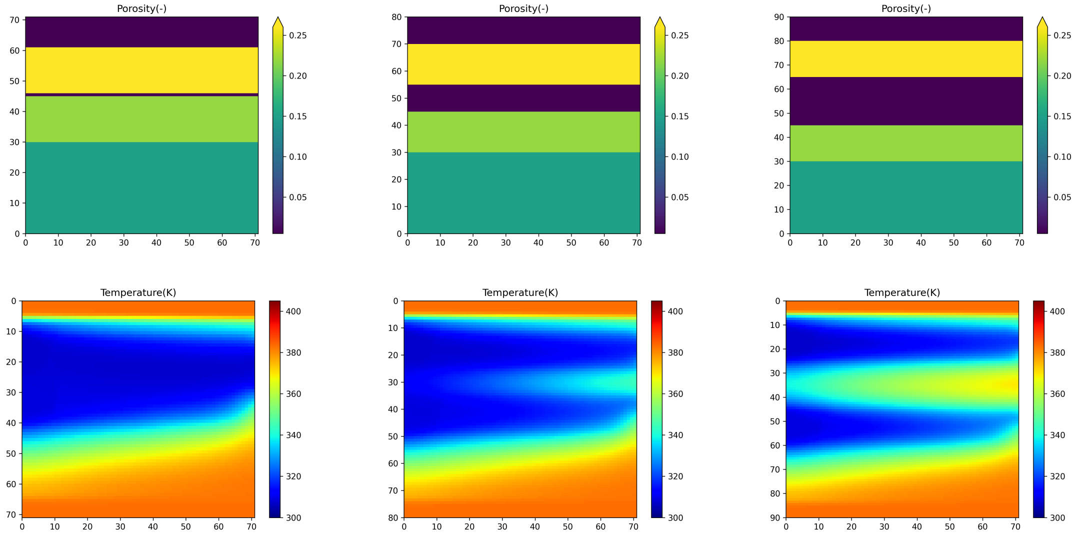

Figure 5.23: Separating layer thickness and temperature profile after 60 years of CPG. from left to right: low case, base case and high case

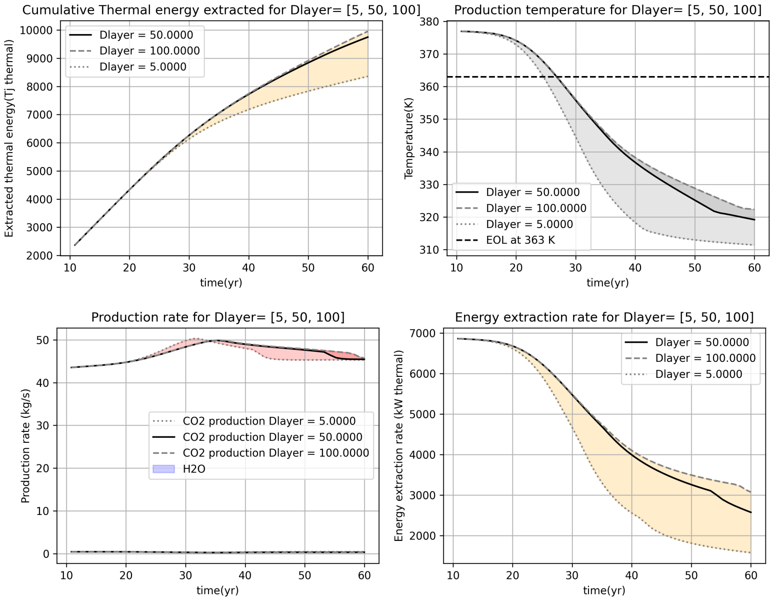

Figure 5.24: Production graphs for separating layer thickness test

Figure C.5 shows the production graphs for the two producing wells, exhibiting similar flow behaviour as earlier described. Figure 5.24 Shows production for the entire reservoir. It can be observed that the effect of the layer recharge only becomes significant after thermal breakthrough. We see that without thermal recharge from the separating layer the drop in temperature is sharper. Whether the extra energy from adjacent layer recharge is useful would depend on the absolute produced temperature and it's resulting exergy in the above-ground installation, as well as well placement and control strategies. For example, lower production rates and larger well spacing would allow for more time for conduction to take place, which would prolong reservoir lifetime.

Vertical permeability anisotropy

In this test, three vertical permeability ratios were chosen: Kv/Kh = 0.1, 0.3 and 0.8. from Figure 5.25 we can see that higher vertical permeability dramatically increases the intrusion of CO_2 into the underlying aquifer. This was the primary reason to deviate from the Pernis model Kv/Kh of 0.8 to 0.3 as the base case for the sensitivity studies.

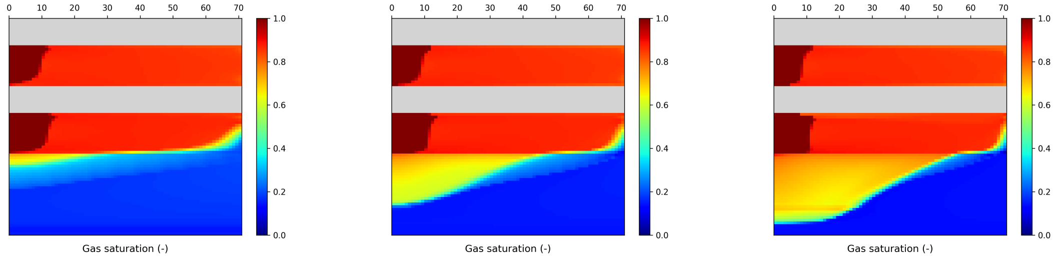

Figure 5.25: Permeability anisotropy sensitivity saturation profile after 60 years of CPG. From left to right: low case, base case, high case

Figure 5.26 shows the well production profiles, confirming that the aquifer interaction is affecting the production profile of P2. P1 is entirely unaffected.

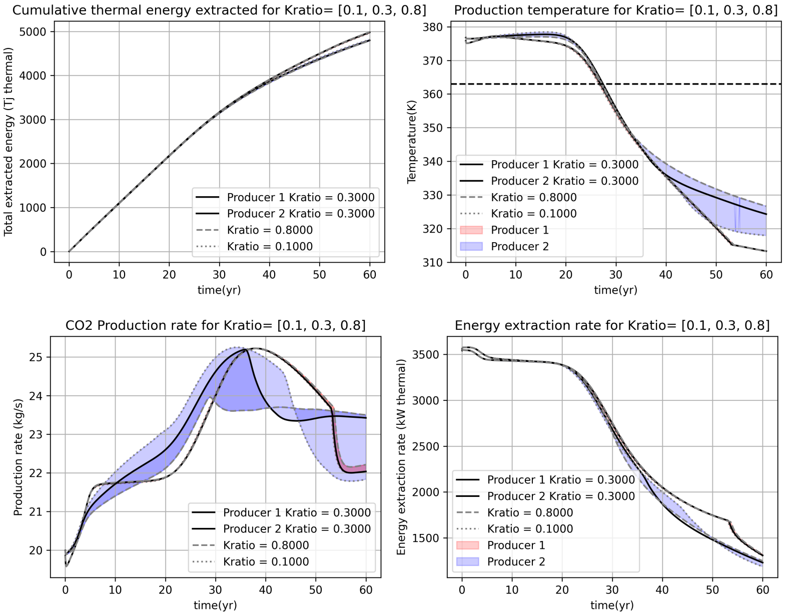

Figure 5.26: Production graphs per well for permeability anisotropy sensitivity test

5.2.4 Parameters of relative permeability

Next, some of the parameters in the Brooks-Corey relative permeability equation were tested. It should be noted that the results from these tests are difficult to interpret, and as such no clear conclusion can be drawn. Value could be added with additional research into multiphase flow behaviour of CPG or thermal CCS systems.

Brooks-Corey gas exponent

First, 3 values for the Brooks-Corey gas exponent governing the relperm curve of the non-aqueous phase were tested. Figure 5.27 shows the saturation profiles after 60 years of CPG, clearly showing the impact the gas exponent has on aquifer interaction.

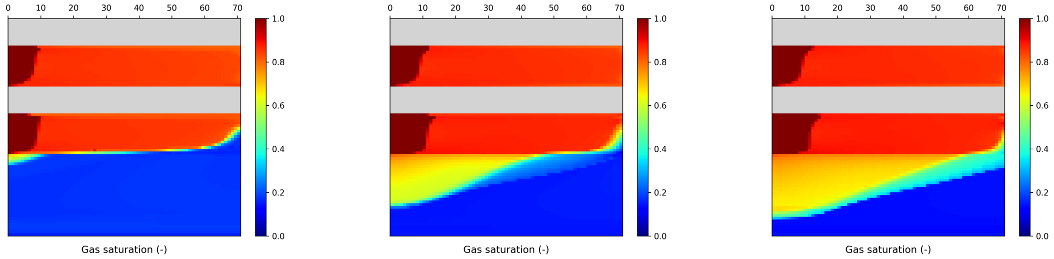

Figure 5.27: Brooks-Corey gas exponent sensitivity saturation profile after 60 years of CPG. From left to right: low case, base case, high case

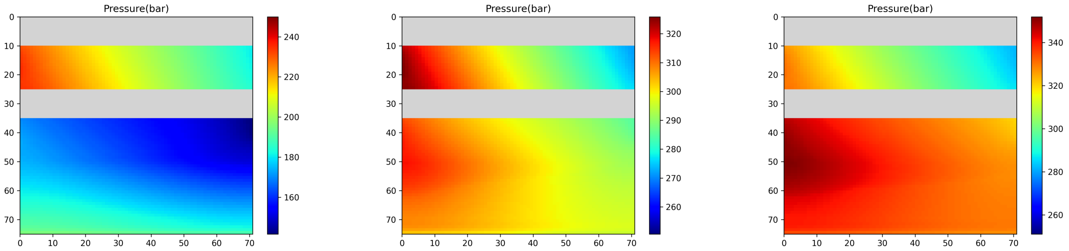

Figure 5.28: Brooks-Corey gas exponent sensitivity pressure profile after 15 years of CPG. From left to right: low case, base case, high case

Figure C.9 shows the reservoir production profiles. Figure 5.29 and Figure 5.30 show the difficulty in interpreting these results. A sharp drop in reservoir pressure in the $n_g = 5$ followed by the reaching of the well constraint induces a sharp spike in mass flow rate, rendering the results not very conclusive. One possible cause might be the fact that high exponents are associated with lower relative permeability at high saturation. The reservoir is initialized at connate water saturation, but elevated injection pressures compress the non-aqueous phase, increasing the relative volume of the aqueous phase above connate saturation. This means that $k_{r,naqp} < 1$, and effects of the gas exponent become visible. This might also explain why P1 is also affected in a similar manner.
Figure 5.28 shows the pressure profiles after 15 years of CPG for the three cases. Here we can observe that pressure drops faster travelling from the injection to production wells. This indicates reduced relative permeability for the non-aqueous phase at high phase saturation.

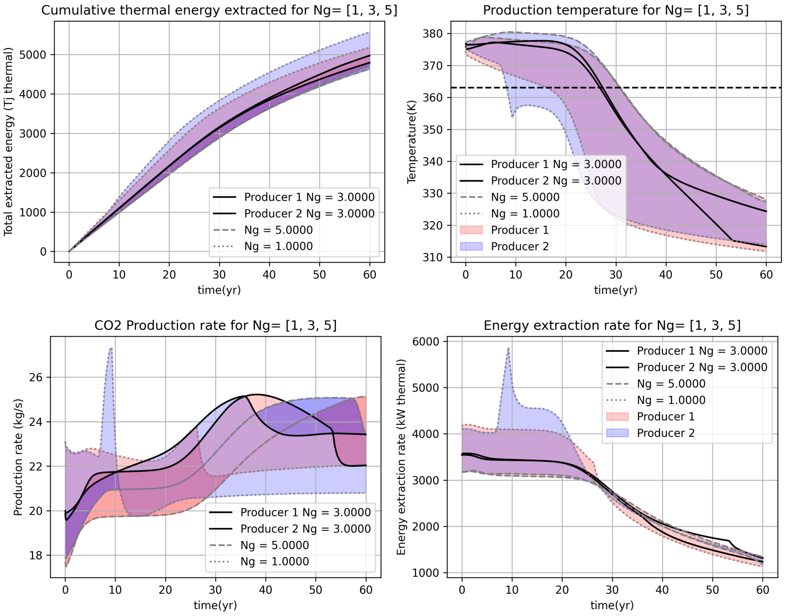

Figure 5.29: Production graphs per well for Brooks-Corey gas exponent sensitivity test

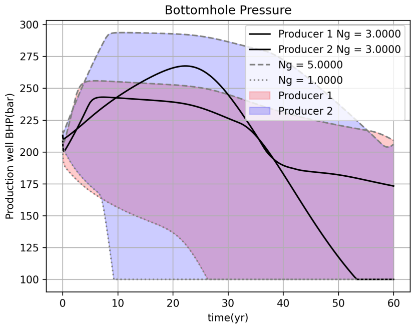

Figure 5.30: Production well BHP profile for Brooks-Corey gas exponent test

Brooks-Corey water exponent

In this test, the Brooks-Corey water exponent governing the relative permeability curve shape for the aqueous phase was varied. Figure 5.31 shows the the effect of the water exponent on the saturation profile. We observe increased brine upconing with a lower water exponent, possibly because the water is more mobile at lower saturations, meaning easier entry. A higher water exponent is associated with increased entry of CO_2 into the aquifer. However, we also observe that the gas saturation in the displacement depression is lower as the water exponent increases. This corresponds to a sharper drop in relative permeability for the non-aqueous phase at higher water exponents.

Looking at the production profiles in Figure 5.32, we can observe that there is a minor difference in production figures across the exponent tests. This is caused by a difference in reservoir impedance caused by the different aquifer interactions. This in turn causes a change in production BHP as shown in Figure 5.33 with resulting fluctuations in density and temperature.

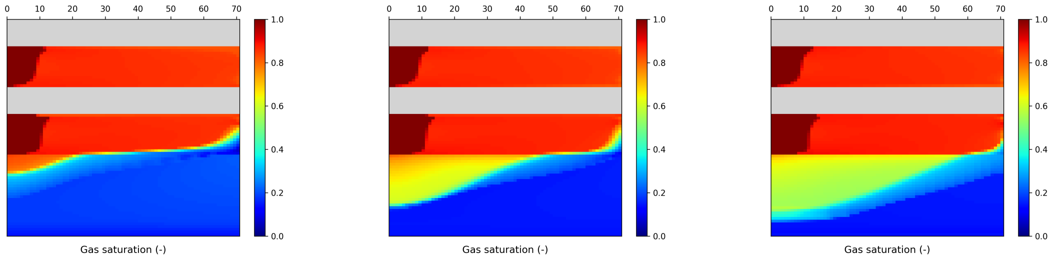

Figure 5.31: Brooks-Corey water exponent sensitivity saturation profile after 60 years of CPG. From left to right: low case, base case, high case

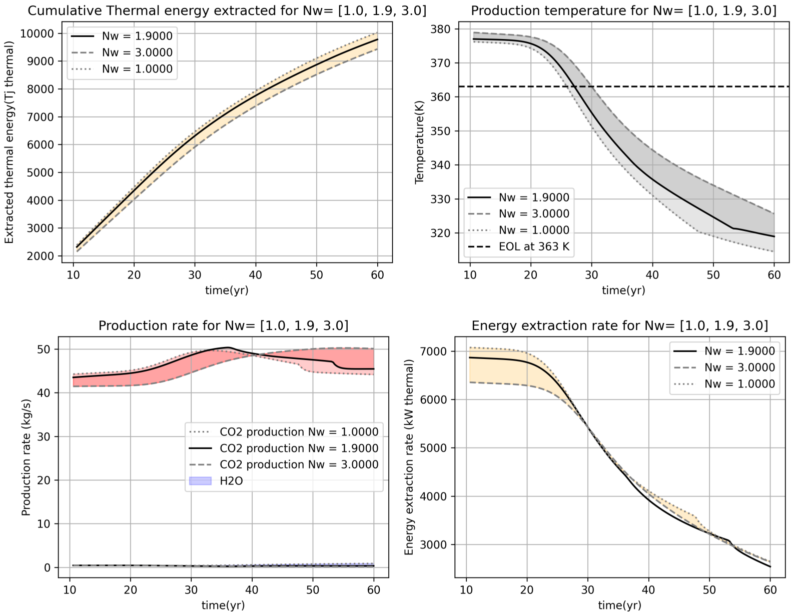

Figure 5.32: Production graphs per well for Brooks-Corey water exponent sensitivity test

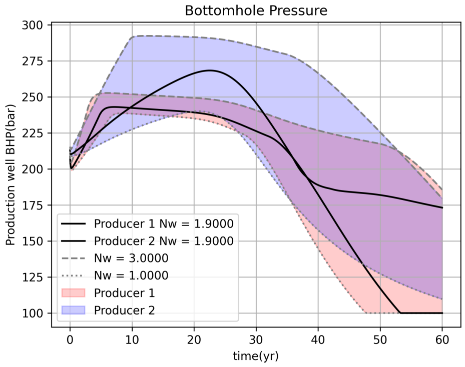

Figure 5.33: Production graphs per well for Brooks-Corey water exponent sensitivity test

5.2.5 Thermal parameters

Rock heat capacity

In this test, heat capacity of all rocks in the reservoir was scaled by a factor of 0.8, 1 or 1.2 in order to simulate potential different minerologies. Figure 5.34 shows the resulting production figures for all three tests. It is observed that increasing heat capacity is favourable for the lifetime of the system, much in line with what one would expect. No deviant behaviour was found in the well production profiles.

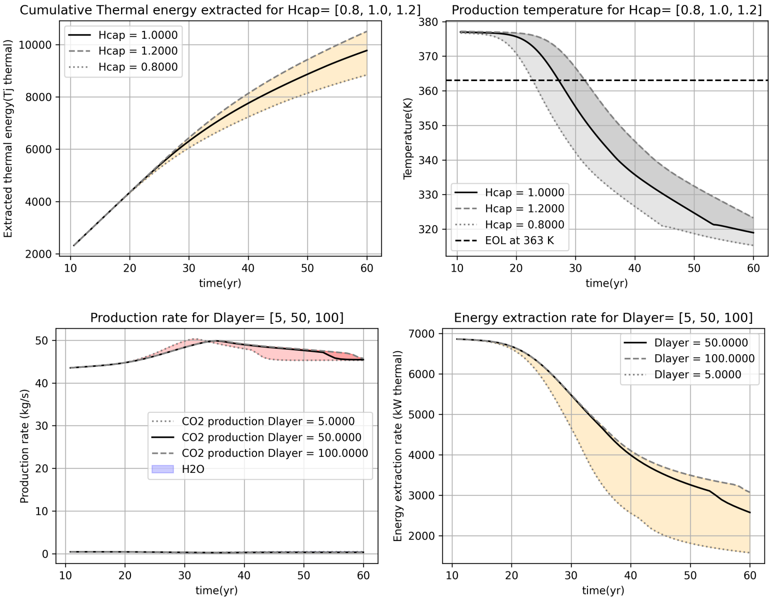

Figure 5.34: Production graphs for the heat capacity sensitivity test

Thermal conductivity

Microscale laminations and changes in minerology can give rise to thermal conductivity anisotropy. In our 2D layered system, this can quite conveniently be described as a change in thermal conductivity as conduction predominantly occurs in the vertical direction. Rock thermal conductivity was scaled with factors 0.5, 1 and 1.5. This variation corresponds to the variation seen from research on thermal conductivity anisotropy [8]. The resulting temperature distribution after 60 years of CPG is shown in Figure 5.35. It is observed that increased thermal conductivity aids in the thermal recharge from the separating layer.

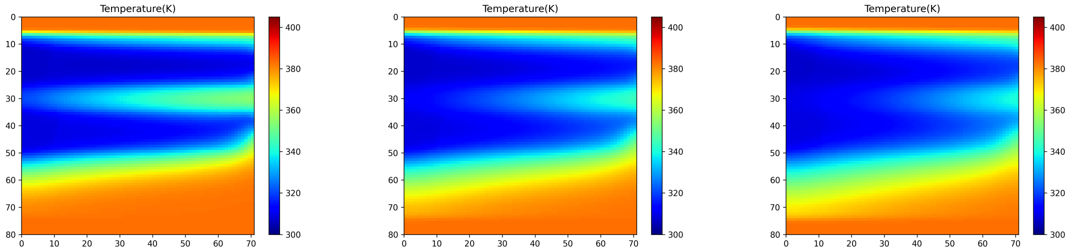

Figure 5.35: Thermal conductivity sensitivity temperature profile after 60 years of CPG. From left to right: low case, base case, high case

Figure 5.36 Shows the production profile for the sensitivity tests. No effects other than the ones previously described are noted. This means that a higher thermal conductivity is favourable for the thermal recharge from impermeable section of the reservoir, and a change in thermal conductivity does not give rise to other notable effects.

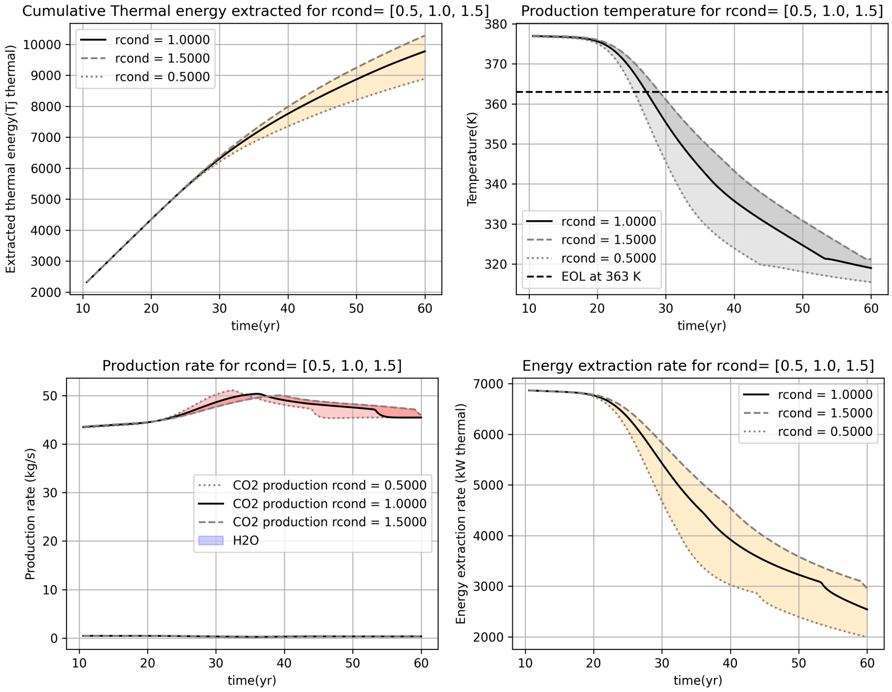

Figure 5.36: Production graphs for the thermal conductivity sensitivity test

5.2.6 Control parameter

In this section, we discuss well control parameters. Due to time constraint, only the injection surplus has been discussed. Other well variables such as well spacing [4], wellbore diameter and flow rate [2] have been extensively studied in literature.

Injection surplus

In order to explore further the effect of the pressure distribution on the reservoir, as well as explain the decision to increase the injection rate in the 2D sensitivity study, a comparison study was done with different injection well rate controls. Figure 5.37 shows the different pressure profiles after 15 years of CPG for the base case (left) and comparison (right). Figure 5.38 shows the large difference in production temperature caused by lower producer BHP. Resultant energy extraction is more or less constant.

Looking at Figure 5.39 it can be seen that the base case with overinjection has higher mass flow rate and higher production temperature but similar thermal energy extraction. This is caused by higher pressure being correlated with lower enthalpy. This means that thermal energy extraction is not a good indicator of the performance of a CPG system, as this pressure can be converted into power by a turbine, hence these two cases will have different resultant exergies. This clearly shows the difficulties of modelling CPG systems without a coupled wellbore and power plant model. Figure 5.37 shows the strong difference in producer BHP between the two models. We also see that the fluctuations in the mass production rate origi-

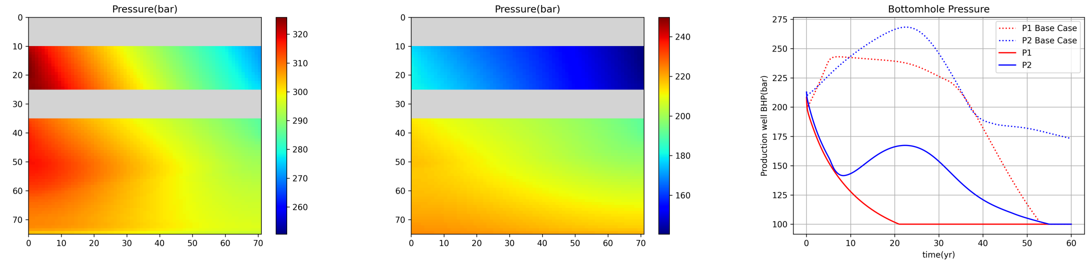

Figure 5.37: Pressure distribution after 15 years of CPG for the injection surplus comparative test, as well as the pressure profile in the production wells

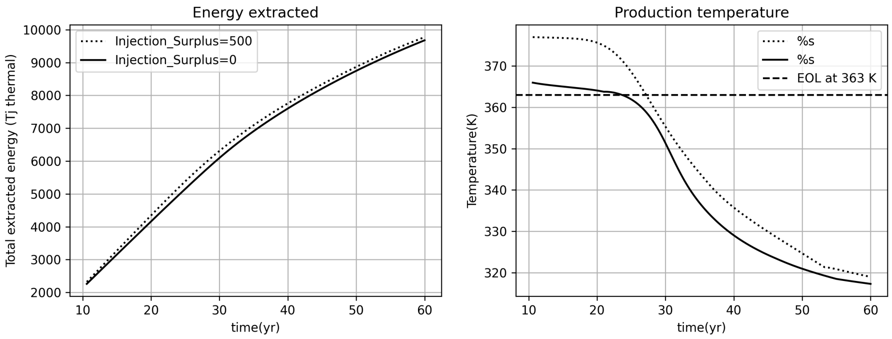

Figure 5.38: Production graphs for the injection surplus comparative test

nate from fluctuations in the BHP, For example, the dip in mass production rate in P2 in the comparison run around 12 years corresponds to a low point in BHP around the same time.

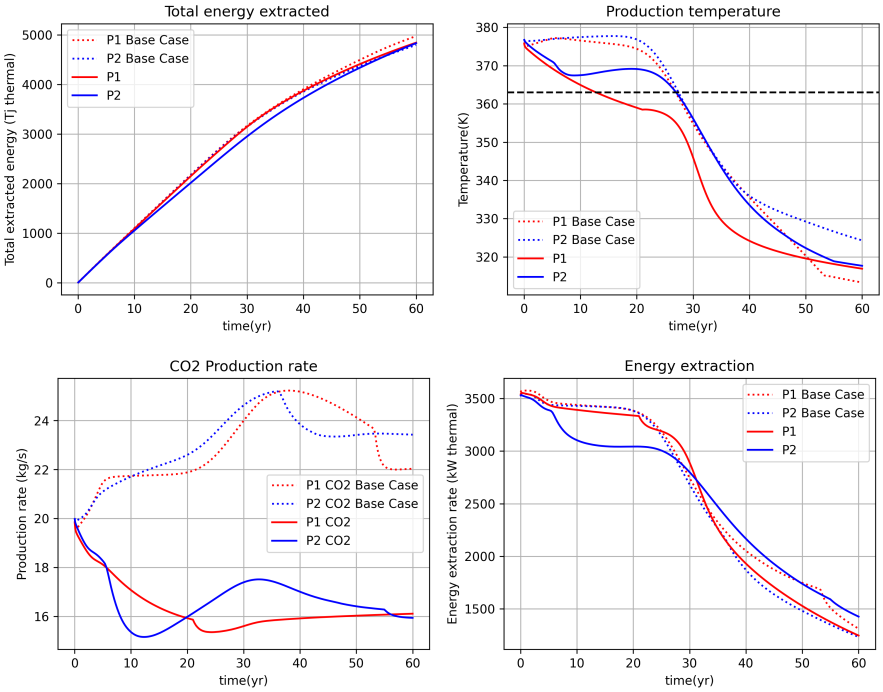

Figure 5.39: Production graphs per well for the injection surplus comparative test

5.3 Results of 3D Simulation Study

5.3.1 Results from the 3D-box case

It should be noted that in these results, only the production figures from the P1 well in the Holland Greensand formation is considered, as the de Lier realizations had problems with reservoir connectivity. Figure 5.40 shows the within-layer N/G variation for the two productive formations. It is clearly visible that the de Lier formation has a within-layer N/G that is substantially lower, which causes these connectivity issues. Figure 5.40 also shows the results from the geometric mean upscaling of the Holland Greensand formation. As is visible, mean permeability is on the low end, but appears to be consistent with quantities described in petrophysical analysis from the adjacent MNZ field [54].

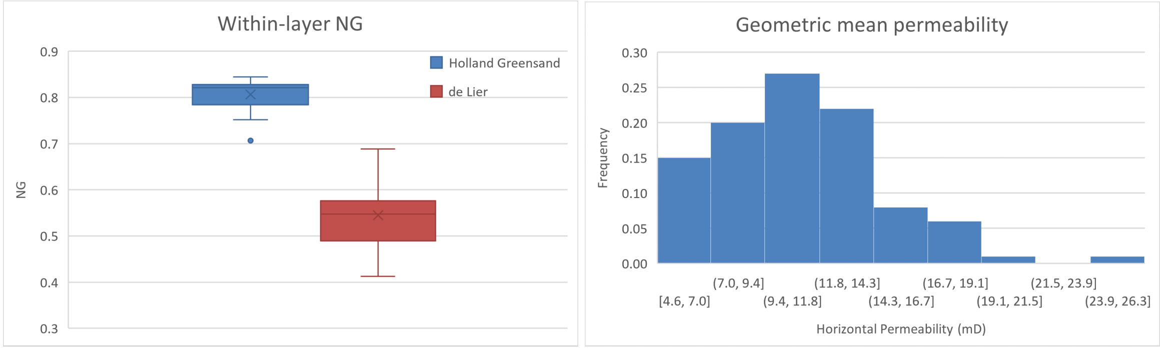

Figure 5.40: Reservoir information for the 3D Box model cases

For the 3D base case, volumetric production rate was set to $10000m^3/day$ nonaqueous phase at bottomhole conditions with a BHP constraint at 100 bar. Subsequently, the four production wells at the corners of each realization were set to $2550m^3/day$ nonaqueous phase at bottomhole conditions with a BHP constraint at 375 bar. 100 realizations with different facies and porosity distributions were run, as well as 100 realizations of the respective geometric mean upscaled permeabilities with porosity adjusted to realize similar pore volume between the two realizations. Figure 5.42 Shows the temperature profile for the base case realizations and their homogeneous counterparts. We can note a few things; mean time for the thermal breakthrough is quick, with the mean breakthrough at 17 years. This is caused by preferential flow paths in the realizations as showcased by Figure 5.41. However, connectivity is quite good, and the majority of realizations follow a similar temperature profile. The homogeneous realizations show that the upscaled permeability is too low to allow for this volumetric rate to be sustained. Thus, two more sets will be run; one with lower rate and another with higher permeabilities.

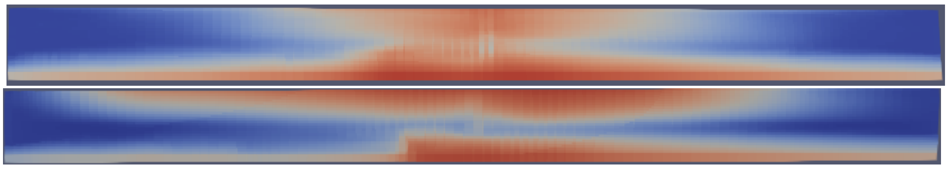

Figure 5.41: Graphs showing sideview temperature distribution for the best performing realization (top) and worst performing realization (bottom) after 30 years of CPG

Looking at Figure 5.43, we note that for the first 25-30 years, cumulative thermal energy extraction is very similar. This is caused by the earlier noted fact that on volumetric rate control,

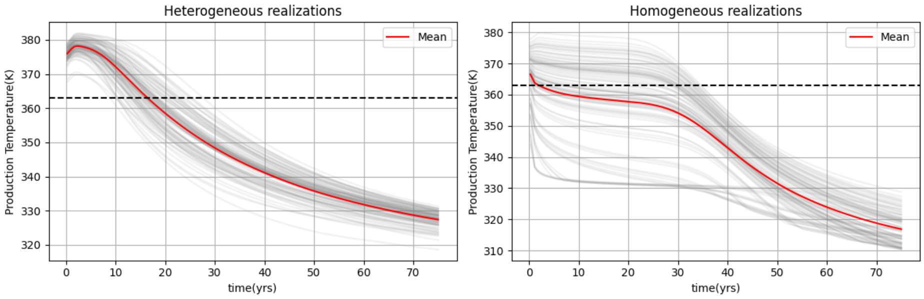

Figure 5.42: Temperature profile for the 3D-box model case

reduced temperature corresponds to higher mass flowrate and resulting total energy production, This is reinforced by the variation in mass production rates seen in Figure 5.43.

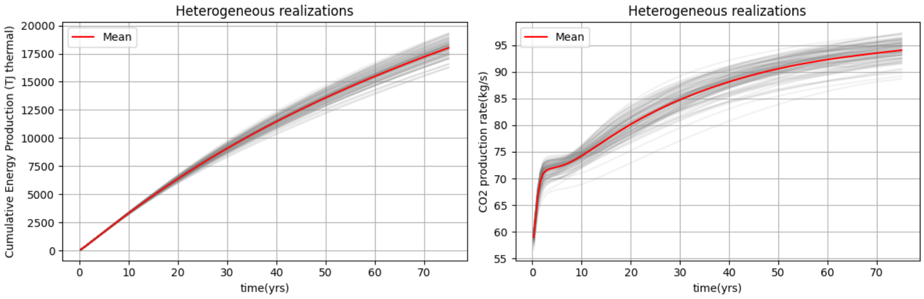

Figure 5.43: Thermal energy extraction and mass flowrate for the 3D box base case realizations

As mentioned in chapter 4, the realizations were made from 25 facies realizations with 4 porosity realizations each. A scatter plot showing cumulative thermal energy extraction across facies realizations with the facies mean in grey is shown in Figure 5.44. We observe that while some facies realizations(e.g. #6 and #8) show very low spread, this low spread is not consistent across realizations. Additionally, by only looking at porosity distributions within a single facies realizations, we reduce the randomness in the system. Thus, we can conclude that both facies and within-facies porosity distribution are important for thermal performance.

5.3.2 Results from the 3D-box model with lower flow rate

As discussed in the previous section, production rates were reduced in this run in order to reduce the problems with low upscaled permeability. In this case, volumetric production rate was set to $7000m^3/day$ nonaqueous phase at bottomhole conditions with a BHP constraint at 100 bar. Subsequently, the four production wells at the corners of each realization were set to $1800m^3/day$ nonaqueous phase at bottomhole conditions with a BHP constraint at 375 bar. Figure 5.45 shows the temperature profile for the heterogeneous and homogeneous realizations at lower production rate. We note a clearly increased mean lifetime for the heterogeneous realizations at 30.7 years. However, the homogeneous realizations still struggle with the low geometric mean permeability, making direct comparison difficult. Figure C.16 shows the cumulative thermal energy extraction and mass production rate for the low rate

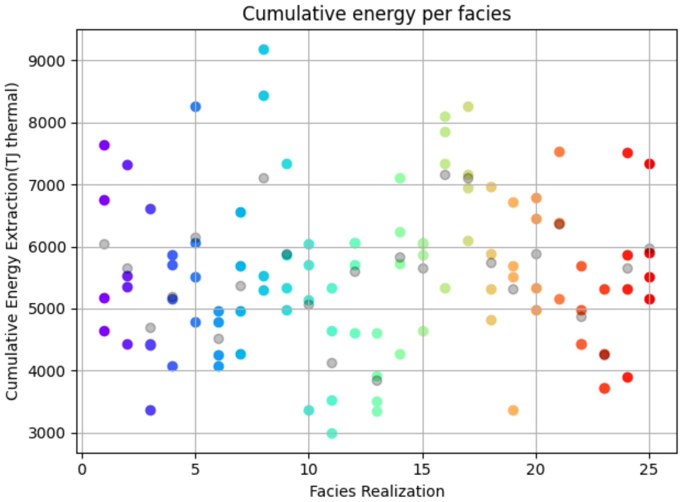

Figure 5.44: Scatter plot of cumulative energy extraction for every facies realization with facies mean in grey

run. No important differences compared to Figure 5.43 are noted.

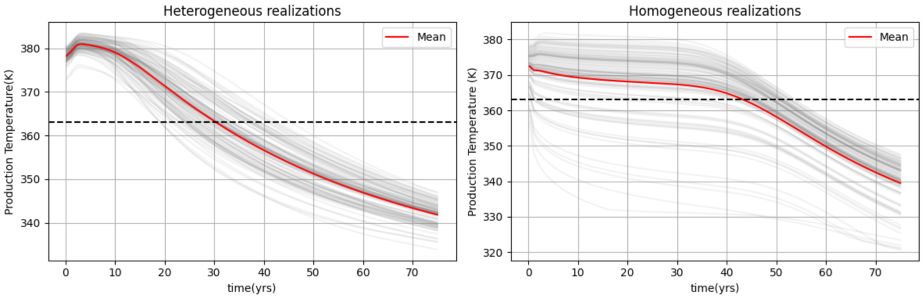

Figure 5.45: Temperature profile for the 3D Box Model Base case

Comparing the production profiles of the heterogeneous base case with the low production rate in Figure 5.46. We note three important differences compared to the Base Case. Mean temperature in the early stages of the production cycle is higher, caused by a higher producer BHP. Secondly, reservoir lifetime is substantially longer. Lastly, there appears to be a larger spread in thermal breakthrough times compared to the Base Case. In order to get a better feel for the quantitative differences, thermal performance is set out on a scatter plot shown in Figure 5.47.

Scatter plotting cumulative energy extracted versus reservoir lifetime for the two runs showcases some interesting trends. Firstly, a clearly linear trend between lifetime and cumulative energy extraction is visible, which is to be expected given the rate control. However, the slope of the two linear curves is different. This slope should correspond to the different rate controls and thus energy extraction. Large differences are noted in the minimum lifetime, as well as energy extracted. The worst case at low rate has twice the lifetime compared to the worst base case realization. Also, reducing the rate increases cumulative thermal energy extracted, which appears to indicate that reducing rate reduces the effect of fingering and increases the recovery factor of the reservoir. For the Base Case mean lifetime and cumulative thermal energy extraction are 17.0 years and 5503 TJ thermal respectively, the low rate at

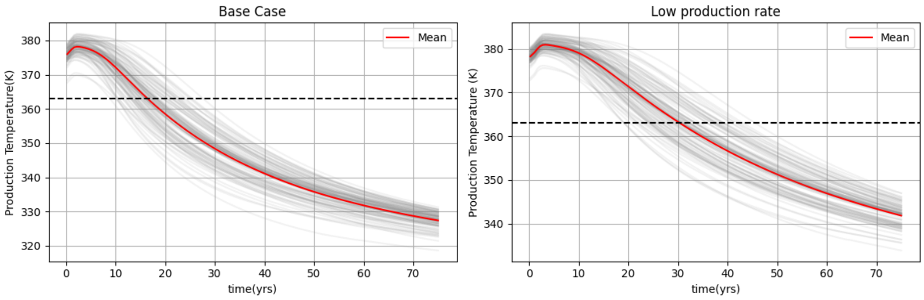

Figure 5.46: Production temperature for 3D box base case and low production case

30% lower volume rate control has mean of 30.7 years and 6987 TJ thermal respectively. This means that reducing production rate by 30% corresponds to a 27.0% increase in total energy extraction and a 80.7% increase in mean lifetime, indicating that heterogeneous reservoirs favor a lower production rate. It should be noted that the large increase in lifetime might be caused by a combination of improved sweep and increased conduction, as well as higher production temperatures induced by higher production BHP.

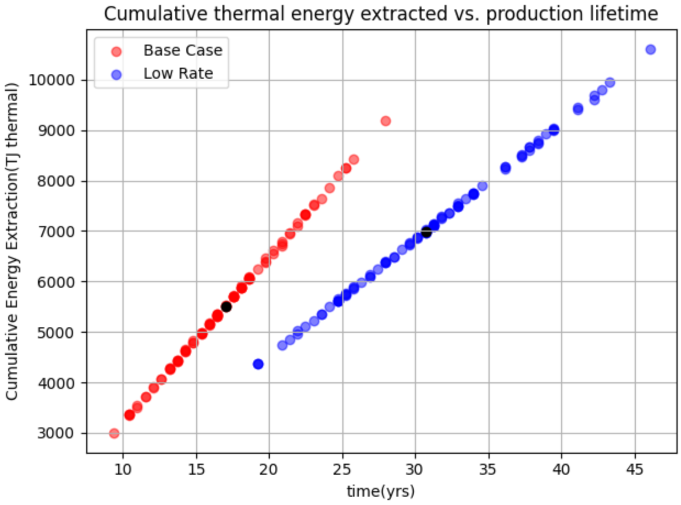

Figure 5.47: Scatter plot of thermal performance for the 3D box base case and low rate case heterogeneous realizations

5.3.3 Results from the increased permeability in 3D-box case

In this run, permeability of net rock in the heterogeneous realizations as well as the homogeneous realizations were increased by a factor of three, in order to try to eliminate the connectivity issue in the upscaled realizations. Figure 5.48 shows a temperature profile comparison between the heterogeneous base case and increased permeability case, A slight increase in mean lifetime from 17.0 to 19.8 years can be observed, which is caused by higher production BHP limiting expansive cooling.

Figure 5.49 shows the difference between the heterogeneous and homogeneous geometric mean upscaled realizations at higher permeability. Here, permeability of the homogeneous realizations is high enough to showcase the large reduction in lifetime from 35.1 to 19.8 years

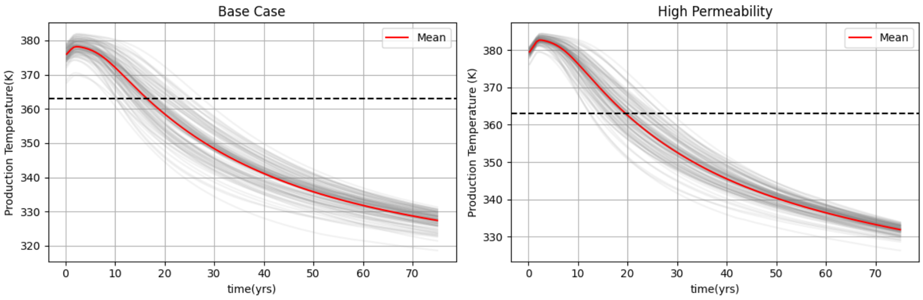

Figure 5.48: Temperature profile comparison for the heterogeneous base case and increased permeability realizations

caused by heterogeneity. This corresponds to a 43.6% reduction in lifetime due to the effect of porosity and permeability heterogeneity.

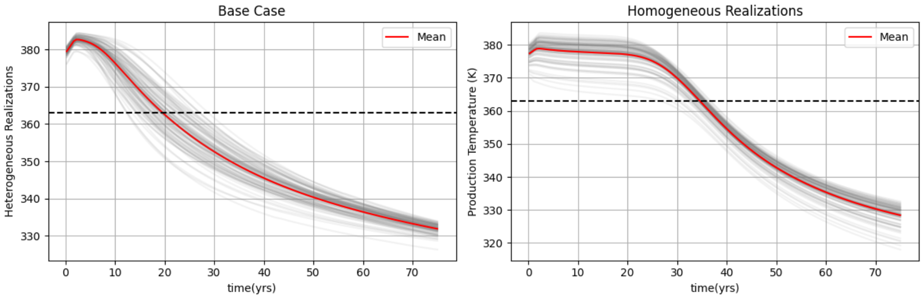

Figure 5.49: Temperature profile comparison for the heterogeneous and homogeneous increased permeability realizations

Chapter 6

Conclusions

6.1 Discussion

Thermal compositional model

The current thermal compositional model built for this study does not contain effects of capillary pressure and diffusion. A decision was made early in the project to leave out these variables, as they would further increase computational demands without introducing significant changes to results. However, it would not be difficult to consider these effects in further studies. Likewise, in the current model, the effects of salt precipitation or variation in the salinity have not been accounted for. These phenomena can affect injectivity around the wellbore, as we did observe substantial reservoir dry-out near the injection well in the 2D sensitivity experiments. This can also affect the pressure distribution throughout the reservoir which can exacerbate the discussed challenges with maintaining high production flow rates.

In our study, the properties have been validated up to 130°C and 400 bar as this is in the range of interest for realistic applications. There should be no difficulty in extending the model to higher pressures. Increasing the temperature limit might prove more challenging. Some of the phase properties, such as the different correlations computing dynamic viscosity and thermal conductivity, use correlations that might already not cover the entire range of states of interest. This necessitated extensive validation of all properties in order to ensure that the modeling study happened in appropriate range.

Macroscale heterogeneity test

The 2D macroscale heterogeneity test showcased the strength of the OBL approach, allowing 5000 albeit simple realizations to be run over the course of several hours. It should be noted that at this stage of model development, rate control was not available yet. Thus, the decision was made to run the realizations on BHP control. This meant that the mass flow rates through the reservoir did vary with N/G ratio. In analyzing the results, an attempt was made to correct for this effect by using different variables in order to get an idea of the importance of within-layer N/G and the specific distribution of impermeable rock.

When selecting a site for CPG, layered reservoirs might prove to be excellent choices for real application. As our results show, a large proportion of distributed impermeable rocks aides in thermal recharge of productive formations. Layered formations can aid in distributions of the CO_2 plume where it might buoyantly rise to the top of a massive formation in aquifer injection CPG, as illustrated by Garapati et al. [29].

For simplicity the decision was made to work with two discrete homogeneous lithologies. There are currently no simple measures of vertical heterogeneity for geothermal systems, as conventional statistical approaches (e.g. Dykstra-Parson coefficient) do not take into account the actual spatial distribution of permeability. The results of our simplified model already show that the spatial distribution of permeability zones can play a significant role in the resultant behaviour of any geothermal system.

Sensitivity study

The Pernis field productive formation permeability is in the order of 5-30 mD $(10^{-15}m^2)$. This is at the very low end of feasible formations denoted in literature [4]. As a result of this, maintaining substantial flow rate required very large pressure drops in the production wells. This gave rise to a series of emergent behaviours such as coning of aqueous brine. This phenomena requires a maintaining of flow rate with progressing thermal front. Results regarding very strong expansive cooling and hitting the 100 bar production well constraint should not be directly translated to more permeable formations, but give an important insight into the different dynamics that go into a CPG system. The drop in performance due to low permeability is also discussed in [4].

For our model, volumetric rate constraint was employed. This differs from the mass control used by other CPG studies. For hydrothermal systems, this difference is minimal, but the expansive nature of CO_2 combined with the large pressure fluctuations at the production well meant that mass flow rate, energy extraction and production temperature were subject not only to heat transfer from the reservoir to the working fluid, but also to the varying temperature, pressure and density caused by expansion near the production wellbore. This caused complications with analyzing in much detail the different sensitivity runs, but also shows an opportunity in optimizing well controls which is not available in the low compressible conventional geothermal systems.

This optimization necessarily needs to be done in context of a coupled wellbore and infrastructure model. For example, our injection surplus comparative test shows higher pressure, temperature and mass flow rates for increased volumetric injection rate. However, this does not translate to purely increased enthalpy production, and also raises the question of how increased surface compression at the injection wellhead influence the resulting power output. Thus, we can see that coupled wellbore and infrastructure models are vital in order to properly analyze CPG systems.

Full-field 3D study

The 3D box model cropped from the Pernis model showed poor connectivity in the de Lier formation caused by layers of impermeable rock. Due to this, the decision was made to use only the results from the top formation which does not have these issues. This means that aquifer interaction is not studies in these tests. Visual inspection of different porosity realizations did show that the well constraining succeeded in creating SIS realizations with different facies and porosity distributions, but with large features remaining similar. The geometric mean upscaling procedure showed some issues with very low mean permeabilities, necessitating some extra runs with increased permeability. This does however showcase some interesting property of the CPG system: the high mobility of $scCO_2$ aides connecting producer-injector pairs in formations where the upscaled properties might not be as conductive to flow. The trade-off is a reduced reservoir lifetime due to preferential flow paths, the effect of which can be partially counteracted by reducing production rate. This given an interesting extra consideration to the design of CPG systems compared to earlier research that CPG production in homogeneous reservoirs performs better with higher production rate. This contradiction warrants extra investigation into the trade-off between higher flow rate with low lifetime versus lower flow rate with increased lifetime and energy production.

6.2 Conclusion

In this thesis, a DARTS model for nonisothermal injection of CO_2 into depleted gas reservoirs was built. Using the model, different scales and types of reservoir heterogeneity were thoroughly studied, The following conclusions can be drawn:

Thermal compositional model

- The dynamic model is a two-phase three-component thermal model validated between 50-400 bar pressure and 35-130$^\circ C$ Temperature. Two phases are distinguished in our study which include aqueous and non-aqueous (supercritical fluid), with the three components being CO_2,CH_4 and H_2O. The equation of state is built using a fugacity-activity model with fugacity based on a modified Peng-Ronbinson EOS. Component phase partitioning, phase density, dynamic viscosity, thermal conductivity and relative enthalpy are dependant on pressure, temperature, fluid composition and salinity. The enthalpy function takes into account enthalpy of dissolution, enthalpy of vaporization and variations in pressure and temperature. Component phase partitioning and resulting phase properties have been validated to be accurate in the range of interest.

Macroscale heterogeneity test

- Experimenting on an ensemble of layered 2D reservoirs, it was shown that increasing formation N/G reduced the energy produced per m^3 of net rock. In addition the variation in energy produced per m^3 of net rock increases strongly at low N/G ratios. This is caused by an increased importance in the degree of layering and specific order and thickness distribution of layers at low N/G ratios.

- Increasing N/G ratio is associated with increasing recovery factor. However, the spread of recovery factors increases as net-to-gross decreases. This is caused by a sensitivity to the degree of layering mainly at low ($\leqslant 0.5$) N/G values. This indicates that distribution of impermeable parts of a formation becomes important to thermal performance mainly at lower N/G ratio.

- Convective flux is more important than conductive flux by 2-5 orders of magnitude. However, for low N/G and highly layered reservoirs, the conductive flux significantly increases the lifetime of a CPG development.

Sensitivity tests

- The initial state of the reservoir has a significant impact on CPG performance, especially with regards to aquifer interaction. Lower reservoir pressure increases the density contrast between the aqueous and non-aqueous phases, reducing coning effects. Increasing reservoir temperature increases thermal energy extraction, and also increases density contrast between the aqueous and non-aqueous phase. Increasing brine salinity is associated with an increases phase density contrast, resulting in reduced brine coning. No water is produced across tests, but the presence of the cone does influence relative permeability of the non-aqueous phase, which increases the BHP drop required for production. Additionally, increasing brine salinity reduced phase relative enthalpy in both the aquifer and connate water, resulting in slightly lower energy extraction.

- Variation in the separating layer thickness shows that the thickness of this separating layer has an effect on the steepness of the thermal breakthrough, extending the total lifetime of a CPG development. An increasing K_v/K_h ratio is associated with increased brine coning and flow of supercrtical CO_2 in the aquifer. For formations underlain by an impermeable underburden, variation of this ratio has no effect on flow behaviour.

- An increase in the thermal rock parameters rock heat capacity and thermal conductivity shows improved thermal performance. This is caused by higher available energy and improved recharge from adjacent unproductive layers. No notable effects on flow behaviour were noticed as expected.

- Setting a higher injection than production rate appears to be beneficial to the performance of a CPG system. This is a unique feature of CPG systems compared to conventional geothermal systems, as the production BHP has significant influence on the pressure and temperature of the produced fluid. By increasing the injection rate, the required production BHP for a certain mass or volume flow rate increases, which reduces the effect of expansive cooling near the wellbore. Additionally, this increased production pressure can be converted by a direct cycle turbine into power. A study with an additional wellbore and power plant model is required to properly characterize the effect of this phenomenon.

Full-field 3D Study

- The large mobility of $scCO_2$ means that heterogeneous formations with low upscaled permeability can sustain large flow rates. Variation in performance is seen in two factors: production temperature governed by the required BHP to sustain a certain flow rate, and lifetime before thermal breakthrough governed by preferential flow paths.

- For a single well constrained reservoir model with 100 realizations, resulting cumulative thermal energy extraction varies by a factor of three. Variations are dependent on facies distribution and within-facies porosity distribution.

- Reducing production rate affects thermal performance. Reducing production rate in our tests by 30% corresponds to a 27.0% increase in mean total energy extraction and a 80.7% increase in mean lifetime. This is caused by compounding effects of increases sweep efficiency, larger impact of conductive flux and higher production well temperature.

- Tests with increased permeability revealed that porosity-permeability heterogeneity strongly reduces lifetime till thermal breakthrough compared to the homogeneous reference. This is caused by the existence of preferential flow paths in the reservoir. The amplitude of this reduction can be diminished by reduced production rate.

6.3 Recommendations

- It is important to analyze thermal production with a coupled wellbore and infrastructure model. In our project, due to time constraints, the decision was made to not link the production data to a coupled wellbore and turbine model. However, our experiments show that heterogeneities and uncertainties can affect the specific temperature and pressure at which supercritical CO_2 is produced. For example, we note that in our volumetric rate control tests, lower production BHP translates to lower temperature but a higher mass flow rate with similar resultant energy production rate. However, the exergy resulting from these two might be very different, and it would prove very valuable to link the heterogeneous models to a turbine model to see the actual effect on exergy, power production and NPV.

- More extensive testing on geological heterogeneity is needed. This research looked at a variety of basic reservoir structures, different rock properties including absolute permeability and and relative permeabilities. However, the permeability realizations used in this study were based on a well constrained sequential Gaussian porosity distribution. While this is more informative than a homogeneous reservoir, true facies distribution is not random, but dependant on depositional environment and diagenesis. Additionally, the effect of natural fractures and faults has been left unstudied. Research these topics would provide an even better understanding of favourable geologies.

- More research for the effect of relative permeability and capillary pressure is required. The 2D sensitivity experiments on Brooks-Corey exponents were inconclusive. Additionally, capillary pressure was neglected in our model. In order to have a complete picture of the effect of reservoir property variation, it would be valuable to perform additional experiments with heterogeneous capillary pressure.

- EGR and repressurization stage optimization was not considered in our study. [24] showed that CO_2 injection in strongly depleted reservoir can induce strong cooling effects around the injection wellbore. Additionally, experimental results appear to indicate that overinjecting and thus raising average reservoir pressure during the CPG stage might have a positive effect on system performance. Thus, it would be valuable to investigate at which pressure to commence EGR with the goal of reducing reservoir cooling and increasing CPG performance.

- When brine coning reaches the production wellbore, a drop in temperature associated with reduced BHP was observed. Due to time constrains it was not investigated, but it would be useful to study the behaviour of relative permeability and fractional flow around the production wellbore over the lifetime of a CPG well.

Bibliography

[1] B. M. Adams. "On the Power Performance and Integration of Carbon-dioxide Plume Geothermal (CPG) Electrical Energy Production". PhD thesis. University of Minnesota, 2015.

[2] B. M. Adams et al. "A comparison of electric power output of CO2 Plume Geothermal (CPG) and brine geothermal systems for varying reservoir conditions". In: *Applied Energy* 140 (2015), pp. 365–377. ISSN: 03062619. DOI: `10.1016/j.apenergy.2014.11.043`.

[3] B. M. Adams et al. "Estimating the Geothermal Electricity Generation Potential of Sedimentary Basins Using genGEO (the generalizable GEOthermal techno-economic simulator)". In: *ChemRxiv Preprint* (2021).

[4] B. M. Adams et al. "Heat depletion in sedimentary basins and its effect on the design and electric power output of CO2 Plume Geothermal (CPG) systems". In: *Renewable Energy* 172 (2021), pp. 1393–1403. ISSN: 18790682. DOI: `10.1016/j.renene.2020.11.145`. URL: `https://doi.org/10.1016/j.renene.2020.11.145`.

[5] B. M. Adams et al. "On the importance of the thermosiphon effect in CPG (CO2 plume geothermal) power systems". In: *Energy* 69 (2014), pp. 409–418. ISSN: 03605442. DOI: `10.1016/j.energy.2014.03.032`.

[6] T. H. Ahmed. *Reservoir Engineering Handbook, 4th edition*. Elsevier Inc., 2010, pp. 10–12. ISBN: 9780120885480.

[7] N. N. Akinfiev and L. W. Diamond. "Thermodynamic description of aqueous nonelectrolytes at infinite dilution over a wide range of state parameters". In: *Geochimica et Cosmochimica Acta* 67.4 (2003), pp. 613–629. ISSN: 00167037. DOI: `10.1016/S0016-7037(02)01141-9`.

[8] K. Albert et al. "Thermal conductivity estimation model considering the effect of water saturation explaining the heterogeneity of rock thermal conductivity". In: *Geothermics* 66.March (2017), pp. 1–12. ISSN: 03756505. DOI: `10.1016/j.geothermics.2016.11.006`.

[9] A. A. Aleksandrov, V. F. Ochkov, and K. A. Orlov. "Equations and computer program for calculating the properties of gases and combustion products". In: *Thermal Engineering* 52.3 (2005), pp. 221–229. ISSN: 00406015.

[10] A. A. Amooey. "A simple correlation to predict thermal conductivity of supercritical carbon dioxide". In: *Journal of Supercritical Fluids* 86 (2014), pp. 1–3. ISSN: 08968446. DOI: `10.1016/j.supflu.2013.11.016`.

[11] R. J. Arts et al. "The feasibility of CO2 storage in the depleted P18-4 gas field offshore the Netherlands (the ROAD project)". In: *International Journal of Greenhouse Gas Control* 11.SUPPL (2012), pp. 10–20. ISSN: 17505836. DOI: `10.1016/j.ijggc.2012.09.010`.

[12] A. Battistelli and M. Marcolini. "TMGAS: A new TOUGH2 EOS module for the numerical simulation of gas mixtures injection in geological structures". In: *International Journal of Greenhouse Gas Control* 3.4 (2009), pp. 481–493. ISSN: 17505836. DOI: `10.1016/j.ijggc.2008.12.002`.

[13] M. Batzle and Z. Wang. "Seismic properties of pore fluids". In: *Geophysics* 57.11 (1992), pp. 1396–1408. ISSN: 00168033. DOI: `10.1190/1.1443207`.

[14] E. Békési et al. "An updated geothermal model of the Dutch subsurface based on inversion of temperature data". In: *Geothermics* 88.June 2020 (2020), p. 101880. ISSN: 03756505. DOI: `10.1016/j.geothermics.2020.101880`.

[15] J. M. Bielicki. *Don ' t Emit , Use It : CO 2 -Enabled Geothermal Energy Production and Storage Intergovernmental Panel on*. 2019. URL: `https://www.catf.us/wp-content/uploads/2019/06/Don%E2%80%99t-Emit-Use-It-CO2-Enabled-Geothermal-Energy-Production-and-Storage.pdf`.

[16] T de Boer, J.A. Steijn, and J Mao. *Carbon Capture and Storage in the Port of Rotterdam*. Tech. rep. Delft University of Technology, 2020.

[17] F. Brigaud and G. Vasseur. "Mineralogy, porosity and fluid control on thermal conductivity of sedimentary rocks". In: *Geophysical Journal International* 98.3 (1989), pp. 525–542. ISSN: 1365246X. DOI: `10.1111/j.1365-246X.1989.tb02287.x`.

[18] R. H. Brooks and A. T. Corey. "Hydraulic Properties of Porous Media". In: *Hydrology Papers* 3 (1964). ISSN: 00319090.

[19] S. Brunsting et al. "Stakeholder participation practices and onshore CCS: Lessons from the Dutch CCS case Barendrecht". In: *Energy Procedia* 4 (2011), pp. 6376–6383. ISSN: 18766102. DOI: `10.1016/j.egypro.2011.02.655`.

[20] N. L. Carr, R. Kobayashi, and D. B. Burrows. "Viscosity of Hydrocarbon Gases Under Pressure". In: *Journal of Petroleum Technology* 6.10 (1954), pp. 47–55. ISSN: 0149-2136. DOI: `10.2118/297-g`.

[21] CBS. *Uitstoot Broeikasgassen 8 procent lager in 2020*. URL: `https://www.cbs.nl/nl-nl/nieuws/2021/10/uitstoot-broeikasgassen-8-procent-lager-in-2020`.

[22] K. Chen, R. C. Winter, and M. K. Bergman. "Carbon dioxide from fossil fuels: Adapting to uncertainty". In: *Energy Policy* 8.4 (1980), pp. 318–330. ISSN: 03014215. DOI: `10.1016/0301-4215(80)90108-1`.

[23] I. S. Cole et al. "Corrosion of pipelines used for CO 2 transport in CCS: Is it a real problem?" In: *International Journal of Greenhouse Gas Control* 5.4 (2011), pp. 749–756. ISSN: 17505836. DOI: `10.1016/j.ijggc.2011.05.010`.

[24] M.C.M. Creusen. "Near wellbore effects induced by CO2 injection and the influence on injecticity in depleted gas reservoirs". PhD thesis. Delft University of Technology, 2018, pp. 1–107.

[25] R. A. Crooijmans et al. "The influence of facies heterogeneity on the doublet performance in low-enthalpy geothermal sedimentary reservoirs". In: *Geothermics* 64 (2016), pp. 209–219. ISSN: 03756505. DOI: `10.1016/j.geothermics.2016.06.004`.

[26] Z. Duan and R. Sun. "An improved model calculating CO 2 solubility in pure water and aqueous NaCl solutions from 273 to 533 K and from 0 to 2000 bar". In: *Chemical Geology* 193.3-4 (2003), pp. 257–271. ISSN: 00092541. DOI: `10.1016/S0009-2541(02)00263-2`.

[27] EBN and Gasunie. *Transport en opslag van CO2 in Nederland*. Tech. rep. 2017, pp. 1–87.

[28] J. Ezekiel et al. "Combining natural gas recovery and CO2-based geothermal energy extraction for electric power generation". In: *Applied Energy* 269.April 2020 (2020), p. 115012. ISSN: 03062619. DOI: `10.1016/j.apenergy.2020.115012`.

[29] Nagasree Garapati et al. "CO2-plume geothermal (CPG) heat extraction in multi-layered geologic reservoirs". In: *Energy Procedia* 63.December (2014), pp. 7631–7643. ISSN: 18766102. DOI: `10.1016/j.egypro.2014.11.797`.

[30] J. E Garcia. *Density of Aqueous Solutions of CO2*. Tech. rep. Lawrence Berkeley National Laboratory, 2001.

[31] Global CCS Institute. *Geological CO2 Storage Factsheet*. 2021.

[32] Y. Guo et al. "An enthalpy model of CO2-CH4-H2S-N2-brine systems applied in simulation of non-isothermal multiphase and multicomponent flow with high pressure, temperature and salinity". In: *Journal of CO2 Utilization* 31.February (2019), pp. 85–97. ISSN: 22129820. DOI: `10.1016/j.jcou.2019.02.018`.

[33] J. Hansper et al. "ASSESSMENT OF PERFORMANCE AND COSTS OF CO2 PLUME GEOTHERMAL (CPG) SYSTEMS". In: *European Geothermal Congress*. June. Den Haag, 2019.

[34] E. Heidaryan, J. Moghadasi, and A. Salarabadi. "A new and reliable model for predicting methane viscosity at high pressures and high temperatures". In: *Journal of Natural Gas Chemistry* 19.5 (2010), pp. 552–556. ISSN: 10039953. DOI: `10.1016/S1003-9953(09)60109-2`.

[35] E. Heidaryan et al. "Viscosity of pure carbon dioxide at supercritical region: Measurement and correlation approach". In: *Journal of Supercritical Fluids* 56.2 (2011), pp. 144–151. ISSN: 08968446. DOI: `10.1016/j.supflu.2010.12.006`.

[36] J. Hekayati, A. Roosta, and J. Javanmardi. "Volumetric properties of supercritical carbon dioxide from volume-translated and modified Peng-Robinson equations of state". In: *Korean Journal of Chemical Engineering* 33.11 (2016), pp. 3231–3244. ISSN: 02561115. DOI: `10.1007/s11814-016-0176-5`.

[37] S. de Hoop. "Determination of Relevant Spatial Scale in Reservoir Simulation". PhD thesis. Delft University of Technology, 2017.

[38] IPCC. *Global warming of 1.5°C: An IPCC Special Report on the impacts of global warming of 1.5°C above pre-industrial levels and related global greenhouse gas emission pathways, in the context of strengthening the global response to the threat of climate change*. Tech. rep. October. 2018.

[39] A. W. Islam and E. S. Carlson. "Viscosity models and effects of dissolved CO2". In: *Transactions - Geothermal Resources Council* 36 (2012), pp. 1269–1274. ISSN: 01935933.

[40] J. de Jager et al. "Geology of Gas and Oil under the Netherlands". In: *Geology of Gas and Oil under the Netherlands* December (1996). DOI: `10.1007/978-94-009-0121-6`.

[41] M. D. Jensen et al. *Opportunities and Challenges Associated with CO2 Compression and Transportation During CCS Activities*. Tech. rep. Plains CO2 Reduction Partnership Phase III. National Energy Technology Laboratory, 2011, p. 42.

[42] B. Kabdenova, L. R. Rojas-Solórzano, and E. Monaco. "Lattice Boltzmann simulation of near/supercritical CO2 flow featuring a crossover formulation of the equation of state". In: *Computers and Fluids* 216 (2021), pp. 1–14. ISSN: 00457930. DOI: `10.1016/j.compfluid.2020.104820`.

[43] M. Khait and D. Voskov. "Adaptive parameterization for solving of thermal/compositional nonlinear flow and transport with buoyancy". In: *SPE Journal* 23.2 (2018), pp. 522–534. ISSN: 1086055X. DOI: `10.2118/182685-pa`.

[44] L.W. Lake and J.L. Jensen. *A review of Heterogeneiety measures used in reservoir characterization*. 1991, pp. 409–439.

[45] O. Leeuwenburgh et al. "Enhanced gas recovery - A potential 'U' for CCUS in the netherlands". In: *Energy Procedia* 63 (2014), pp. 7809–7820. issn: 18766102. doi: `10.1016/j.egypro.2014.11.815`.

[46] P. J. Linstrom and W. G. Mallard. "NIST Chemistry webBook, NIST Standard Reference Database Number 69". In: *National Institute of Standards and Technology* (2014). issn: 0009-4978.

[47] X. Lyu, M. Khait, and D. Voskov. "Operator-Based Linearization Approach for Modeling of Multiphase Flow with Buoyancy and Capillarity". In: *SPE Journal* 26.04 (Aug. 2021), pp. 1858–1875. issn: 1086-055X. doi: `10.2118/205378-PA`.

[48] X. Lyu, D. Voskov, and W. R. Rossen. "Numerical investigations of foam-assisted CO2 storage in saline aquifers". In: *International Journal of Greenhouse Gas Control* 108.February (2021), p. 103314. issn: 17505836. doi: `10.1016/j.ijggc.2021.103314`.

[49] H. Mao et al. "Development and application of ultra-high temperature drilling fluids in offshore oilfield around bohai sea bay Basin, China". In: *Offshore Technology Conference Asia 2016, OTCA 2016* March (2016), pp. 1201–1222. doi: `10.4043/26384-ms`.

[50] M. McBride-Wright. "Viscosity and Density of Aqueous Fluids with Dissolved CO2". PhD thesis. Imperial College London, 2014.

[51] B. Metz et al. *IPCC Special Report on Carbon Dioxide Capture an*. Tech. rep. Integovernmental Panel on Climate Change, 2005. doi: `10.1002/9783527818488.ch15`.

[52] E. E. Michalides. "Thermodynamic Properties of Geothermal Fluids". In: *Geothermal resources council* Transactio.1 (1981), pp. 361–364. issn: 00167029.

[53] N. W. Morshuis. "An improved carbon-dioxide thermodynamic model applied for reservoir simulation". PhD thesis. Delft University of Technology, 2019.

[54] NAM B.V. *Petrophysical Evaluation of the KNNSL and KNGLG reservoirs in MNZ-1*. Tech. rep. 2014, pp. 1–15.

[55] M. Norton. *Depositional Environments and Sedimentary Basins*. url: `https://opentextbc.ca/geology/chapter/6-3-depositional-environments-and-sedimentary-basins/`.

[56] C. M. Oldenburg. "Carbon Sequestration in natural Gas Reservoirs: Enhanced Gas Recovery and natural Gas Storage". In: *TOUGH Symposium 2003* (2003), pp. 1–8.

[57] B. Orlic. "Geomechanical effects of CO2 storage in depleted gas reservoirs in the Netherlands: Inferences from feasibility studies and comparison with aquifer storage". In: *Journal of Rock Mechanics and Geotechnical Engineering* 8.6 (2016), pp. 846–859. issn: 16747755. doi: `10.1016/j.jrmge.2016.07.003`.

[58] A. Péneloux, E. Rauzy, and R. Fréze. "A consistent correction for Redlich-Kwong-Soave volumes". In: *Fluid Phase Equilibria* 8.1 (1982), pp. 7–23. issn: 03783812. doi: `10.1016/0378-3812(82)80002-2`.

[59] D. Y. Peng and D. B. Robinson. "A New Two-Constant Equation of State". In: *Industrial and Engineering Chemistry Fundamentals* 15.1 (1976), pp. 59–64. issn: 01964313. doi: `10.1021/i160057a011`.

[60] J. B. Randolph and M. O. Saar. "Coupling carbon dioxide sequestration with geothermal energy capture in naturally permeable, porous geologic formations: Implications for CO2 sequestration". In: *Energy Procedia* 4 (2011), pp. 2206–2213. issn: 18766102. doi: `10.1016/j.egypro.2011.02.108`.

[61] Jimmy B. Randolph et al. "Wellbore heat transfer in CO2-based geothermal systems". In: *Transactions - Geothermal Resources Council* 36 1 (2012), pp. 549–554. issn: 01935933.

[62] A. Read et al. “Lessons from the ROAD project for future deployment of CCS”. In: *International Journal of Greenhouse Gas Control* 91.October 2019 (2019), p. 102834. ISSN: 17505836. DOI: `10.1016/j.ijggc.2019.102834`.

[63] O. Redlich and J. N. S. Kwong. *On the thermodynamics of solutions. An equation of state. Fugacities of Gaseous Solutions*. Tech. rep. Shell Development Company, 1949. DOI: `10.1021/cr60137a013`.

[64] D. Roizard. “Antoine Equation”. In: *Encyclopedia of Membranes*. 2. 2014, pp. 1–3. ISBN: 9783642408724. DOI: `10.1007/978-3-642-40872-4`.

[65] Rotterdam CCUS project Porthos. *Rotterdam CCUS*. 2020. URL: `https://rotterdamccus.nl/stand-van-zaken-rotterdam-ccus-project-porthos/`.

[66] M. H. Sharqawy. “New correlations for seawater and pure water thermal conductivity at different temperatures and salinities”. In: *Desalination* 313 (2013), pp. 97–104. ISSN: 00119164. DOI: `10.1016/j.desal.2012.12.010`.

[67] V. Sisinni et al. “Facies modeling described by probabilistic patterns using Multi-point statistics an application to the K-field, Libya”. In: 42045 (2016), pp. 229–229. DOI: `10.1190/ice2016-6320106.1`.

[68] G. Soave. “Equilibrium constants from a modified Redlich-Kwong equation of state”. In: *Chemical Engineering Science* (1972). ISSN: 00092509. DOI: `10.1016/0009-2509(72)80096-4`.

[69] J. P. Spivey, W. D. McCain, and R. North. “Estimating density, formation volume factor, compressibility, methane solubility, and viscosity for oilfield brines at temperatures from 0 to 275° C, pressures to 200 MPa, and salinities to 5.7 mole/kg”. In: *Journal of Canadian Petroleum Technology* 43.7 (2004), pp. 52–61. ISSN: 00219487. DOI: `10.2118/04-07-05`.

[70] N. Spycher and K. Pruess. “CO2-H2O mixtures in the geological sequestration of CO2. II. Partitioning in chloride brines at 12-100°C and up to 600 bar”. In: *Geochimica et Cosmochimica Acta* 69.13 (2005), pp. 3309–3320. ISSN: 00167037. DOI: `10.1016/j.gca.2005.01.015`.

[71] United Nations. *Paris Agreement*. 2015. DOI: `10.4324/9789276082569-2`.

[72] F. F. N. Van Hulten. “Geological factors effecting compartmentalization of Rotliegend gas fields in the Netherlands”. In: *Geological Society Special Publication* 347.November 2010 (2010), pp. 301–315. ISSN: 03058719. DOI: `10.1144/SP347.17`.

[73] D. Voskov. “Operator-based linearization approach for modeling of multiphase multi-component flow in porous media”. In: *Journal of Computational Physics* 337 (2017), pp. 275–288. ISSN: 10902716. DOI: `10.1016/j.jcp.2017.02.041`.

[74] D. Voskov, R. Zaydullin, and A. Lucia. “Heavy oil recovery efficiency using SAGD, SAGD with propane co-injection and STRIP-SAGD”. In: *Computers and Chemical Engineering* 88 (2016), pp. 115–125. ISSN: 00981354. DOI: `10.1016/j.compchemeng.2016.02.010`.

[75] D. Voskov et al. *Delft Advanced Research Terra Simulator*. Tech. rep. 2021, pp. 1–9.

[76] Y. Wang et al. “An efficient numerical simulator for geothermal simulation: A benchmark study”. In: *Applied Energy* 264.October 2019 (2020). ISSN: 03062619. DOI: `10.1016/j.apenergy.2020.114693`.

[77] Y. Wang et al. “Multiphase mass and heat transfer in fractured high-enthalpy geothermal systems”. In: (2020).

[78] Y. Wang et al. "Uncertainty Quantification of Realistic Geothermal Reservoir". In: *Proceedings World Geothermal Congress*. October. 2021, pp. 1–5. DOI: `10.3997/2214-4609.202021080`.

[79] C. J. L. Willems and H. M. Nick. "Towards optimisation of geothermal heat recovery: An example from the West Netherlands Basin". In: *Applied Energy* 247.December 2018 (2019), pp. 582–593. ISSN: 03062619. DOI: `10.1016/j.apenergy.2019.04.083`.

[80] T. Xu et al. "On fluid and thermal dynamics in a heterogeneous CO2 plume geothermal reservoir". In: *Geofluids* 2017 (2017), p. 12. ISSN: 14688123. DOI: `10.1155/2017/9692517`.

[81] W. Zhong and J. D. Haigh. "The greenhouse effect and carbon dioxide". In: *Weather* 68.4 (2013), pp. 100–105. ISSN: 00431656. DOI: `10.1002/wea.2072`.

[82] Z. ZiabakhshGanji. "Physical and geochemical impacts of impure CO2 on storage in depleted hydrocarbon reservoirs and saline aquifers". PhD thesis. VU Amsterdam, 2015.

Acronyms

CCS Carbon Capture and Storage

CPG Carbon-Dioxide Plume Geothermal

ROAD Rotterdam Opslag en Afvang Demonstratieproject

scCO2 Supercritical Carbon Dioxide

EGR Enhanced Gas Recovery

DARTS Delft Advanced Research Terra Simulator

CNGR Conventional Natural Gas Recovery

N/G Net-to-Gross ratio

GWC Gas-Water Contact

SIS Sequential Indicator Simulation

PRN Pernis field

WNB West Netherlands Basin

RTD Rotterdam field

PRW-06 Pernis-West well 06

EEM-01 Eemshaven well 01

GR Gamma Ray

SP Spontaneous Potential

HAGWC Height above Gas-Water contact

AqP Aqueous Phase

NAqP Non-Aqueous Phase

MBE Mass Balance Equation

ECE Energy Conservation Equation

OBL Operator Based Linearization

PPU	Phase-potential-upwinding
EOS	Equation of State
RF	Recovery Factor
BHP	Bottom Hole Pressure
NPV	Net Present Value
MNZ	Monster field

Appendix A

Supplemental Model information

This chapter contains reference data for the dynamic model, mostly consisting of tabular data used in the various equations specified in chapter 3.

A.1 Supplemental information to the Thermodynamic Model

Table A.1: Table showing the constants used for determination of k_h used in Equation 3.32

Gas	η	τ	β	Γ
CO_2	-0.114535	-5.279063	6.187967	0
H_2 S	0.77357854	0.27049433	0.27543436	0
SO_2	0.198907	-1.552047	2.242564	-0.009847
N_2	-0.008194	-5.175337	6.906469	0
CH_4	-0.092248	-5.779280	7.262730	0
O_2	0.290812	-1.862778	3.9917226	0

Table A.2: Second order interaction coefficients used in Equation 3.33

constant	λ_{CO_2-Na}	λ_{SO_2-Na}	λ_{N_2-Na}	λ_{H_2S-Na}	λ_{CH_4-Na}	λ_{O_2-Na}
c_1	-0.0653	$-5.0962\text{E}-2$	-2.0934	1.0366	$-5.707\text{E}-1$	0.20
c_2	$1.6791\text{E}-4$	$2.8865\text{E}-4$	$3.1445\text{E}-3$	$-1.1785\text{E}-3$	$7.300\text{E}-4$	0
c_3	40.839	0	$3.9139\text{E}+2$	$-1.7755\text{E}+2$	$1.5177\text{E}+2$	0
c_4	0	0	$-2.9974\text{E}-7$	$-4.5313\text{E}-4$	$3.1927\text{E}-5$	0
c_5	0	$1.1145\text{E}-2$	0	0	0	0
c_6	$-3.9267\text{E}-2$	0	$-1.5918\text{E}-5$	0	$-1.6427\text{E}-5$	0
c_7	0	$-2.4878\text{E}-5$	0	0	0	0
c_8	$2.1157\text{E}-2$	0	0	0	0	0
c_9	$6.5486\text{E}-6$	0	0	0	0	0
c_{10}	0	0	0	$4.7751\text{E}+1$	0	0

Table A.3: Third order interaction coefficients used in Equation 3.33

Constant	ζ_{CO_2-Na}	ζ_{SO_2-Na}	ζ_{N_2-Na}	ζ_{H_2S-Na}	ζ_{CH_4-Na}	ζ_{O_2-Na}
c_1	$\frac{-1.}{1446\text{E}-2}$	$-7.146\text{E}-3$	$-6.398\text{E}-3$	-0.01027	$-2.999\text{E}-3$	$-1.28\text{E}-2$
c_2	$2.828\text{E}-5$	0	0	0	0	0
c_3	0	0	0	0	0	0
c_4	0	0	0	0	0	0
c_5	0	0	0	0	0	0
c_6	$1.398\text{E}-2$	0	0	0	0	0
c_7	0	0	0	0	0	0
c_8	$4349\text{E}-2$	0	0	0	0	0
c_9	0	0	0	0	0	0
c_{10}	0	0	0	0	0	0

Table A.4: Binary interaction coefficients between H_2O and Gaseous components used in Equation 3.30

	CO_2	H_2S	SO_2	N_2	CH_4	O_2
H_2O	0.19014	0.105	-1.10329	0.32547	0.47893	0.9

A.2 Supplemental Information to Physical Properties

Appendix to non-aqueous phase properties

Table A.5: Fitting coefficients for CO_2 viscosity computation in Equation 3.47

Coefficient	Tuned coefficient
A_1	$-1.146067 \times 10^{-01}$
A_2	6.978380×10^{-07}
A_3	3.976765×10^{-10}
A_4	6.336120×10^{-02}
A_5	$-1.166119 \times 10^{-02}$
A_6	7.142596×10^{-04}
A_7	6.519333×10^{-06}
A_8	$-3.567559 \times 10^{-01}$
A_9	3.180473×10^{-02}

Table A.6: Fitting coefficients for CH_4 viscosity computation in Equation 3.48

Coefficient	Tuned coefficient
A_1	$-2.25711259 \times 10^{-02}$
A_2	$-1.31338399 \times 10^{-04}$
A_3	$3.44353097 \times 10^{-06}$
A_4	$-4.69476607 \times 10^{-08}$
A_5	$2.23030860 \times 10^{-02}$
A_6	$-5.56421194 \times 10^{-03}$
A_7	$2.90880717 \times 10^{-05}$
A_8	$-1.90511457 \times 10^{+00}$
A_9	$1.14082882 \times 10^{+00}$
A_{10}	$-2.25890087 \times 10^{-01}$

Table A.7: Constants for the determination of ideal gas component enthalpy from [32] and [9] in Equation 3.50

a_i	CH_4	CO_2	H_2O
a_0	-133.833552	-1.818873	31.040960
a_1	-44.338840	12.903022	-39.142208
a_2	214.421009	-9.663486	37.969528
a_3	62.376295	4.225188	-21.837491
a_4	-821.181789	-1.042164	7.422515
a_5	1123.866804	0.126835	-1.381789
a_6	-507.399196	-0.004994	0.108807
a_7	177.100692	2.495024	-12.077118
a_8	-114.066593	-0.827238	3.391051
a_9	44.047253	0.153725	-0.584521
a_{10}	-10.201132	-0.015861	0.058993
a_{11}	1.305622	8.602E-04	-0.003130
a_{12}	-0.071038	-1.922E-05	6.5746E-05
H_{int}	28351.109	2108.207	9908.000

Appendix to Aqueous phase properties

Table A.8: Coefficients for density of brine as function of temperature at 70 MPa for Equation 3.55

i	$D_{C_m,2}(T)$	$D_{C_m,3/2}(T)$	$D_{C_m,1}(\mathrm{T})$	$D_{C_m,1/2}(T)$
1	-7.925×10^{-5}	1.0998×10^{-3}	$-7.6402 \times 10^{-}3$	3.746×10^{-4}
2	-1.93×10^{-6}	-2.8755×10^{-3}	3.6963×10^{-2}	-3.328×10^{-4}
3	-3.4254×10^{-4}	-3.5819×10^{-3}	4.36083×10^{-2}	-3.346×10^{-4}
4	0	-0.72877	-0.333661	0
5	0	1.92016	1.185685	0

Table A.9: Coefficients for different variants of Equation 3.57 and Equation 3.56

i	$D_w(T)$	$E_w(T)$	$F_w(\mathrm{T})$
1	-0.127213	4.221	-11.403
2	0.645486	-3.478	29.932
3	1.03265	6.221	27.952
4	-0.070291	0.5182	0.20684
5	0.639589	-0.4405	0.3768

Table A.10: coefficients used for the computation of $E_{Cm,i}$ and $F_{C_{m,i}}$ in Equation 3.59

i	$E_{C_m}(T)$	$F_{C_m,3/2}(T)$	$F_{C_m,1}(\mathrm{T})$	$F_{C_m,1/2}(T)$
1	0	-1.409	0	-0.1127
2	0	-0.361	5.614	0.2047
3	0.1353	-0.2532	4.6782	-0.0452
4	0	0	-0.307	0
5	0	9.216	2.6069	0

Table A.11: Constants used to compute salt dissolution enthalpy in Equation 3.67

$a_{ij}^{\dagger}$	Value
$\boldsymbol{a}_{00}$	-9633.6
$\boldsymbol{a}_{01}$	-4080.0
$\boldsymbol{a}_{02}$	286.49
$\boldsymbol{a}_{10}$	166.58
$\boldsymbol{a}_{11}$	68.577
$\boldsymbol{a}_{12}$	-4.6856
$\boldsymbol{a}_{20}$	-0.90963
$\boldsymbol{a}_{21}$	-0.36524
$\boldsymbol{a}_{22}$	0.0249667
$\boldsymbol{a}_{30}$	$0.17965\mathrm{E}-02$
$\boldsymbol{a}_{31}$	$0.71924\mathrm{E}-03$
$\boldsymbol{a}_{32}$	$-0.4900\mathrm{E}-04$

Appendix B

Model Validation

In order to correctly show the behaviour of our system in the reservoir, physical properties of the fluid resulting from the computed state need to be characterized. The used correlations are shown in section 3.4 for an overview.

B.1 Validation of component phase partitioning

The first model which need needs to be validated is the Fugacity-Activity model, which governs the component phase partitioning under different conditions. The first check is done by comparing component phase partitioning under a different pressure, temperature and salinity conditions as shown in section B.1. The most important factors to consider here are CO_2 dissolution and H_2O vaporization, as these components can make up a decent fraction of either phase depending on local conditions, compared to CH_4 which strongly favours the gas phase under all conditions within our range of interest.

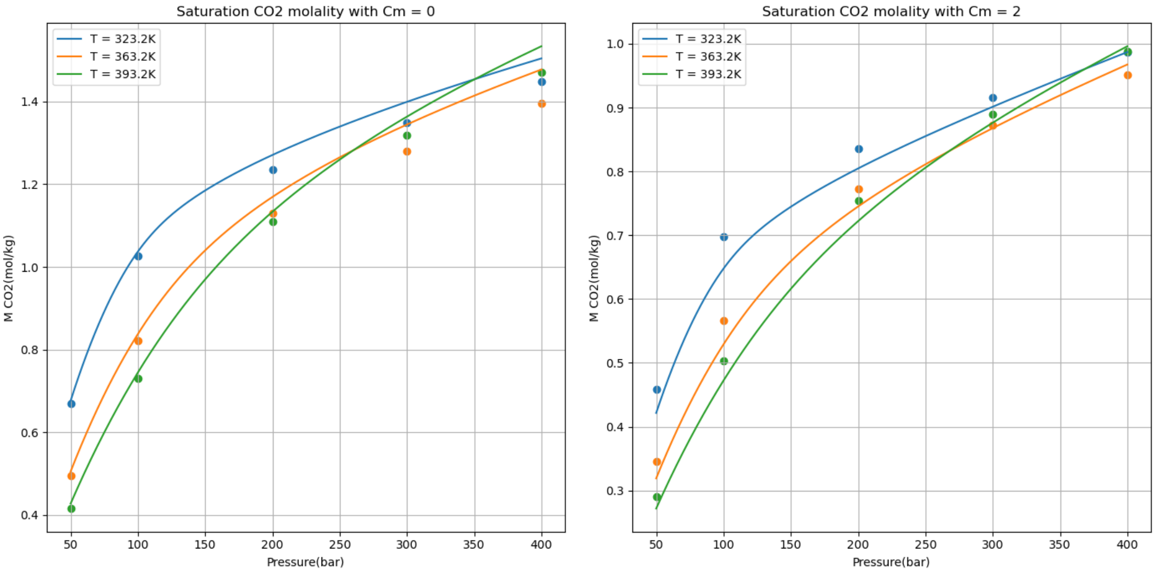

Figure B.1: Graphs showing the saturation molality of CO_2 in water for a range of different temperatures, pressures and salinities compared to experimental data from [26]

It can be seen that the model captures the behaviour of the CO_2 solubility accurately for fresh water and brine systems. It should be noted that for fresh water at high pressures, there appears to be a minor, but significant, overestimation of CO_2 solubility. While this is important to note, the aqueous phase in our model will not have a low molal salinity. Next, the model output is compared to a graph from [82]. Tabular data for this graph could not be found, thus a visual comparison is used and shown in Figure B.1:

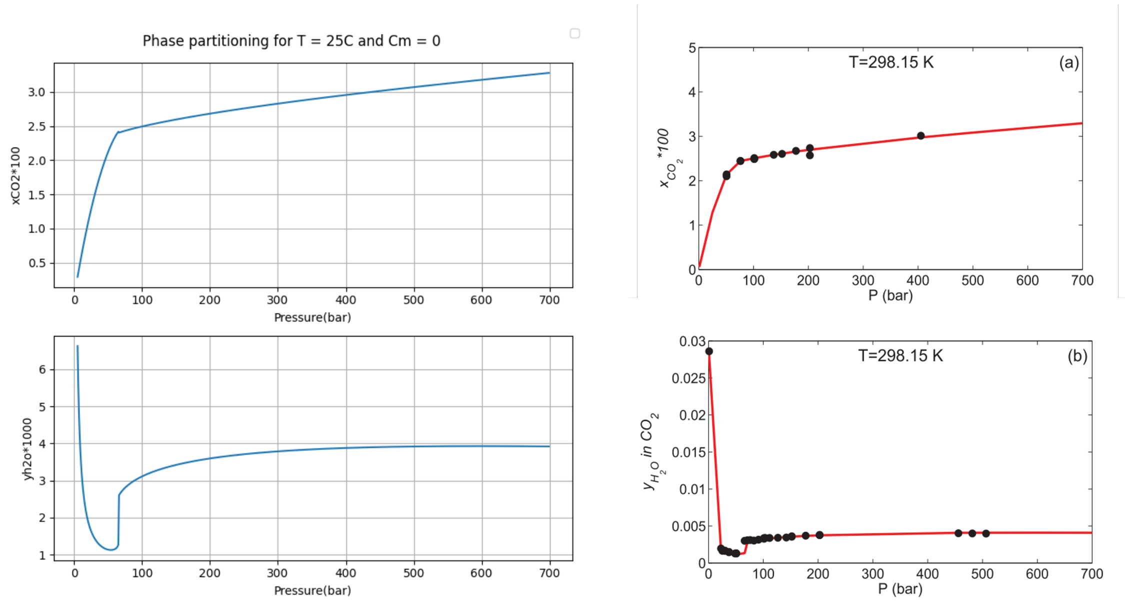

Figure B.2: Graphs showing the saturation molality of CO_2 in water and H_2O in the non-aqueous phase from the used model (left) and a comparative graph from [82] using data from [26]

Evident from the graph is the accordance of the two solubilities at low temperature conditions. The sharp change in water solubility in the non-aqueous phase corresponds to a phase transition in the CO_2 phase from gas to compressible liquid as it passes the cricondenbar.

B.2 Validation of the non-aqueous phase properties

This next chapter discusses the different properties of the non-aqueous phase. It should be noted that the effect of trace H_2O is not considered, except for it's effect on enthalpy due to vaporization.

Density

Gas phase density is shown in Figure B.3, and compared to the grey lines which correspond to the NIST reference database [46]. Good agreement is seen on a range of temperatures and pressures, except for pure CO_2 at medium to low temperatures. This is caused by the use of the Peng-Robinson EOS, which is notoriously inaccurate near the critical point [82]. A simple volume correction by [58] is possible, but it outside the scope of this study. It should also be noted that this effect is most pronounced under around 150 bar, which is at the lower end of our studied range.

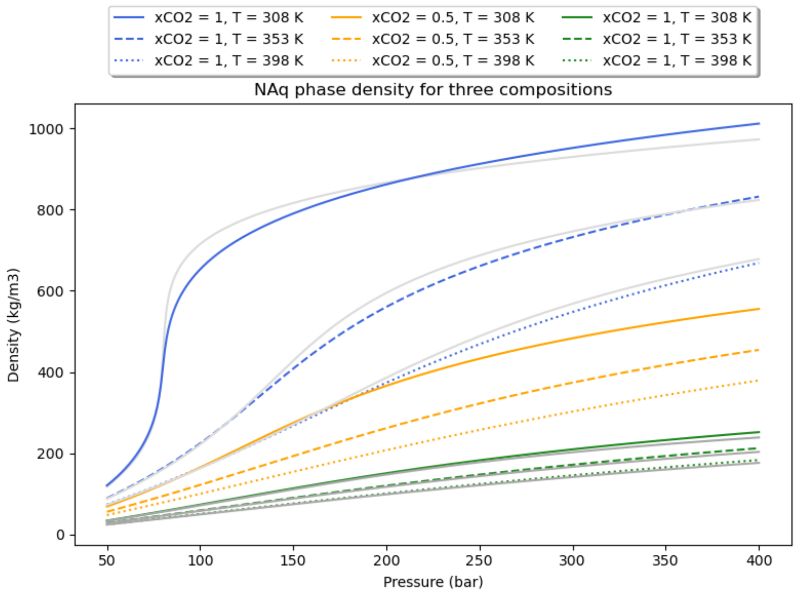

Figure B.3: Non-aqueous phase density for a range of pressures and temperatures at 3 compositions is shown, compared to NIST reference data[46] for the pure components

Viscosity

Figure B.4 shows the NIST reference viscosity of CO_2 (light grey) and CH_4 (dark grey), As well as the viscosities of pure CO_2 and CH_4.

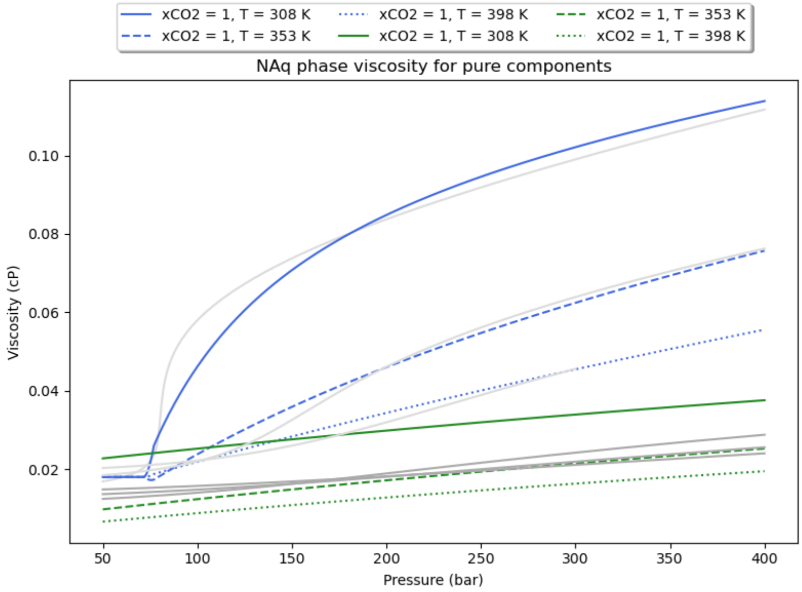

Figure B.4: Non-aqueous phase viscosity for a range of pressures and temperatures for pure components is shown, compared to NIST reference data [46]

The drawback of the simplified equations from Heidaryan et al. [34] [35] becomes obvious here. Due to the simple fit, CO_2 viscosity for low pressure and temperature deviates substantially from the true value. Same as with the density correlation, this model is most accurate for pressures above 150 bar. For simulation cases modelling low pressure CO2-EGR, CO_2

viscosity is manually set at 0.018 Cp. The deviation of the CH_4 viscosity is percentually even greater, especially for low temperatures. However, it should be noted that CH_4 is of less importance for the CPG stage of the system, and that the combination of low temperature CH_4 should not occur in connective parts of the reservoir where the CH_4 will be flushed out before the temperature front advances. In other words, cold CH_4 will be immobile, negating the importance of very accurate viscosity readings.

Enthalpy

One of the most imporant variables in our study is the relative enthalpy function of the non-aqueous phase, which governs the energy of the phase at a certain state [32]. The enthalpy function shown in section B.2 here has been shifted in order to accomodate for the different relative enthalpy integration constants between the used model and the NIST reference dataset. The graph shows excellent agreement with the reference data, indicating accurate simulation of relative enthalpy.

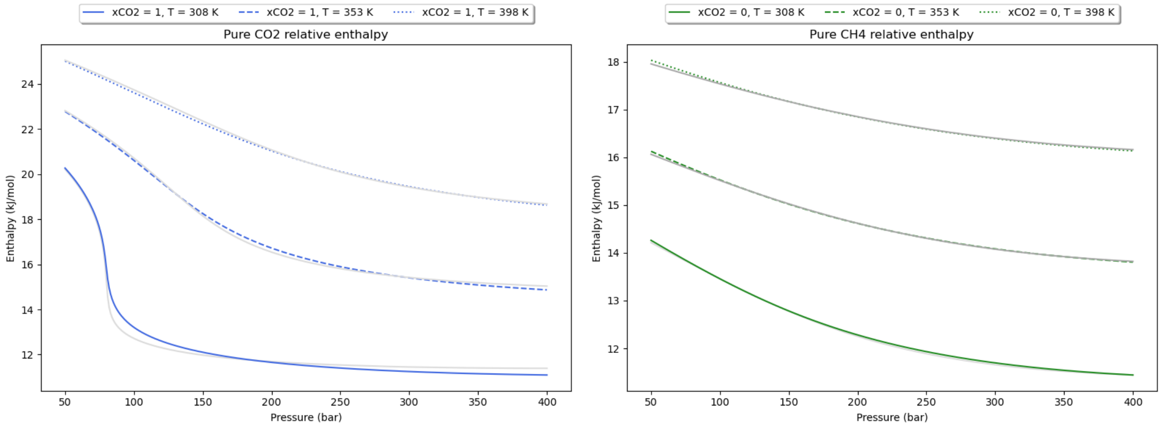

Figure B.5: Pure CO_2 and CH_4 phase relative enthalpies for the non-aqueous phase using [32] and data from [46]

Thermal Conductivity

The final phase property modelled is the phase thermal conductivity using a correlation from Amooey [10]. While gas thermal conductivity is generally quite a bit lower than water or rock conductivity, it might play a role in highly porous reservoirs, or reservoirs where structural trapping of CO_2 occurs. Figure B.6 shows decent agreement between the Amooey correlation and reference data, with larger deviations occuring at low temperature, and around the CO_2 cricondenbar. This means that the empirical correlation lose accuracy around the critical point, where properties are generally harder to predict. Due to the minor importance of non-aqueous phase thermal conductivity, this deviation at extreme conditions is deemed acceptable.

B.3 Validation of the aqueous phase properties

This next chapter discusses the different properties of the aqueous phase. It should be noted that the effect of trace CH_4 is generally not considered, as the solubility of CH_4 is orders of magnitude less than that of CO_2.

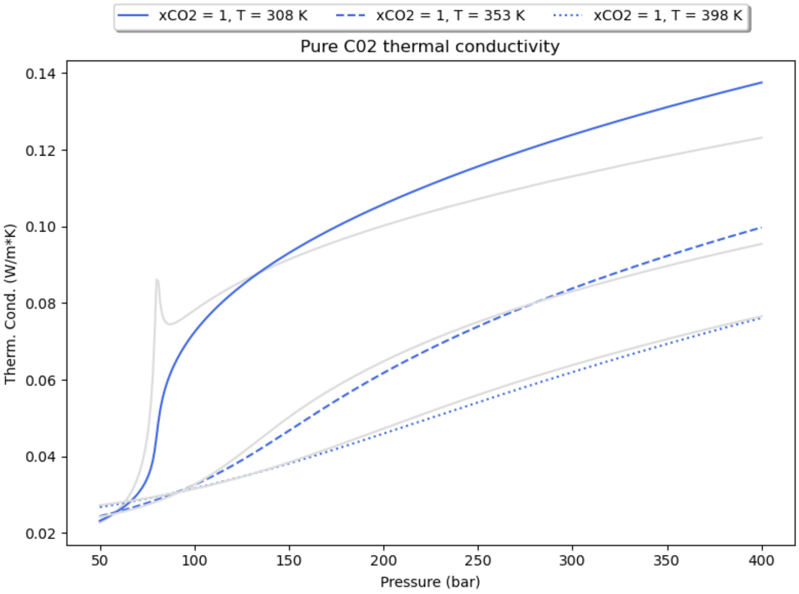

Figure B.6: Non-aqueous phase thermal conductivity for a range of pressures and temperatures for pure CO_2 is shown, compared to NIST reference data [46]

Density

Accurate prediction of density is important for the modelling of mass flux, as well as any buoyancy effects arising from phase density differences. The aqueous phase density model is built from multiple correlations, for pure water density, effect of salinity and effect of dissolved gasses. Figure B.7 shows aqueous phase density without the presence of CO_2 or salt components. The agreement with reference data is very accurate.

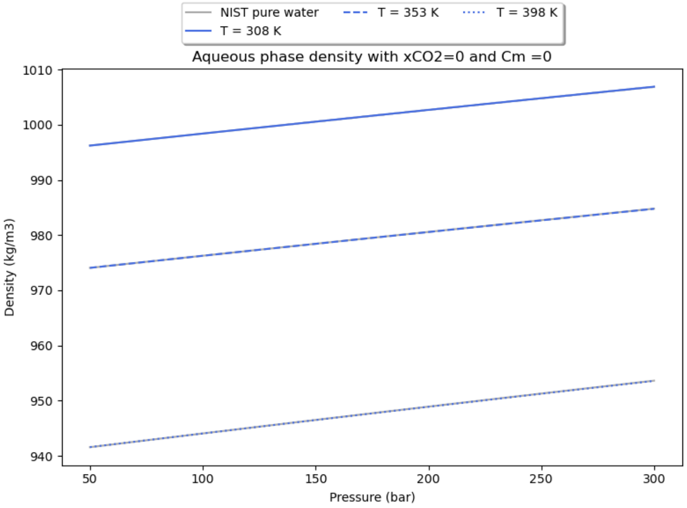

Figure B.7: Aqueous phase density for a range of pressures and temperatures for pure H_2O is shown, compared to NIST reference data [46]

Figure B.8 shows CO_2 saturated brine density for a variety of different temperatures, pressures and salinities. Agreement for all four situations is very close to experimental data. It should be noted that for high temperatures and higher pressures, there appears to be a slight deviation from the experimental data. It should be noted that this deviation could be caused by the deviations in CO_2 solubility shown by section B.1 at higher pressures.

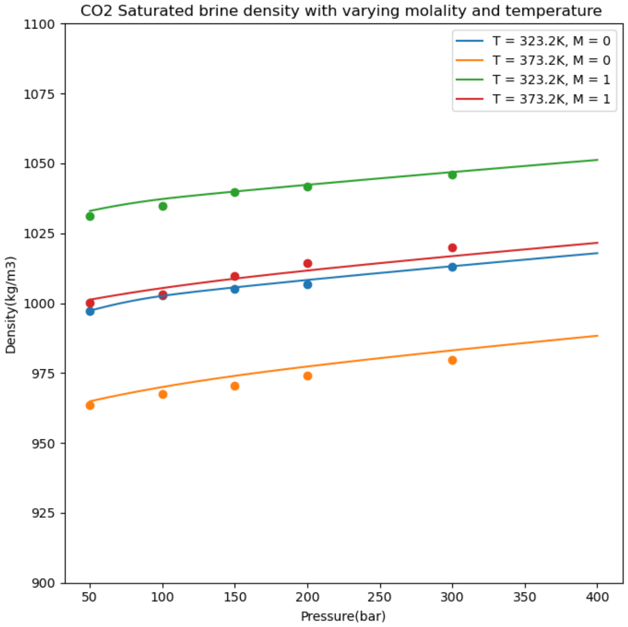

Figure B.8: Aqueous phase density with saturation concentration CO_2 for a range of pressures, temperatures and salinities are shown for pure H_2O is shown with experimental data from [50]

Viscosity

The computation for aqueous phase viscosity is split up into multiple correlations; the viscosity of pure water, and the effect of salt and dissolved CO_2. Figure B.9 shows pure H_2O aqueous phase viscosity compared to NIST reference data, showing excellent agreement over a range of temperatures and pressures.

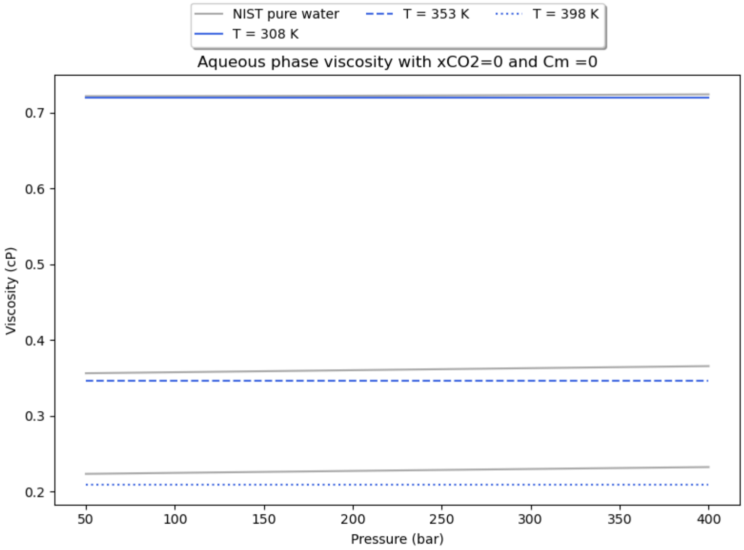

Figure B.9: Aqueous phase viscosity for a range of pressures and temperatures for pure H_2O is shown, compared to NIST reference data [46]

for the effect of salt and CO_2 on viscosity, little experimental data was available, apart from a study from Mcbride-Wright [50] with a wide range of conditions. Data points in the relevant salinity, pressure and temperature range have been extracted and compared on deviation with model data in Table B.10. It can be seen that while the absolute deviation stays within 10%, the data appears to show that the correlation for salinity is not wholly accurate, as becomes clear when comparing the Cm = 0, nonzero x_{CO_2} with the nonzero Cm, $x_{CO_2} = 0$ data. This might indicate that the correlation from Batzle and Wang [13] might not be very accurate, which could be caused by it's age, simplicity and/or the different purpose of the correlation (seismic studies), in which accuracy of models is less important due to the large uncertainty in the data.

Table B.10: Effect of salinity and dissolved CO_2 on aqueous phase viscosity with experimental data from [50]

T	P	Cm	xco2	Viscosity(Cp)		
Kelvin	Bar	mol/kg	-	Experimental	Model	Abs dev.
294.3	151	0	0.009	1.013	0.9934	1.93%
294.3	151	0	0.017	1.0492	1.0274	2.08%
322.93	150	0	0.009	0.5596	0.5704	1.93%
322.91	301	0	0.017	0.5726	0.5901	3.06%
373.13	150	0	0.009	0.2863	0.2803	2.10%
397.98	301	0	0.009	0.2307	0.2173	5.81%
296.18	152.1	0.77	0.0124	1.051	1.0842	3.16%
348.36	302	0.77	0.0124	0.4358	0.4715	8.19%
398.24	302.7	0.77	0.0124	0.2655	0.285	7.34%
296.2	152.2	0.77	0	0.9948	1.0279	3.33%
348.36	152.6	0.77	0	0.4206	0.4533	7.77%
398.26	153.7	0.77	0	0.2611	0.2797	7.12%
274.51	152	2.5	0.0124	2.244	2.0817	7.23%
296.19	300.7	2.5	0.0124	1.2994	1.2954	0.31%

Enthalpy

The enthalpy of the Aqueous phase is calculated through a series of correlations, calculating in steps the enthalpy of pure water, correcting for high pressure, salt dissolution and the dissoltuion of gaseous components. section B.3 Shows the enthalpy of pure ideal H_2O (left) and pressure corrected Aqueous phase enthalpy (right). It can be seen that there is some deviation from the NIST reference database [46], with at high temperature enthalpy being overestimated, and at low temperature enthalpy being underestimated. This divergence indicates an inaccuracy in the model or correlation, as the result is shifted in different directions as opposed to the same direction which would arise from a different relative enthalpy integration constant. The important variable here is not necessarily the absolute enthalpy value, be the relative enthalpy difference between two states, as that indicates the amount of energy that can be extracted by the non-aqueous phase. In this way, the error in enthalpy difference between high temperature and low temperature is reduced due to the absolute deviation being only a small percentage of the total enthalpy change. While this deviation is acceptable for our case, care should be taken when this model is to be used for conventional water based geothermal purposes, as it overestimates the heat capacity of the water.

Next, the model correct for the enthalpy of dissolution of salt. No experimental data in tabular form could be found, so a visual comparison is made with the graph from the validation of the model from Guo [32] in Figure B.3. The model result (left) is in good accordance with the original paper and earlier work as shown right.

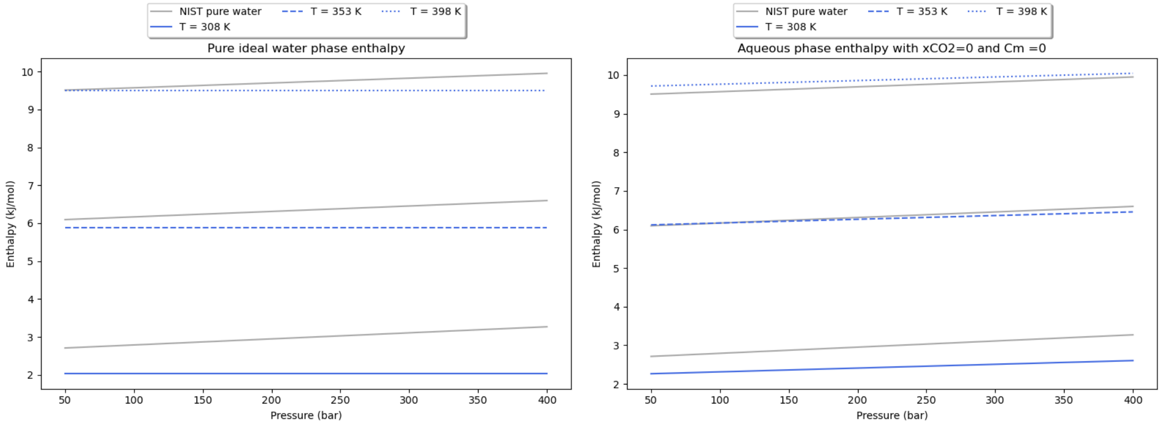

Figure B.11: Pure water enthalpy using correlations from Keenan et al.[32]

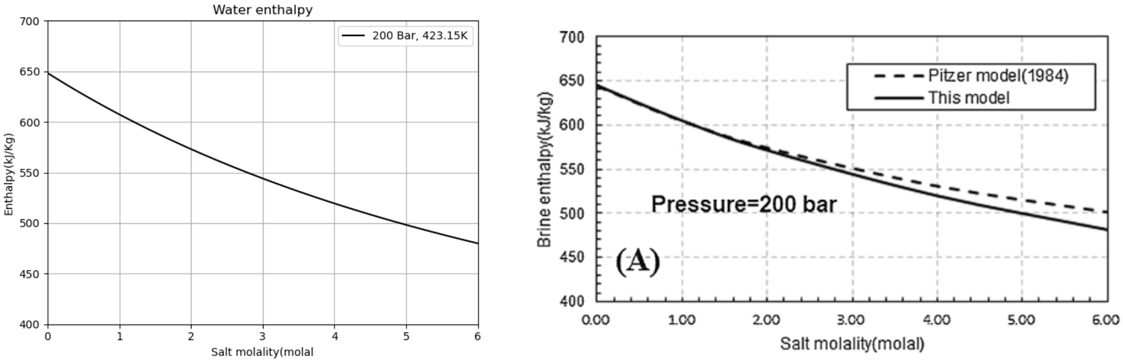

Figure B.12: Effect of salinity on AqP enthalpy, with the validating graph from Guo [32]

Finally, the enthalpy of dissolution of CO_2 is added to the model. Again, a visual comparison is made and shown in Figure B.13, appearing to show good agreement over the range of interest. This value is rather small compared to the total relative enthalpy changes over temperature differences, meaning that this visual check should be sufficient for our required accuracy.

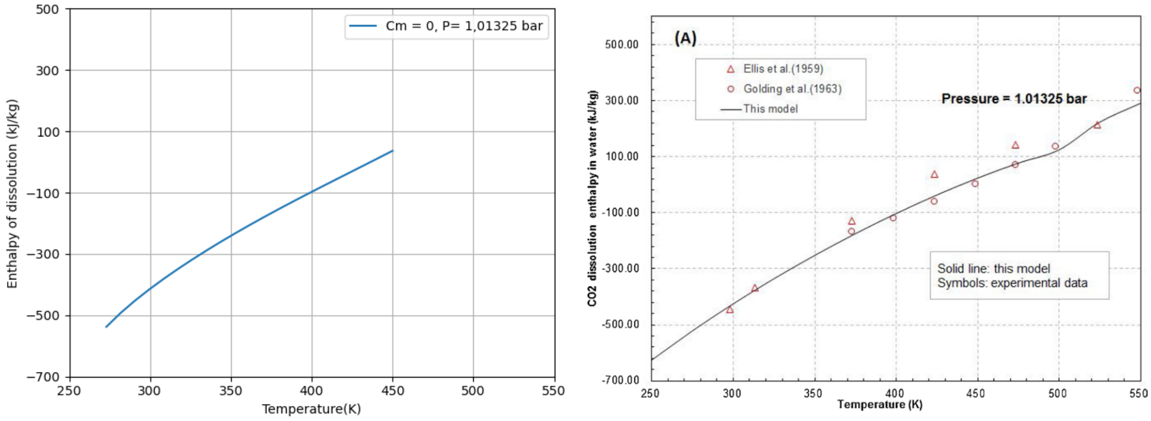

Figure B.13: Graphs comparing the enthalpy of dissolution of CO_2, with the model (left) compared to the validation graph from Guo (right)

Thermal Conductivity

Finally, the adjusted correlation for aqueous phase thermal conductivity from Sharqawy [66] is compared to NIST reference data. Again, fluid phase thermal conductivity is of lesser importance, with the most important being having a value in the correct range. Figure B.14 shows a good agreement with the NIST reference data, and is deemed sufficient to accurately model any effect porous aquifers might have on thermal recharge of the CO_2 plume.

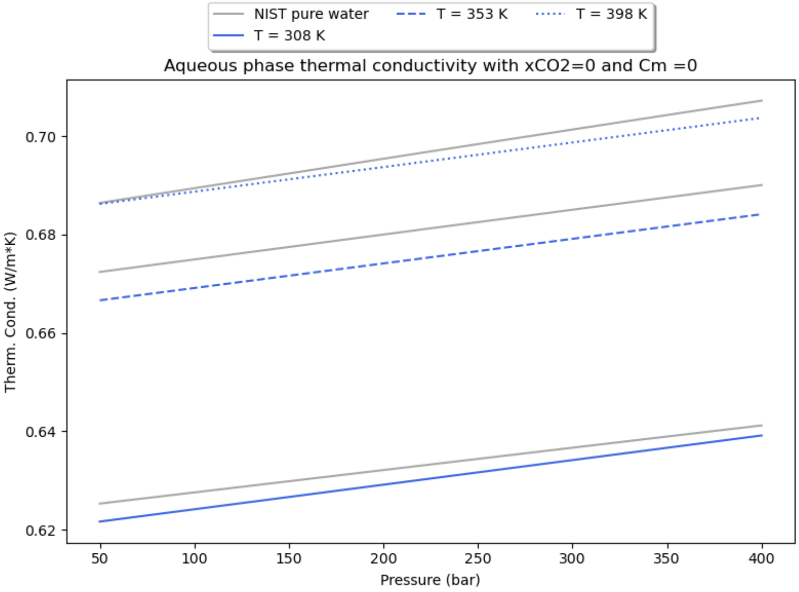

Figure B.14: Aqueous phase thermal conductivity for a range of pressures and temperatures for pure H_2O is shown, compared to NIST reference data [46]

Appendix C

Supplemental Results

C.1 Appendix to 2D Sensitivity Study

C.1.1 Supplemental figures to the Inital State Parameters

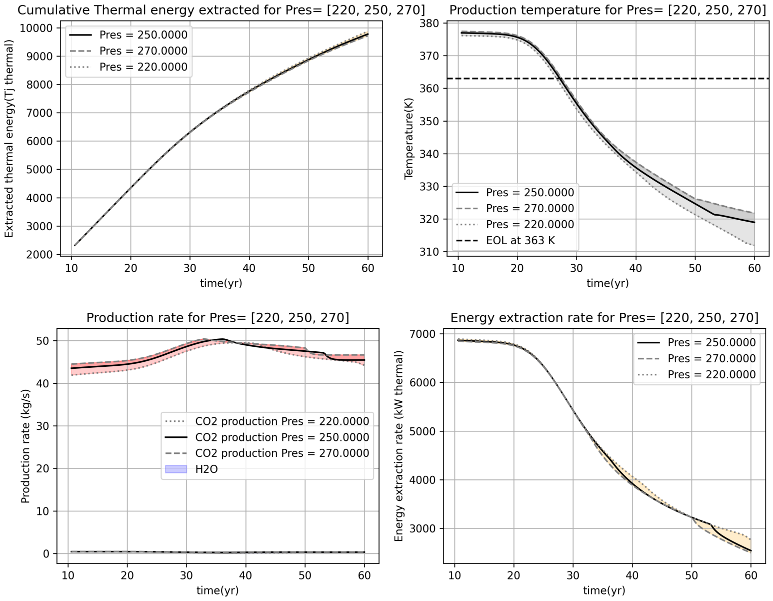

Figure C.1: Production graphs for Reservoir Pressure Sensitivity test

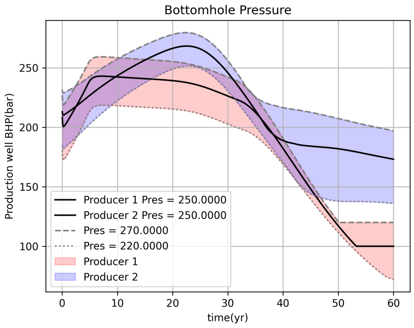

Figure C.2: Production well pressure profiles for the Reservoir Pressure Sensitivity test

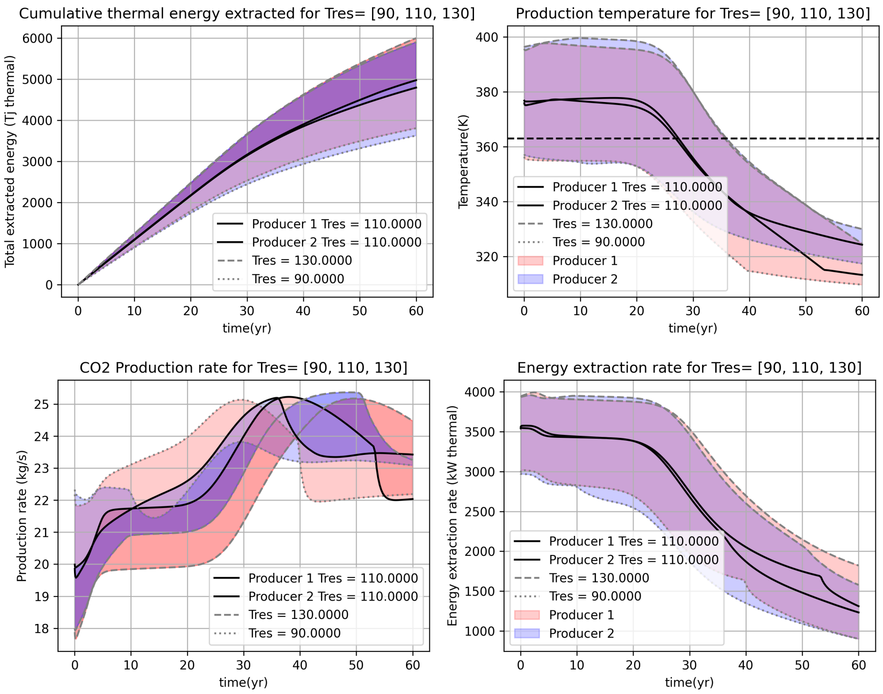

Figure C.3: Production graphs for Reservoir Temperature Sensitivity test per well

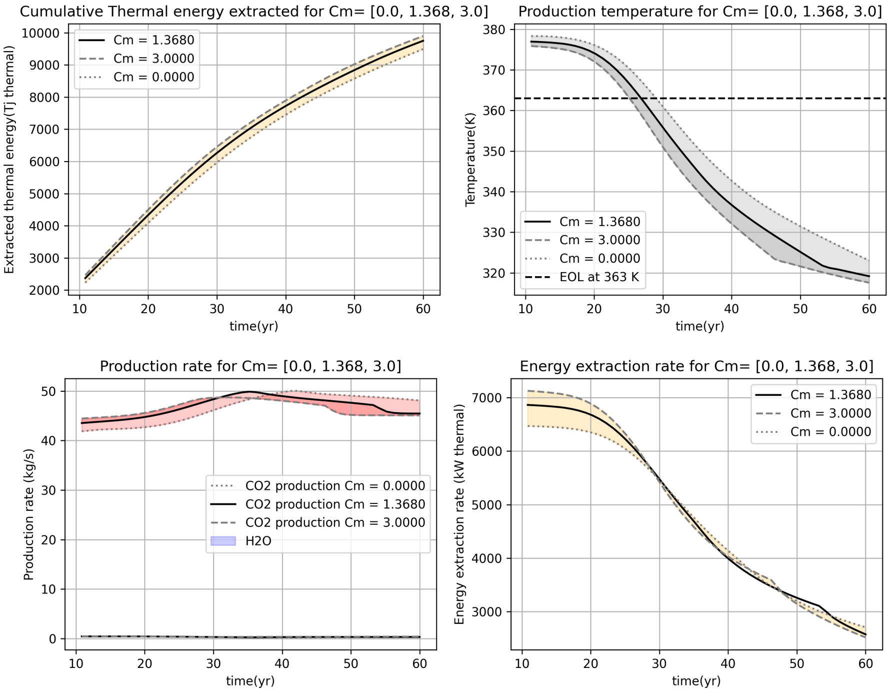

Figure C.4: Production graphs for the Salinity Sensitivity tests

C.1.2 Supplemental Reservoir parameter figures

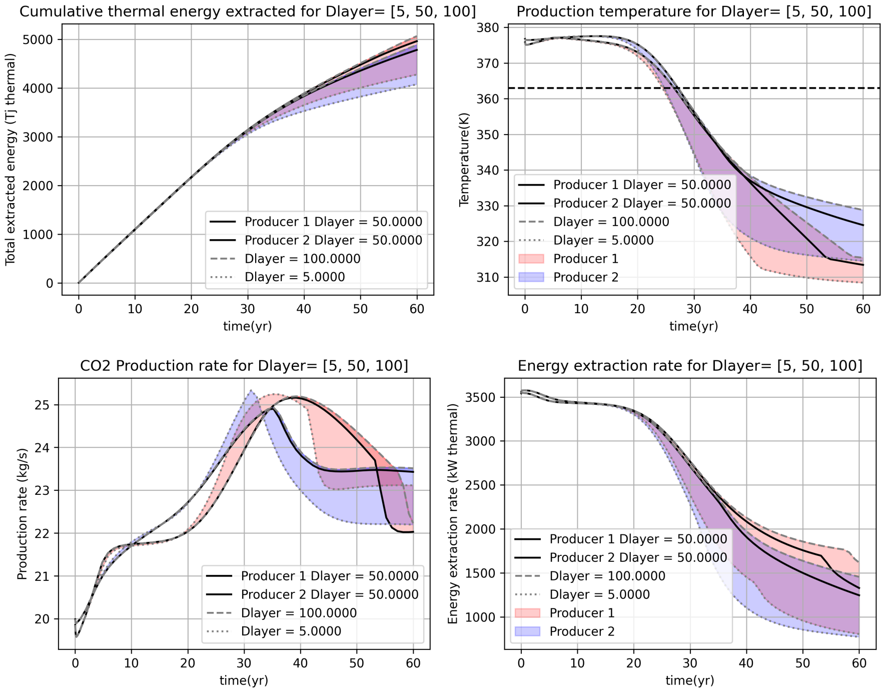

Figure C.5: Production graphs for separating layer thickness test per well

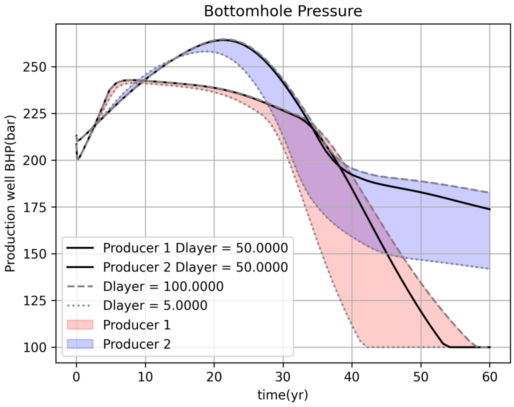

Figure C.6: Pressure profile for the separating layer sensitivity test

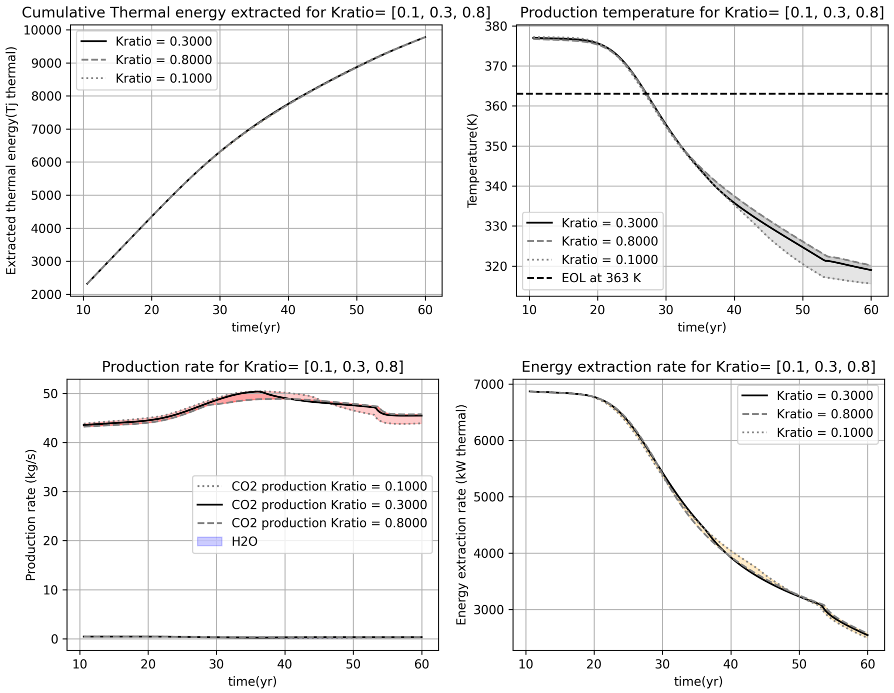

Figure C.7: Production graphs for permeability anisotropy sensitivity test

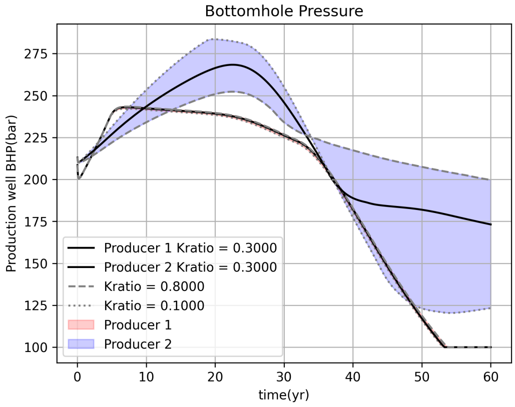

Figure C.8: Production graphs per well for permeability anisotropy sensitivity test

C.1.3 Supplemental Relperm parameter figures

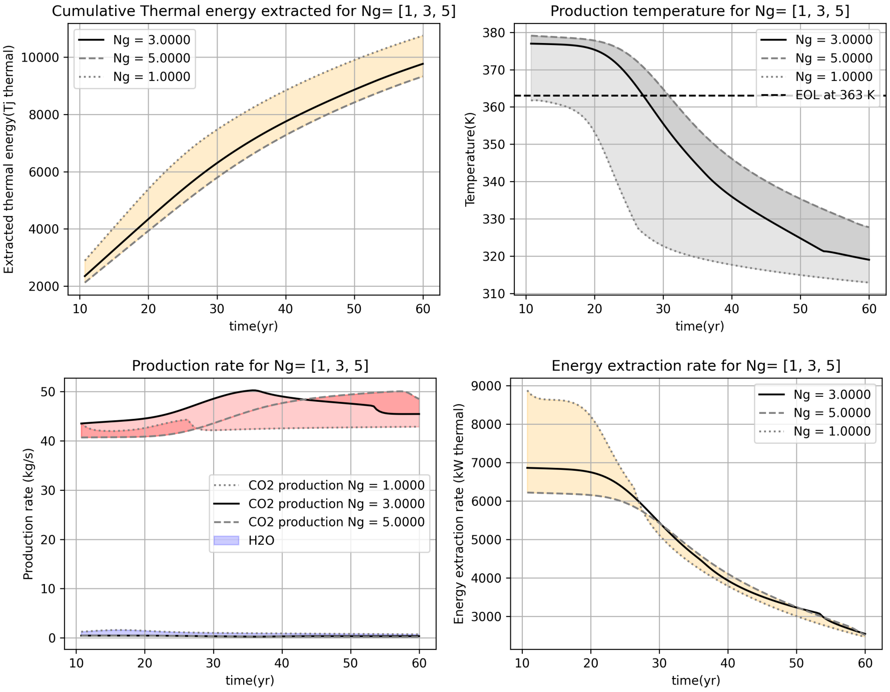

Figure C.9: Production graphs per well for the Brooks-Corey gas exponent sensitivity tests

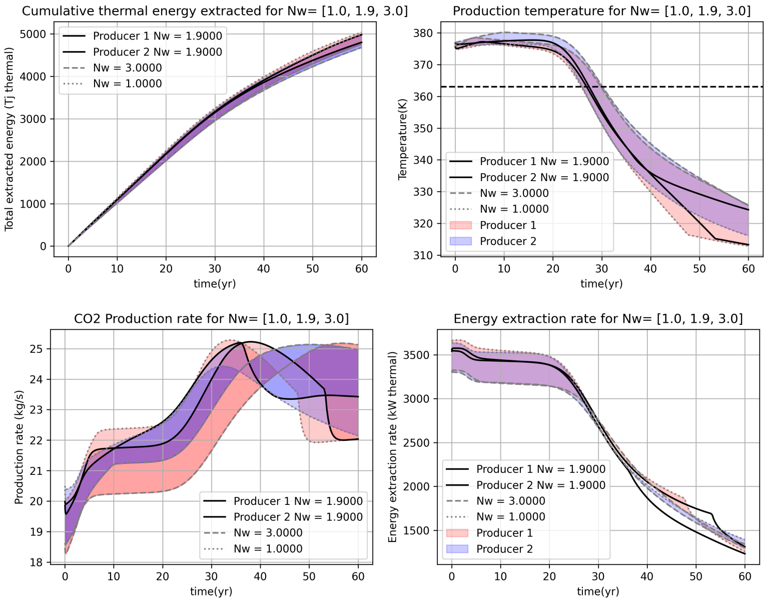

Figure C.10: Production graphs per well for Brooks-Corey water exponent sensitivity test per well

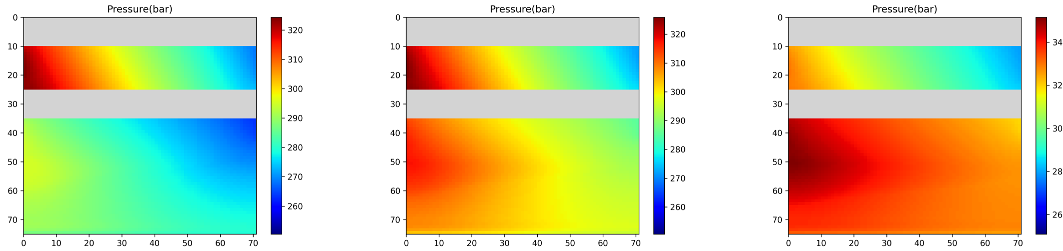

Figure C.11: Brooks-Corey water exponent sensitivity pressure profile after 15 years of CPG. From left to right: low case, base case, high case

C.1.4 Supplemental Thermal Parameter figures

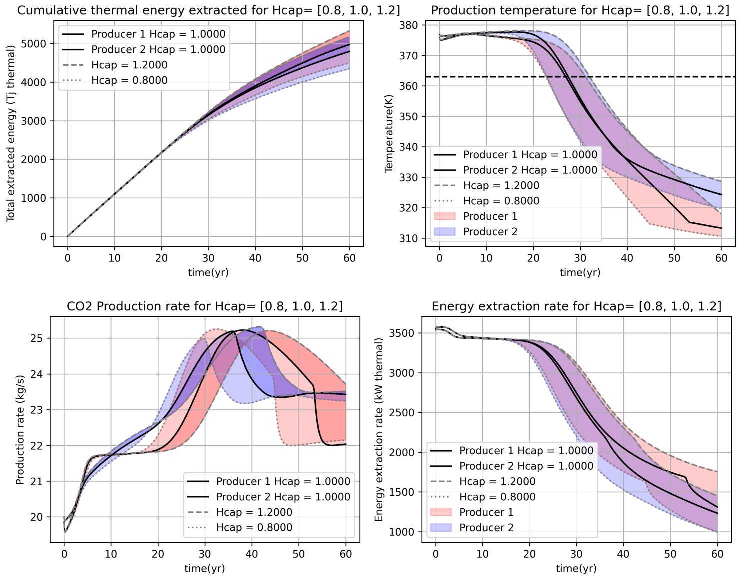

Figure C.12: Production graphs per well for the Heat Capacity sensitivity test

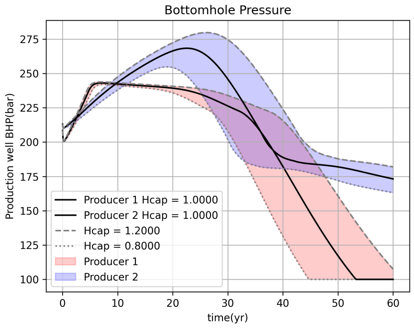

Figure C.13: BHP profile for the Heat Capacity sensitivity test

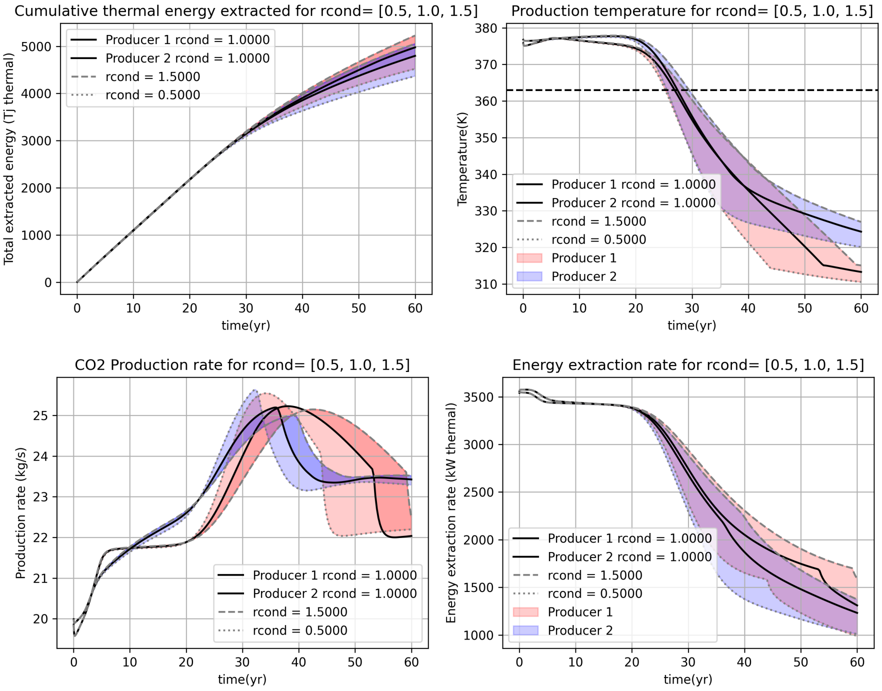

Figure C.14: Production graphs per well for the thermal conductivity sensitivity test

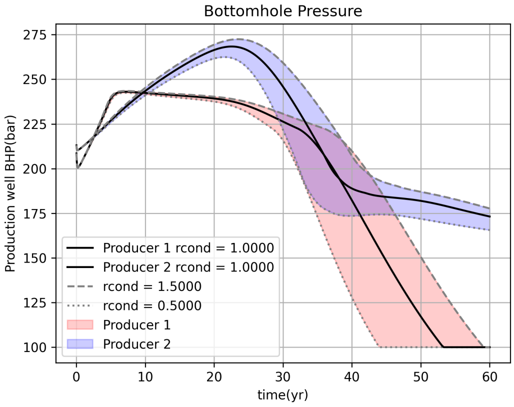

Figure C.15: BHP profile for the thermal conductivity sensitivity test

C.2 Supplemental figures to the 3D Study

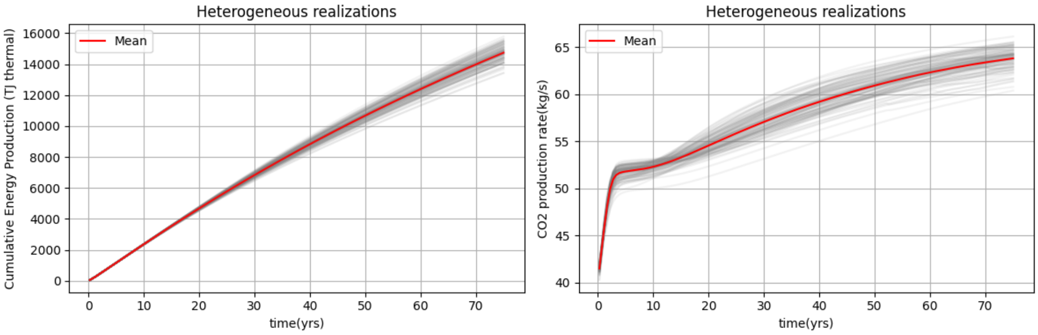

Figure C.16: Thermal energy extraction and mass flow rate for the 3D box base case realizations

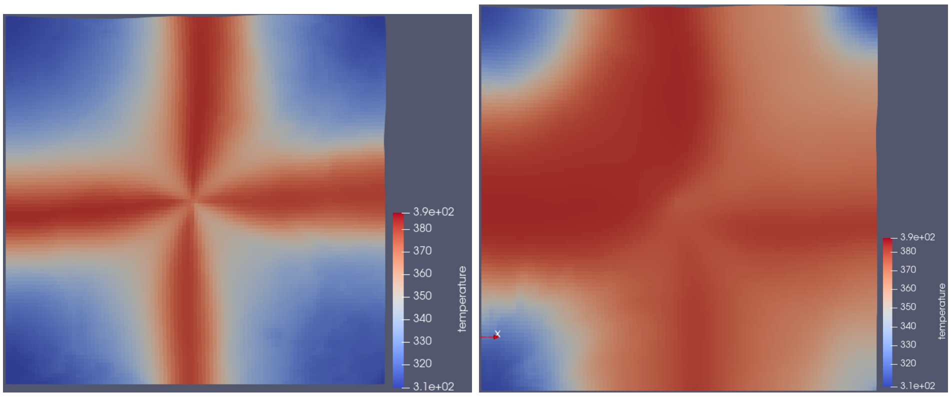

Figure C.17: Graphs showing the top down temperature distribution for the best performing realization(left) and worst performing realization(right) after 30 years of CPG